# Synthesis of zinc/zinc oxide nanoparticle-carbon nanotube composites

Martin D. Lennox

Doctoral Thesis

Department of Chemical Engineering

McGill University

Montréal, Québec

August 2013

Thesis submitted in partial fulfillment
of the requirements for the degree of
Doctor of Philosophy

## DEDICATION

*To my friends and family.*

## ACKNOWLEDGEMENTS

I have nothing less than the deepest of gratitude to my research supervisor, Professor Sylvain Coulombe, for his support, guidance, patience and encouragement over the past years. Through all the challenges I encountered, he has always been willing and able to help me find the best solution that would bring me closer to my goals. For his confidence and counsel, I am grateful.

I wish to thank everyone at McGill who helped make this project possible. It is a pleasure to thank my current and former colleagues in the Plasma Processing Laboratory for their ideas, our many discussions, their good humour and their support. I am fortunate to have excellent colleagues not only in our research group, but outside of it as well, so my thanks also go to all my current and former colleagues at McGill who provided many enlightening and enlivening discussions. I am indebted to the professors and support staff at McGill, Université de Montréal, and École Polytechnique de Montréal who contributed their assistance to this project. My thanks go to Ranjan Roy for his assistance and determination in the implementation of a number of analytical protocols; to Helen Campbell for her assistance with scanning electron microscopy and X-ray photoelectron spectroscopy (XPS); to Patricia Moraille for her help and training in atomic force microscopy; to Josianne Lefebvre for her insights and expertise in XPS analysis; to Jo-Ann Gadsby for her capabilities with all things administrative; and to Gerald Lepkyj for his electronics expertise. I wish to also thank Lou Cusmich, Melanie Gorman, Frank Caporuscio, Roberto Tariello, and all

the other members of the Department of Chemical Engineering technical and administrative staff, without whom the completion of this project would not have been possible.

I would like to acknowledge the generous financial support of the Natural Sciences and Engineering Reserach Council of Canada (NSERC), the Les Vadasz Engineering Fellowship and McGill University, and Plasma Québec.

Finally, my sincere thanks go to my friends and family. During my studies, their friendship and support has been invaluable.

Thank you.

## ABSTRACT

This thesis presents a novel process for the synthesis of zinc/zinc oxide nanoparticle-carbon nanotube composites. The process combines aerosol flow condensation for the synthesis of nanoparticles with a radio-frequency glow discharge in order to facilitate the deposition of these nanoparticles on nanostructured surfaces consisting of carbon nanotubes grown directly on stainless steel substrates. The design, construction and optimization of the process is described. A maximum observed nanoparticle deposition rate of 500 nm/min was observed when layers of nanoparticles were deposited on silicon wafers. Significant variation in the nanoparticle deposition rate was also observed; 95% confidence intervals on the prediction of nanoparticle layer thicknesses were approximately $\pm 225\,\text{nm}$ and $\pm 550\,\text{nm}$ for the evaporative source temperature range of 575 to 625 °C and measured average evaporation rate range of 0.009 to 0.048 g/min, respectively. A core/shell structure of zinc/zinc oxide nanoparticles is inferred from electron diffraction, X-ray diffraction, and X-ray photoelectron spectroscopy data.

The utility of the synthesized nanocomposites as cathode materials is evaluated in a model direct-current glow discharge system. No significant reduction in the voltages required to sustain the glow discharge were observed when the synthesized nanocomposites were tested, as compared to cathodes of nanostructured carbon nanotube surfaces or bare stainless steel cathodes.

# ABRÉGÉ

Cette thèse présente un nouveau procédé de synthèse de nanotubes de carbone décorés de nanoparticules de zinc et oxyde de zinc.

Le procédé combine la condensation d'un aérosol pour la synthèse de nanoparticules avec le traitement des particules en vol dans une décharge luminescente par radiofréquence. Cette méthode facilite le dépôt de nanoparticules sur ces surfaces nanostructurées telles que des nanotubes de carbone formés directement sur des substrats en acier inoxydable dans le cas présent. La conception, la construction et l'optimisation des processus sont décrits. Une vitesse de dépôt maximale de 500 nm/min a été observée lorsque les couches de nanoparticules ont été déposées sur des plaquettes de silicium. On a également observé une variation significative dans le taux de dépôt de nanoparticules; les intervalles de confiance à 95% pour le prédictions de l'épaisseur de la couche de nanoparticules étaient approximativement $\pm 225\,\text{nm}$ et $\pm 550\,\text{nm}$ pour la plage de température de la source d'évaporation de 575 à 625 °C tandis que le taux d'évaporation moyen mesuré variait de 0,009 à 0,048 g/min, respectivement. À partir des données de diffraction des électrons, de diffraction des rayons X ainsi que de spectroscopie photoélectronique aux rayons X, il a été possible de déduire que les nanoparticules ont une structure coeur-écorce composée de zinc et d'oxyde de zinc.

L'utilité des nanocomposites synthétisés comme matériaux pour une cathode est évaluée dans un système de décharge luminescente en courant continu. Aucune

réduction significative des tensions nécessaires au maintien de la décharge luminescente a été observée lorsque les nanocomposites synthétisés ont été testés, par rapport aux cathodes formées de surfaces nanostructurées de nanotube de carbone ou aux cathodes en acier inoxydable non-traité.

## CONTRIBUTIONS OF AUTHORS

Chapter 5 of this thesis is an article that was accepted for publication in the peer-reviewed *Journal of Nanoparticle Research*, volume 14, number 11, pages 1-8.

This article was authored by Martin Lennox (the Ph.D. candidate) and Professor Sylvain Coulombe (the research supervisor). The paper was written by Martin Lennox, who conducted the work described therein as part of the research towards the creation of this Ph.D. thesis. Professor Coulombe provided supervision of, and suggestions for, the research work performed, in addition to reviewing manuscripts prior to submission.

TABLE OF CONTENTS

LIST OF TABLES

LIST OF FIGURES

# CHAPTER 1
# Introduction

In engineering non-thermal plasma processes, comparatively little work outside of the lighting industry has been done on engineering electrode materials for sustaining the electrical discharge. Design challenges caused by the interaction of such plasmas with the electrode material can often be resolved by choosing another reactor configuration for plasma generation, such as the use of dielectric barriers to shield the electrodes from plasma exposure, or by changing the method by which the plasma is excited [1, 2]. However, recent research towards miniaturized plasma applications, such as display panels [3, 4, 5], analytical sensors [6, 7], and micro- and nano-electrical mechanical systems [8, 9] has renewed interest in developing nanostructured electrode materials that have been engineered to provide specific material properties [10, 11, 12]. More specifically, nanostructured materials are promising cathode materials, as reports of their enhanced electron emission could reduce the need for high-temperature and high-voltage emission modes in non-thermal plasmas [13, 14].

In particular, carbon nanotubes (CNTs) have been the subject of many investigations relating to their elevated electron emission under vacuum, which results from the geometrical enhancement of the local electric field as a result of the high aspect ratio of the CNTs [15, 16]. The synthesis of composite CNT materials by their chemical modification and the incorporation of nanoparticles has been of interest as a

method for engineering a broad range of materials with, for example, improved field emission properties [17, 12, 18]; high electron- and ion-induced secondary electron emission yields [19, 20]; elevated catalytic activities [21, 22]; mechanical durability [23]; and applications as electrode materials in solar cells, fuel cells, and sensors [24, 25, 21, 26]. However, most techniques rely on liquid-phase chemistry and/or the use of toxic, or expensive reagents, and this can create barriers to the scale-up of the process for commercial production. Alternatively, dry techniques tend to have higher scalability, since reactions are not limited to liquid volumes. Moreover, non-thermal plasmas can be used in these processes to chemically modify nanoparticles in-flight according to the species present in the plasma, thereby obviating the use of pure liquid reagents [27, 28, 29].

With regards to the use of nanocomposite materials as cathodes, zinc oxide (ZnO) and other metal and metal-oxide nanoparticles deposited on CNTs or other nanostructured surfaces show promise. These materials have been reported as having enhanced field electron emission [30, 12, 31], higher values of ion-induced secondary electron emission [32, 33] and the potential for photoelectron emission [34, 35, 36]. These properties have the potential to reduce the voltages required to sustain direct-current (DC) glow discharge plasmas by improving the electron emission at the cathode. Similarly, these nanocomposite materials may have further applications in reducing the power requirements of alternating current (AC) discharges, which are found in fluorescent and compact fluorescent lighting, by mitigating the need for high-temperatures at the cathode to allow for the thermionic emission of electrons that sustain these discharges [1]. In consideration of the size of the fluorescent and

compact-fluorescent lighting market, this could represent significant power savings [37, 38].

## 1.1 Objectives

This PhD thesis focuses on the synthesis and use of ZnO nanoparticle-CNT nanocomposite materials as cathodes to sustain direct-current (DC) glow discharges to investigate their utility in reducing the sustaining voltage requirements of these electrical discharges. The DC glow discharge is selected as a simple model system in which the performance and engineering challenges of these nanocomposite materials can be evaluated and better understood. Consequently, the objectives of this project are:

1. Report the design and construction and characterization of an integrated aerosol flow condensation (AFC) and radio-frequency (RF) glow discharge plasma reactor to synthesize ZnO nanoparticles and create ZnO-CNT nanocomposites.
2. Evaluate the utility of CNTs and ZnO-CNT composites as cathode materials in reducing the voltage requirements for sustaining DC glow discharges.
3. Characterize the morphology and surface chemistry resulting from exposure of the deposited nanoparticles to the RF plasma.

## 1.2 Organization of the thesis

This thesis is organized into eight chapters. Following this introductory section, a review of the literature related to this project is given in Chapter 2. Particular attention is paid to reviewing the use of CNTs and CNT-nanoparticle nanocomposites as electrode materials and gas phase synthesis methods with the intent of providing insight to the rationale for the designs and experiments used in this thesis.

Chapter 3 describes the synthesis method used for producing CNT forests solidly anchored to stainless steel (SS) substrates, details the design and construction of a DC glow discharge apparatus to evaluate the performance of the synthesized cathodes, and discusses the results of experiments using CNT-SS cathodes. In Chapter 4, the design considerations of the reactor used to synthesize ZnO-CNT nanocomposites are described briefly. Chapter 5 presents a manuscript published in the *Journal of Nanoparticle Research* and provides an overview of the reactor used to synthesize Zn/ZnO-CNT nanocomposites and their physical characteristics. Chapter 6 describes the attempted optimization of the nanoparticle deposition conditions in the reactor and evaluates the performance of the as-synthesized nanocomposites and untreated CNT-SS cathodes. Chapter 7 describes the results of an evaluation of the nanoparticle deposition rates in the reactor, and examines the effect of the RF plasma conditions on the surface chemistry and bulk composition of the synthesized nanocomposites. Lastly, a summary of the work performed is given, including the original contributions to knowledge, and recommendations for future work are made.

# CHAPTER 2
# Literature Review

## 2.1 Background

Man-made plasmas produced by electrical discharges in gases can manifest themselves in many different forms with a wide range of physical, chemical, thermal, and electrical properties. As ionized gases, they are good electrical conductors, and can have electron temperatures ranging from a few thousand Kelvin in high-pressure arc discharges to millions of Kelvin in magnetically-constricted fusion plasmas. Finer distinctions in the classification of plasmas can be made in terms of the degree of ionization, the number density of electrons, the extent of thermodynamic equilibrium between the temperature of electrons ($T_{e^-}$) and the temperature of "heavy" species (i.e. ions and neutral atoms/molecules, $T_h$), and the source of the energy sustaining the plasma. Yet for arc discharges and direct-current (DC) glow discharges, there is an intimate relationship between the interaction of the plasma with the cathode (the more negatively-biased electrode in DC discharges) and the nature of electron emission.

With regards to thermal arc discharges, where $T_{e^-} \approx T_h$, high temperatures are required at the cathode spot (the point at which the arc contacts the cathode) in order to sustain thermionic emission, where electrons are emitted from the metal cathode as a result of the thermal energy present, or to sustain thermo-field emission, where electrons are emitted as a result of the combined effects of the thermal energy present

and the applied electric field [2, 39]. These modes of electron emission are necessary, as it is this electron emission that allows the arc to sustain itself at a given externally-applied power by providing sufficient current in the discharge. Recent efforts have attempted to reduce the negative effects of temperature-sustained electron emission (i.e. cathode erosion) through the use of nanostructured coatings in an attempt to increase electron yields and/or distribute the cathode spot over the cathode surface to mitigate cathode erosion [40]. In the case of self-sustaining alternating-current (AC) non-thermal arcs, which are found in fluorescent and compact fluorescent light sources, heating of the electrodes by Joule heating and ion bombardment from the plasma is required to maintain thermionic emission from the electrodes [1]. The engineering of these cathode materials has generally been limited to metal oxide coatings to lower their work function, thus improving electron emission [41], and coiling of the cathode to improve radiative heating between the turns of the coil in order to better sustain the elevated temperatures required for high-temperature electron emission modes [1].

Within the scope of the current work, the interaction between the non-thermal plasma of a DC glow discharge, where $T_{e^-} \gg T_h$, is of interest as a model system to study the performance of nanostructured cathodes in sustaining a non-thermal discharge. Recent work has shown great promise in the use of arrays of carbon nanotubes (CNTs) as cathode materials, whose structure can drastically reduce the voltages required to sustain DC glow discharges by allowing for the field emission of electrons from the cathode surface [13, 14]. Similar improvements in the sustaining

voltages and stability of discharges in plasma display panels (PDPs) have been reported for CNT cathodes/electrodes [4, 42, 3], yet a growing body of work suggests the degradation of CNT cathodes/electrodes is an inevitable consequence of the ion bombardment of the electrode surface [43, 44] and electrical contact resistance between CNTs and their substrates [45]. In PDPs, nanocomposite electrodes made of CNTs coated with metal oxide nanoparticles have been used to provide a nanostructure resistant to ion degradation, thereby allowing for field emission of electrons, and to enhance ion-induced secondary electron emission (ISEE) from the cathode as a consequence of the material's higher coefficient of ISEE, $\gamma_i$ [46, 19]. Of course in these devices, the inter-electrode gap, $d$, may be on the order of tens or hundreds of microns. Thus the benefits of the observed enhancement attributed to field electron emission are ultimately dependent upon the applied electric field, which is a function of the magnitude of $d$ and which attains values sufficiently high to sustain field electron emission as a result of the particular structure of DC microdischarges and geometric effects at the cathode [47].

Yet the utility of nanostructured composite cathode materials composed of CNTs coated with metal oxide nanoparticles in sustaining glow discharges at values of $d$ beyond the micro-scale remains unaddressed. Specifically, it is of interest to determine whether the higher field emission capability of nanostructures supported on CNTs and different values of $\gamma_i$ for metal oxides can lower the sustaining voltages of glow discharges with larger inter-electrode gaps to values below those previously observed for untreated CNTs. If this proves to be the case, then these materials may have applications in mitigating the need for thermionic emission in fluorescent and

compact fluorescent electrodes by replacing this emission mode with field emission and ISEE.

With regards to the objectives of this PhD project, this Chapter reviews the literature relevant to the synthesis of the Zn/ZnO nanoparticle-CNT nanocomposite materials that were produced and their testing in a DC glow discharge system. The role of the cathode in sustaining glow discharges is first introduced, followed by the properties and applications of ZnO nanoparticle-CNT nanocomposites and other CNT-based materials as cathodes. A review of the methods available to synthesize such nanocomposites is then made, with particular attention paid to the aerosol flow condensation (AFC) process used in the current work.

## 2.2 The role of the cathode in DC glow discharges

The mechanism by which a DC glow discharge is generated (i.e. the electrical breakdown of the gas) is most often described by the Townsend breakdown mechanism, provided that $pd < 4000$ Torr $\cdot$ cm, where $p$ is the system pressure and $d$ is the inter-electrode distance (for larger values of $pd$, other breakdown mechanisms, such as spark breakdown, become relevant) [2]. Thorough descriptions of this mechanism are given elsewhere [2, 48]. A summary of this process from these references that highlights the role of the cathode in sustaining the DC glow discharge, and explains the potential for energy savings by increasing the efficiency of electron emission at the cathode, is presented below.

The conditions for the Townsend breakdown mechanism to occur can be described in terms of the Townsend ionization coefficient ($\alpha$), which is the electron production per unit length of $d$, and the ISEE coefficient $\gamma_i$, which is the number of

electrons produced at the cathode per ion impact. Whereas $\alpha$ is a function of the electric field, $E$, and conditions in the gas such as the ionization frequency, number density and type of neutral gas species present, and the electron mobility, the value of $\gamma_i$ depends on the cathode material and its surface properties, in addition to the gas present, and the reduced electric field $E/p$ [2].

The Townsend formula describes the current in the discharge regime known as the "dark discharge" that exists prior to the ignition of a DC glow discharge (when the electric field is uniform and independent of ionization events across $d$), and establishes the criterion for breakdown to occur [2]. In a dark discharge, two electrodes that are maintained at a given electric potential, with $pd < 4000$ Torr $\cdot$ cm, and with sufficient ohmic resistance in the electric circuit to prevent transition to an arc discharge, will experience a current that can be described by:

$$i = \frac{i_0 \exp(\alpha d)}{1 - \gamma_i [\exp(\alpha d) - 1]} \tag{2.1}$$

where $i_0$ is the current of primary electrons produced in the inter-electrode gap. Excluding any artificial sources of primary electrons, these electrons occur naturally in the inter-electrode gap as the result of random ionization of the gas by high-energy photons from the surroundings, or by cosmic rays that have penetrated the atmosphere.

The exponential terms in Equation 2.1 result from the exponential growth in the number of electrons produced by the ionization of neutral gas molecules in the inter-electrode gap by primary electrons accelerated towards the anode, and by the production of secondary electrons at the cathode as the ions produced are accelerated

towards the cathode. By definition, the dark discharge is non-self-sustaining as it depends on the production of primary electrons by external sources. Transition to a self-sustained DC glow discharge (where the electrons necessary to maintain the current density of the discharge are produced by ISEE at the cathode) occurs if the electric field is increased by increasing the applied voltage, causing the denominator of Equation 2.1 to approach zero, and which provides the following conditions for breakdown [2]:

$$\alpha d = \ln\left(\frac{1}{\gamma_i} + 1\right) \tag{2.2}$$

Once breakdown occurs, the electric field in the discharge is no longer uniform as a result of varying charge densities across $d$. The cathode layer, comprising the Aston dark space, cathode glow, and cathode dark space, is of particular interest as the ISEE in this region causes the discharge to be self-sustained. Here, the electric potential decreases from approximately the applied sustaining voltage, $V_S$, to zero at the cathode in what is known as the "cathode fall," $V_C$. Similarly, $E$ decreases from a maximum at the cathode to approximately zero at the edge of the cathode layer [2]. Based on the Engel-Steenbeck model of the cathode layer, it can be shown that $V_C$ and the corresponding reduced electric field at the cathode $E_c/p$ can be modelled as:

$$V_C = \frac{B\,(pd_c)}{C + \ln\,(pd_c)} \tag{2.3}$$

and

$$\frac{E_c}{p} = \frac{B}{C + \ln\,(pd_c)} \tag{2.4}$$

where $d_c$ in Equations 2.3 and 2.4 corresponds to the length of the cathode layer, and $C$ is defined as:

$$C = \ln A - \ln \ln \left( \frac{1}{\gamma_i + 1} \right) \tag{2.5}$$

The values of $A$ and $B$ correspond to the following semi-empirical expression for $\alpha$, and have been calculated for a variety of gases [2]:

$$\frac{\alpha}{p} = A \exp \left( -\frac{B}{E/p} \right) \tag{2.6}$$

Since $\alpha$ and $\gamma_i$ are both functions of $E/p$, and both generally increase with increasing values of $E/p$ [2], Equations 2.1 and 2.2 imply that breakdown of the DC glow discharge can be achieved at lower values of $E/p$ (corresponding to lower applied voltages across $d$) by increasing the value of $\gamma_i$ for the cathode. Furthermore, increased dark discharge currents could similarly be achieved through increases in the value of $\gamma_i$.

Examining the influence of the magnitude of $\gamma_i$ in the model of the cathode layer given by Equations 2.3, 2.4, 2.5, and 2.6 similarly indicates that, for fixed values of $pd_c$ with $A$ and $B$ constant and corresponding to a given gas, an increase in the value of $\gamma_i$ would increase the value of $C$, thereby predicting a reduced value of $V_C$ needed to sustain the DC glow discharge. Since $V_C$ is proportional to the applied voltage, $V_S$, these lower required voltages could provide reductions in the power required to sustain these types of plasmas.

The effect of cathode engineering on the breakdown voltage and dark discharge currents has been reported in a few studies using nanostructured cathodes in gas ionization sensors [7, 6]. When gold nanowires were used to induce breakdown in air,

a reduction in the breakdown voltage of 50–100 V was reported over a pressure range of approximately 0.25–1 Torr [7], with a better performance when the nanowires were used as cathodes rather than anodes. This was attributed to electrons being repelled from the nanowires in the cathode configuration, although it is conceivable the effect of ISEE could have contributed to this effect. In the same study, the dark discharge current for the gold nanowire cathode was more than doubled as compared to a parallel-plate control. The authors speculated the enhanced electric field of the cathode contributed to this enhancement, although no conclusions could be drawn in this work as to the existence of field emission.

## 2.3 Nanostructured cathodes in non-thermal plasma generation

### 2.3.1 Properties and applications of carbon nanotube cathodes

In the more than two decades following their discovery [49], a large body of work has been published regarding the synthesis and applications of CNTs. In particular, the field emission properties of CNTs has been well-documented where, as a result of the combination of their high aspect-ratio and high electrical conductivity, electrons can be emitted from CNT cathodes at room temperatures given the application of sufficient electric fields [50, 16, 15, 51]. A review of early works has reported turn-on ($E_{to}$) and threshold ($E_{th}$) electric fields (defined as the electric fields needed to produce current densities of $10\,\mu A/cm^2$ and $10\,mA/cm^2$, respectively) ranging from 0.75–4.8 $V\,\mu m^{-1}$ and 1.5–7 $V\,\mu m^{-1}$, respectively, with maximum current densities ($J_{max}$) between 0.1–10 $A/cm^2$ [51]. Almost a decade later, ranges for $E_{to}$ = 0.7–2.2 $V\,\mu m^{-1}$ and $J_{max}$ = 0.001–0.077 $A/cm^2$ were reviewed [16], with more recent works continuing to develop CNT synthesis methods and structures to give values of

the same orders of magnitude [52, 53, 54]. With the broad range of CNT synthesis techniques available, and given that electric fields corresponding to $E_{to}$ and $E_{th}$ can be realized with the judicious design of gate electrodes, Spindt-type cathodes, or other cathode configurations, CNT cathodes for field emission have been used in a wide variety of devices and applications, including X-ray sources [55, 56], cold cathodes for lighting applications [57, 58, 59], and field-emission displays [60, 61].

Yet despite the enhanced electron emission of CNTs, very few reports exist of the application of CNT cathodes to sustain gaseous discharges. As noted in Section 2.1, the use of CNT cathodes in PDP has been investigated, and other work has documented their use in generating plasmas at the micro-scale, also known as "microplasmas" [62]. The work of Zou *et al.* [63] concluded that microplasmas at 50 kPa (375 Torr) could be generated with marginal changes to the CNT film of the cathode for $d = 100\,\mu\text{m}$, however at a smaller inter-electrode gap of $d = 20\,\mu\text{m}$, the CNTs of the cathode were severely eroded. Moreover, this study reported data for the micro- and nano-second time scale, thus the ability of the CNT cathode used to sustain a microplasma is questionable. Greater success in sustaining DC microplasmas was reported in [64], where CNTs were grown outside the inter-electrode gap, which reduced the sustaining voltages required by 22% (30 V) and evidently avoided CNT degradation by ion bombardment. The authors concluded the role of the CNTs was to provide "auxiliary" electrons by field emission, thus supplementing those produced by ISEE in the discharge.

It appears that one significant barrier to the use of CNTs as cathode materials at values of $d$ beyond the micro-scale is their susceptibility to ion erosion. There has

been some interest in the use of vertically-aligned CNTs as protective materials in plasma-based space-propulsion systems [65]. Despite concluding that the resistance of these materials to ion-erosion was less than that of diamond films deposited by chemical vapour deposition (CVD), the authors speculated vertically-aligned CNTs had potential as protective coatings. Further study indicated erosion rates as high as $2.5\,\mu m\,h^{-1}$ occurred for vertically-aligned CNTs when they were irradiated by 250 eV Xe ions, which were able to expose the underlying $SiO_2$ substrate in as little as 10 min.

One successful application of CNTs as a cathode material for plasma generation was their use in a gas discharge tube (GDT) protectors, which are devices used to isolate sensitive electrical components from transient over-voltages in a circuit [66]. When an over-voltage is present, these devices ignite a plasma between two electrodes in a sealed, gas-filled tube, thus creating an intentional short-circuit which protects other components in the system from exposure to the over-voltage. When CNT electrodes were used, a reduction in the breakdown voltage of approximately 100 and 150 V was observed when a device constructed with CNT electrodes was compared to two commercially-available units, with a maximum reduction in the variability of the breakdown voltage by a factor of approximately 20. Yet this study also reported a decrease of approximately 50 V in the breakdown voltage between the two CNT electrodes over the duration of 1000 repeated tests, and noted the "depletion" of CNTs from the electrode surfaces when they were examined by scanning electron microscopy.

In fact, the exposure of CNTs to plasmas, specifically as a method for reducing the lengths of the CNTs [67], or as a means of inducing defects in the structure of CNTs, usually to improve their field emission properties [68, 69, 70, 71, 72, 73] is far better documented than the use of CNTs as cathodes for sustaining plasmas. Thus, if CNTs are to be viable as cathode materials with enhanced electron emission for sustaining glow discharges, a coating which might provide protection against CNT degradation by ion bombardment and/or enhance electron emission would be of interest. The deposition of metal, or metal oxide nanoparticles, such as zinc oxide, upon CNT surfaces may be a method for achieving this objective by creating nanocomposite materials with better electron emission and possibly better resistance to degradation by ion bombardment. In general, the deposition of nanoparticles on CNTs has been studied extensively elsewhere [74], thus the properties of and applications of ZnO nanoparticle-CNT nanocomposites are reviewed below.

### 2.3.2 Properties and applications of ZnO nanoparticle-CNT nanocomposite cathodes

By far the most promising property of ZnO nanoparticle-CNT composites is the enhanced field electron emission that has been reported in a number of studies. For example, in [75], synthesized ZnO-CNT nanocomposites required an electric field of 1.3 $\mathrm{V\,\mu m^{-1}}$ to achieve an emission current of 2 µA, relative to CNT cathodes which required an electric field of 2.5 $\mathrm{V\,\mu m^{-1}}$ to reach the same emission current. In another study, where ZnO nanorods of approximately 200 nm in length were grown from the surfaces of CNTs, values of $E_{to}$ = 3.72 and 2.68 $\mathrm{V\,\mu m^{-1}}$ were reported for the ZnO-CNT nanocomposite, relative to $E_{to}$ = 5.58 and 3.50 $\mathrm{V\,\mu m^{-1}}$ for the CNT

controls [76]. Similarly, values of $E_{to} = 3.75\ \mathrm{V\,\mu m^{-1}}$ and $E_{th} = 5.0\ \mathrm{V\,\mu m^{-1}}$ for ZnO-CNT nanocomposites, relative to $E_{to} = 4.9\ \mathrm{V\,\mu m^{-1}}$ and $E_{th} = 6.0\ \mathrm{V\,\mu m^{-1}}$ for the CNT control have also been reported [12]. Repeatedly, CNTs decorated with ZnO nanoparticles have been demonstrated to be more efficient field emitters of electrons by requiring smaller applied electric fields to achieve equivalent current densities, relative to the control case of bare CNTs.

It is worth noting that the enhanced field emission of ZnO-CNT nanocomposites appears to be dependent on the size and shape of the ZnO nanoparticles. In [77], a value of $E_{to} = 1.5\ \mathrm{V\,\mu m^{-1}}$ was reported for aligned ZnO-CNT nanocomposites with ZnO nanoparticle sizes of 5–15 nm, which was an improvement as compared to the CNT control with $E_{to} = 3\ \mathrm{V\,\mu m^{-1}}$. However, for CNTs decorated with ZnO nanoparticles approximately 100–300 nm in diameter, $E_{to}$ increased to a value of $5\ \mathrm{V\,\mu m^{-1}}$. Regarding the effect of shape of the nanoparticles on field emission, it has been reported that 3 nm diameter, spherical ZnO nanoparticles in a ZnO-CNT nanocomposite actually increased $E_{to}$ to $2.3\ \mathrm{V\,\mu m^{-1}}$ relative to $E_{to} = 1.8\ \mathrm{V\,\mu m^{-1}}$ for the CNT control [31]. However, this study also concluded that the ZnO nanoparticles increased the robustness of the nanocomposite by increasing its lifetime by a factor of approximately 2.5.

Overall, in comparing studies of the field emission of ZnO-CNT nanocomposites to those of CNTs in Section 2.3.1, it appears that, while ZnO-CNT nanocomposites have enhanced field emission properties relative to the CNT controls in these studies, the values for $E_{to}$ and $E_{th}$ reported vary widely and are dependent on the synthesis conditions of the materials tested. Despite the enhanced field emission properties

of ZnO-CNT nanocomposites, there appear to be no reports of their use as cathode materials in sustaining non-thermal plasmas.

As a material, ZnO possesses a number of properties that are potentially useful in plasma generation. With the ability of ZnO nanoparticles to enhance the field emission of CNTs as reviewed above, coatings of ZnO nanoparticles on CNTs may have the ability to enhance ISEE by lowering the energy required for incident ions to induce electron emission from the surface by potential electron emission processes such as Auger neutralization [78]. An example of this can be found in [5], where the ISEE in a PDP was increased by alloying ZnO with MgO. This was done in order to create an alloy with a band gap lower than that of pure MgO, thus increasing the efficiency of ISEE by Auger neutralization of the incident $Xe^+$ ions. The result was a reduction in breakdown voltage ranging from 30–60 V once these alloys were incorporated into the test panel.

Other work with PDPs has taken advantage of the columnar structure of ZnO nanowires to increase the effective secondary electron emission (which is an aggregate measure of the secondary electron emission by ISEE, bombardment by metastable ions, and field emission) [11]. Although the ZnO in this study was coated with a 100 nm-thick layer of MgO, the effective secondary electron emission coefficient was estimated to have increased by approximately 60%, and this was attributed to field emission of electrons by the coated ZnO nanostructures.

## 2.4 Synthesis of ZnO nanoparticle-CNT composites

A number of methods exist to synthesize nanoparticle-CNT nanocomposites. A brief review of liquid phase techniques is given, followed by "dry" techniques

performed in the gas phase. In the following, emphasis is placed on methods to synthesize ZnO-CNT nanocomposites.

### 2.4.1 Liquid phase nanocomposite synthesis methods

There are two major challenges in decorating CNTs with nanoparticles in the liquid phase. Firstly, CNTs are hydrophobic by nature, which limits reaction media to non-polar liquids or requires a pre-treatment step to make the CNTs hydrophillic for aqueous treatment [74]. The latter partially addresses the second challenge: selecting an interaction by which the nanoparticles can be attached to the CNTs (for example, covalent bonding, van der Waals forces, etc.) [74].

With regards to decorating CNTs with nanoparticles, one approach that has been described is the use of short polymer chains which bond to CNTs, thus solvating the CNTs and providing functional groups on the polymer chains that can be further reacted to attach nanoparticles [74]. In the work of Sun *et al.* [79], polyacetylene polymers with a variety thiol-containing aromatic side-chains were used to non-covalently bond to CNTs through interactions of the $\pi-$bonds of the aromatic groups with the $\pi-$bonds of the CNTs, also known as "$\pi$–stacking." ZnO nanoparticles were then attached to the CNTs by chemical adsorption between the thiol groups and ZnO nanoparticles.

Another approach to decorating CNTs is the pre-treatment of CNTs with concentrated acid solutions to induce defects in the structure of the CNTs [80, 81, 24, 82]. Although this method makes it easy to disperse CNTs in aqueous solutions for subsequent reaction with pre-synthesized ZnO nanoparticles [24] or colloids produced from the reduction of metallorganics such as zinc acetate or zinc acetylacetonate

[80, 81], the introduction of defects into the CNT structure may enhance properties such as the field emission of the CNTs by increasing the number of emission sites [83], but may also negatively affect properties such as the thermal [84] and electrical [85] conductivities.

One unique liquid-phase approach to the deposition of ZnO nanoparticles on CNTs was the use of an unfocused $CO_2$ laser to induce the growth of the nanoparticles directly onto CNTs from a liquid solution of zinc acetate dihydrate in methanol [36]. Not only did this create ZnO nanoparticle coatings with a variety of nanoparticle morphologies, but created covalent bonds between the nanoparticles and the CNTs based on X-ray photoelectron spectroscopy results (XPS).

The above is by no means a complete list of the chemistry available to synthesize ZnO-CNT nanocomposites, however this is intended to highlight the complexity and challenges of these methods. For further details on the wide variety of liquid-phase chemical synthesis techniques, the reader is directed to reviews by Eder [74] and Chu *et al.* [86], which provide excellent overviews of chemical synthesis routes available for a variety of nanoparticle materials.

### 2.4.2 Gas phase nanocomposite synthesis methods

In the following section, common gas phase synthesis techniques for nanoparticle production are reviewed. According to classical theory for aerosol formation, nanoparticle production using these techniques depends on combinations of evaporation and condensation via homogeneous and heterogeneous nucleation, coalescence, coagulation, and agglommeration for nanoparticle formation and growth [87, 88]. The principles of these processes are reviewed first and following this, descriptions

of the applications of these principles as they relate to the synthesis of ZnO-CNT nanocomposites are considered.

#### 2.4.2.1 Evaporation-condensation mechanism for nanoparticle production

To generate nanoparticles in evaporation-condensation processes, a vapour source of the material of interest is first required. The evaporation of a material $A$ from a free surface at a constant temperature and system pressure can be described by the Hertz-Knudsen equation [89]:

$$J_A = \frac{\alpha \left(p_A^* - p\right)}{\sqrt{2\pi m_A kT}} \tag{2.7}$$

where $J_A$ is the atomic or molecular flux of the material being evaporated (the evaporant) from the surface, $\alpha$ is a combined evaporation-codensation constant unique to the evaporation system and accounts for the discrepancy between experimentally measured and theoretical evaporation rates [90], $p_A^*$ is the saturated vapour pressure of the evaporant at $T$, $p$ is the the pressure above the surface of the evaporant, $m_A$ is the atomic mass of the evaporant, $k$ is Boltzmann's constant, and $T$ is the temperature of the material being evaporated, in degrees Kelvin.

As $p$ decreases, the mean free path of evaporant atoms/molecules increases. Large mean free paths are desirable in thin-film deposition processes, as operation in the free molecular regime allows for the deposition of uniform films on substrates [91]. However, as $p$ is increased to pressures where continuum mechanics become relevant, the mean free path is sufficiently short such that collisions of the evaporant atoms/molecules with each other and/or inert gases in the system result in rapid

cooling, which favours the production of nanoparticles [89]. The driving force for this is the saturation ratio, $S$, which is defined as:

$$S = \frac{p_A}{p_A^*(T)} \tag{2.8}$$

where $p_A$ is the partial pressure of $A$ and $p_A^*(T)$ is the saturated vapour pressure of $A$ at a temperature, $T$ [87]. When $S > 1$, the gas is supersaturated with $A$ and this favours the production of nanoparticles through homogenous nucleation. At any value of $S$ (although the following becomes extremely unlikely at values of $S \ll 1$), nuclei of $A$ will form as they collide with other atoms/molecules or nuclei of $A$ and conversely, nuclei will also disperse into smaller nuclei or individual atoms/molecules. However, for $S > 1$, nuclei larger than a critical radius, $r^*$, will begin to form as a result of the sum total of all collisional and dissociative processes in the system. At this size, the continued growth of nuclei into stable nanoparticles is thermodynamically favourable and so nanoparticles begin to condense from the vapour phase. Nuclei with radii less than $r^*$ are thermodynamically unstable, and these clusters tend to dissociate and disappear [87]. By minimizing the change in Gibb's free energy resulting from changes to the radius of any nucleus, it has been shown $r^*$ corresponds to:

$$r^* = \frac{2\sigma\upsilon}{kT \ln S} \tag{2.9}$$

where $\sigma$ is the surface tension of the nucleus and $\upsilon$ is the atomic volume of $A$.

Practically, the homogeneous nucleation and growth of nanoparticles will occur in a limited region above the evaporation surface that is characterized by steep temperature gradients and high saturation ratios. Moreover, the growth of nanoparticle

nuclei is not limited to the homogeneous interaction of one species. In systems with more than one species heterogeneous nucleation may occur, where these species may nucleate and grow into nano- and micro-particles.

Outside the region above the evaporation surface, vapour and nuclei of $A$ are depleted and nanoparticle growth transitions to mechanisms of coalescence and coagulation. Temperatures remain sufficiently high to allow nanoparticles to merge or partially merge, respectively, into larger nanoparticles. Lastly, the temperature of the particles lowers to a point where agglomeration occurs, where the surface energies of individual nanoparticles drive their attachment (reversible or irreversible) to each other without any coalescence or coagulation.

While it is convenient to think of the processes contributing to nanoparticle growth as occurring in discrete stages, in reality they may occur with different degrees of concurrence, depending on the configuration of the system [92, 93]. These processes have been studied extensively and form the basis of aerosol science and technology [87, 94, 95, 96]. Given this body of work, the control of nanoparticle size, size distribution, and production rate are of particular interest with regards to synthesizing nanoparticle-CNT nanocomposite materials by depositing nanoparticles on CNTs. Nanoparticle production via evaporation-condensation is almost always performed under vacuum in order to provide evaporation rates high enough for sufficient nanoparticle production and five main techniques exist: inert gas condensation, aerosol flow condensation, chemical vapour condensation, pulsed laser ablation, and arc discharge. The characteristics of each method are described briefly in the following subsections.

#### 2.4.2.2 Inert gas condensation (IGC)

IGC nanoparticle production processes are characterized by the thermal evaporation of one or more materials of interest (typically metallic elements or alloys) into a low-pressure, quiescent, inert gas atmosphere where vapour of the material evaporated condenses into nanoparticles with lognormal particle size distributions and mean particle diameters on the order of 10 nm [97]. Smaller mean diameters closer to 6 nm have been reported [98], as well as particles with much larger diameter values of 450 nm [99]. Control over the particle size distribution is possible by varying the system pressure, the gas present in the system, and the evaporation temperature and evaporation rates of the material [100]. The system pressure in IGC is usually approximately 10 Torr, although pressures ranging from 0.375 to 100 Torr [101, 102, 103] have been used.

Nanoparticles produced in IGC systems are transported by natural convection that is induced by the thermal gradients caused by the presence of the thermal evaporation source(s) present in the system. With no flowing "carrier gas" in the system that can be used to direct the transport of nanoparticles, thermophoretic collection methods, such as liquid-nitrogen cooled surfaces are frequently employed [99, 104, 97]. While the simplicity of nanoparticle production using IGC has facilitated ample research in nanocrystalline materials [105] and formed the basis for the earliest research in nanophase materials [106, 107, 108], the lack of directed nanoparticle transport has perhaps limited its application in synthesizing nanoparticle-CNT composites. Some work has been done with IGC to synthesize nanoparticle-CNT

nanocomposites for gas sensor applications [26] and to generate samples for the investigation of the physical and electronic effects of nanoparticles deposited on CNTs [109, 110]. However the use of carrier gases in AFC to better control the deposition of nanoparticles on CNTs has become more prevalent, as described below.

#### 2.4.2.3 Aerosol flow condensation (AFC)

Whereas nanoparticle production in IGC processes are facilitated by natural convection of the system gas, the nanoparticles produced in AFC processes are condensed from vapours of the material of interest by one or more gas streams introduced to the low-pressure system. These gas streams are introduced directly over or near the evaporated material in order to enhance the temperature gradient directly above the evaporant and the mass transport of vapour from the solid or liquid phase [111, 112, 113]. These two factors increase the driving force for nanoparticle production by increasing the saturation ratio. Combined with the dilution effect of the introduced gas(es), this favours the production of smaller nanoparticles. Control over the mean sizes of the nanoparticles produced has been demonstrated by adjusting the flow rates of the gases used, as well as adjustments to the system pressure, the gas present in the system, and the evaporation temperature, similar to IGC [112, 113, 97]. Practically, the introduced flow rate of gas into the system can drastically increase the pumping capacity requirements to maintain the desired system pressure, and this should be considered in the design of AFC systems.

Although nanoparticle losses to the reactor walls are inevitable in AFC systems, the ability of the carrier gas to direct the location of nanoparticle deposition has been used to synthesize nanoparticle-CNT nanocomposites. Evacuated tube furnaces with

carrier gases injected co-axially are used frequently, and have been used to deposit nanoparticles of ZnO [76, 77, 114], Ge [115], and W [116] on CNTs. Combined with the current understanding of the evaporation-condensation mechanism of nanoparticle production, AFC shows promise for the synthesis of nanocomposite materials [117, 111]

#### 2.4.2.4 Chemical vapour condensation (CVC)

CVC processes used to produce aerosols of metal nanoparticles under vacuum do so by evaporating or sublimating an organometallic precursor which, once decomposed in the gas phase, produces vapours of the metal of interest for nanoparticle formation. The precursors used typically have very high vapour pressures, relative to the metal of interest. Decomposition of the precursor is usually accomplished by pyrolysis in a resistively-heated furnace [118, 119, 120], although $CO_2$ lasers have also been used [121, 122] as well as microwave plasma for non-thermal decomposition of the organometallic precursor [123]. Once decomposed, the formation of nanoparticles proceeds according to the condensation mechanism described in subsection 2.4.2.1.

The primary advantage of CVC is that it is a versatile and well-studied technique that can be used to produce a vast range of nanoparticles and other nanoscale materials. Effectively, the nanoparticle material to be produced by CVC is limited only by the chemical and physical properties of the precursor and the reactor configuration. Additional flexibility in the reactor design for CVC processes is facilitated by the low temperatures required to evaporate the precursor (thus allowing for a wider choice in the reactor's materials of construction) and by the fact that the location in the process at which nanoparticles are condensed can be far removed from the

evaporation location if the reactor temperature profile is imposed judiciously [91]. Moreover, the technique lends itself well to producing nanoparticles of compounds, such as oxides [124], carbides [125], nitrides [126], and sulphides [119], in addition to pure-metal nanoparticles [127].

However, the precursors used in CVC are frequently toxic, carcinogenic, pyrophoric, flammable, or highly chemically-reactive. Coupled with their high vapour pressures, the handling of these substances and the associated safety considerations are often sufficiently disadvantageous to preclude the application of this technique. Additionally, the produced nanoparticles often require annealing at high temperatures to remove residual carbon, oxygen, or other atomic impurities remaining from the decomposition of the organometallic precursor [118].

With regards to the synthesis of zinc oxide nanoparticles or nanostructures, precursor molecules such as zinc acetate [128], diethyl zinc [129], zinc acetylacetonate [130] have been used. To create ZnO-CNT nanocomposites, diethyl zinc has been used [12, 31, 35].

#### 2.4.2.5 Pulsed laser ablation (PLA)

In PLA processes, lasers are used to generate nanoparticles directly from targets of the material of interest, thus replacing the need for an evaporative source. The interaction of the pulsed laser beam (typically of 5–10 ns pulse width and fluence exceeding 10 J/cm$^2$) with the target generates rapid, localized heating of the target, leading to the formation of a plasma plume and the rapid ejection of material from the surface, with nanoparticle formation proceeding in a manner similar to

the condensation mechanism described above, except that shockwaves and supersonic speeds are typical and this leads to relatively narrow particle size distributions [131]. For example, Fazio *et al.* [132] generated approximately 110 nm thin films of ZnO nanoparticles using a pulsed excimer laser at 248 nm with a pulse width of 25 ns and a repetition rate of 10 Hz to ablate a zinc target in a pure oxygen atmosphere at 10 Pa for 1 h. Other work has deposited nanoparticles of Cu, Ti, and TiN on CNTs to produce nanocomposite materials [84, 133]. Although PLA techniques make it significantly easier to generate nanoparticles from materials with high melting points and low vapour pressures, the need for expensive lasers which can only ablate small amounts of material makes this technique better suited to research applications rather than large-scale synthesis.

#### 2.4.2.6 Arc discharge

Electric arcs produce thermal plasmas that can be used to generate nanoparticles in processes similar to laser ablation, albeit only for conductive materials that can be used as cathodes. The attachment of the arc at the cathode spot causes significant heat fluxes (ranging from $10^6\,\mathrm{W\,m^{-2}}$ to $10^{10}\,\mathrm{W\,m^{-2}}$) [39], which then causes metallic vapour to form, usually through the formation of plasma plumes, shockwaves, and the supersonic ejection of material, providing a source for nanoparticle nucleation. The formation of microparticles in addition to nanoparticles in pulsed arc discharge processes can be problematic, leading to large cathode material losses [134, 135]. Copper nanoparticles formed by a rotating arc discharge have been collected on CNTs [136], although with regards to synthesizing nanoparticle-CNT composites, limited work has been done with vacuum arcs for the synthesis of metallic nanoparticles. The

literature appears to favour single-step methods where CNTs and nanoparticles are simultaneously synthesized from graphite electrodes impregnated with metal powders [137, 138] or where the cathode is immersed in a liquid medium [139, 140].

# CHAPTER 3
# Carbon nanotube cathodes for sustaining DC glow discharges

## 3.1 Introduction

The results from preliminary experiments in testing the efficacy of nanostructures of CNTs and SS316 (or SS304) as cathodes for sustaining a DC glow discharge as a model system for evaluating their utility are presented in this chapter. The details of the CNT-SS nanostructured cathode synthesis are outlined, as is the design and construction of a DC glow discharge system used to evaluate the cathode performances.

## 3.2 Experimental procedure

### 3.2.1 CNT-SS synthesis

The details for synthesizing CNTs directly from stainless steel have been described elsewhere [141, 142, 143, 144]. A summary of the particular details relevant to this work is given, below.

#### 3.2.1.1 Apparatus

The apparatus for CNT synthesis directly from stainless steel consists of a custom assembly of a quartz tube (ID=5.5 cm, length=1.22 m (Technical Glass Products, USA)), and two KF NW50 quartz flanges (EVAC AG, Switzerland). Both flanges are sealed to end caps with an elastomer seal and KF chain clamp (all from EVAC AG, Switzerland). At one end of the tube, the end cap is connected to a 6.35 mm ($1/4''$) glass tube, which is connected to the laboratory exhaust system. At the inlet,

the end cap is connected by 6.35 mm (1/4″) SS304 tubing to acetylene and argon tanks (both from MEGS Specialty Gases, Canada), whose flow rates are regulated by individual rotameters upstream of a tee where mixing of the argon and acetylene occurs. To provide heat for the CNT synthesis reaction to occur, the quartz tube is centered in a split-hinge tube furnace (HTF55000 series, Lindberg/Blue, USA).

#### 3.2.1.2 Method

The substrates for CNT synthesis were 14.3 mm (9/16″) and 3 mm diameter circles of 400×400 SS316 and SS304 wire cloth (9319T189 and 85385T117, respectively, McMaster-Carr, USA). Arch punches of the appropriate sizes were used to manually punch circles from the cloth. These were then cleaned ultrasonically for 30 min in a 150 mL Pyrex® beaker containing acetone, using an ultrasonic bath (Model 2510, Bransonic, USA). The substrates were removed from the acetone using forceps, and left to dry at room temperature for approximately 30 min. These were arranged in a single layer in a 3.5 cm×6 cm ceramic boat, which was placed inside the quartz tube, at its midpoint.

Once the ceramic boat was sealed inside the tube, the system was purged with argon at a flow rate of 600 sccm while the furnace was heated to 700 °C over 30 min. Then, 45 sccm of acetylene was added to the argon flow for 5 min, and the system held at 700 °C for an additional 30 min. The addition of acetylene to the hot furnace causes it to pyrolyze, and the presence of austenitic iron phases present on the surface of the substrate catalyzes the growth of CNTs without the need for any acid or catalyst pre-treatment of the substrate. Specifically, the temperature of the furnace allows chromium present in the stainless steel to migrate to the surface, leaving behind

islands of iron. Carbon from the pyrolyzed acetylene diffuses into this iron and, once it becomes saturated, CNTs precipitate and grow, as previously reported [141, 144]. After this time, the system was allowed to cool back to room temperature, taking approximately 2.5 h. The argon flow was then shut off, and the CNT-SS composites removed from the system.

In preparation for additional syntheses, the carbonaceous residue resulting from the pyrolysis of acetylene was removed from the interior of the quartz tube by mechanically scrubbing the walls with ethanol. To pyrolize any remaining residue, the tube was then heated under ambient atmospheric conditions using the same temperature program.

### 3.2.2 DC glow discharge cathode testing

#### 3.2.2.1 Experimental apparatus

The DC glow discharge apparatus, depicted in Figure 3–1 consists of a custom six-way cross (MDC Vacuum, USA), which is used as a chamber for the glow discharge and composed of a 6.99 cm (2 ¾″) ID tube (length=17 cm) equipped with LF NW80 flanges, with four 4.45 cm (1 ¾″) ID tubes arranged evenly around the radius and at the midpoint of the large tube. These four tubes are fit with KF NW40 flanges, which are used to connect the assembly to standard KF vacuum fittings. The cross is mounted to an optical board using custom supports to provide clearance for all components. One of the LF NW80 flanges is sealed with a stainless steel blank, while the other holds a 7056 borosilicate glass window with greater than 80% transmission between 300 and 400 nm and greater than 90% transmission between 400 and 900 nm (Part: 450012, MDC Vacuum, USA). This provides a view of the discharge in

the chamber and allows for the acquisition of optical emission spectra. DC power is provided to the interior anode located at the top of the cross through a high-voltage single-pin feedthrough (Part: 9443002, MDC Vacuum, USA) and is supplied by a 600 V DC power supply (Model: Sorensen XG 600-1.4, AMETEK, USA). A variable resistor acts as a ballast in the circuit, and is set at 2 kΩ. The flow rates of argon or nitrogen from the cylinder are regulated by mass flow controller (MFC) (Model: 5850E, Brooks Instruments, USA), before entering the system through a custom gas feedthrough with a tube size of 6.35 cm ($^1/_4''$). A custom water-cooled copper electrode with three shielded thermocouples enters the chamber through the lowest tee, and is grounded along with the chamber walls. Cooling water is supplied from the laboratory tap, and the temperature of the electrode is controlled via on-off control of a solenoid valve. The controller is implemented by the data acquisition system (DAQ) (NI 9174, NI 9211, National Instruments, USA) through a custom electrical relay system for the solenoid, all of which is controlled by a program written in LabVIEW™ 8.0 (National Instruments, USA). Similarly, the voltage sustaining the glow discharge is measured by a separate module of the DAQ (NI 9215, National Instruments, USA). The pressure of the system is measured using a Pirani gauge (Model 910 DualTrans, MKS, Denmark) and the pressure is regulated manually by adjusting a gate valve upstream of a pump-oil trap and the vacuum pump.

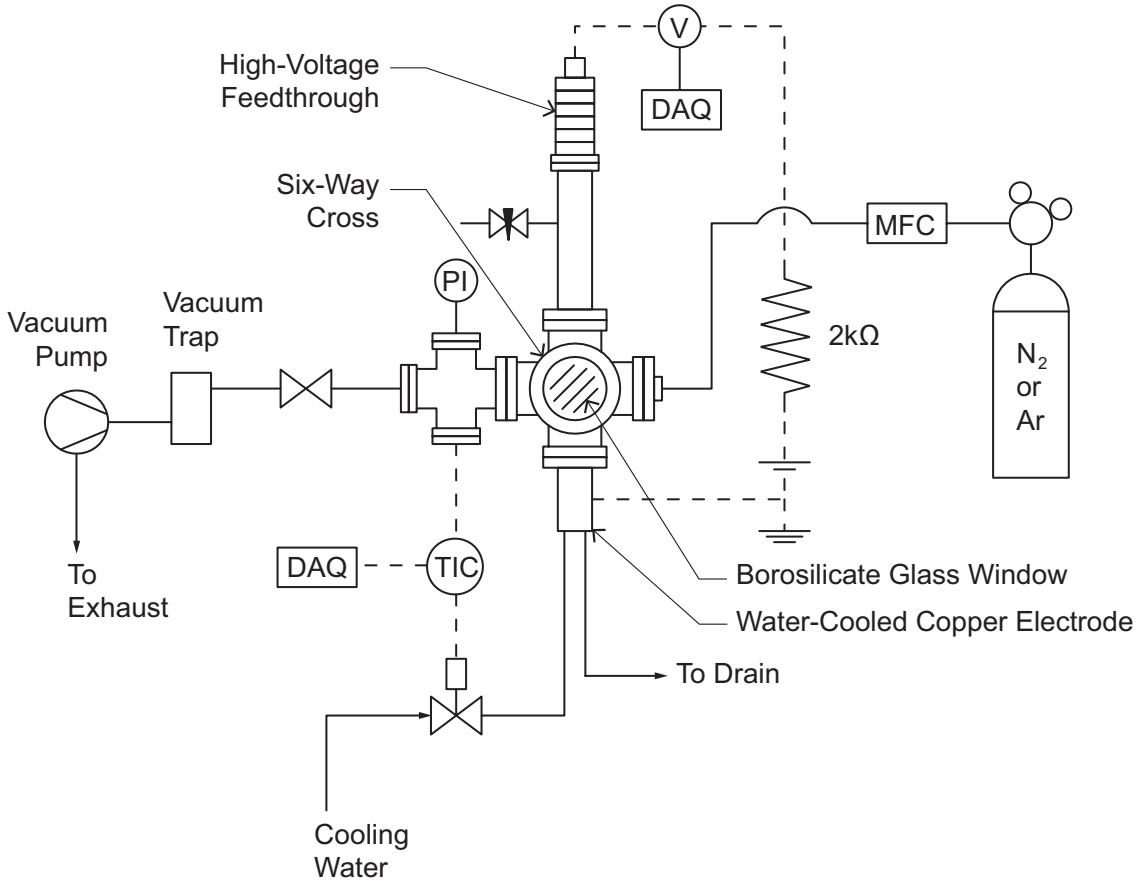


Figure 3–1: Schematic of the DC glow discharge cathode testing apparatus.

A cross-sectional diagram and dimensions of the BN cathode holder is given in Figure 3–3. Parts A, C, and D are machined from BN, with part B machined from 99.99% pure oxygen-free copper (Part: 8312K16, McMaster-Carr, USA). The cathode material to be tested is placed below the upper opening of Part A. Part C is placed in Part B in order to prevent any attachment of the plasma to the copper, and this assembly threads into part A to hold the cathode in-place. The electrical contact resistance between the cathode material and Part B is assumed to

be negligible. Lastly, Part D threads onto the assembly, and a 5 cm long, 6.35 cm ($1/4''$) diameter copper pin is friction-fit into part B to provide thermal and electrical contact with the water cooled electrode shown in Figures 3–1, 3–3, and 3–4.

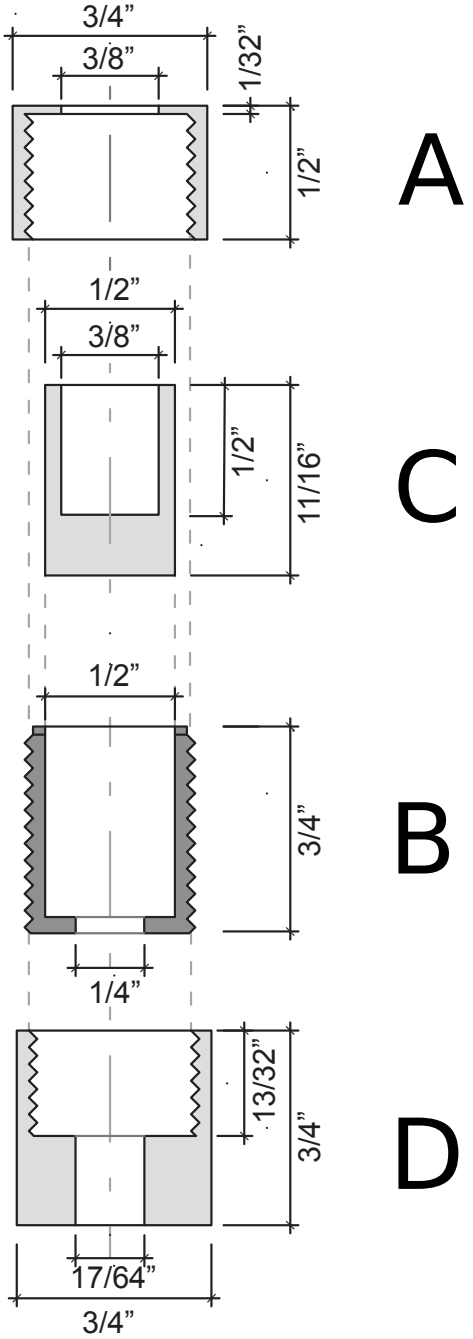


Figure 3–2: Boron nitride cathode holder, with dimensions.

Figure 3–3 shows a cross-section of the DC glow discharge chamber, and Figure 3–4 is an image of the interior of the DC glow discharge chamber with the assembled BN cathode holder. The anode in the DC glow discharge chamber is an aluminum disc with a thickness of 3 mm and radius of 1 cm whose face is hand-polished with a buffing compound (Part: 4783A3, McMaster-Carr, USA). Borosilicate glass tubing with a 1.27 cm (½″) OD (Part: 8729K37, McMaster, USA) surrounds the anode's electrical connection, and the DC discharge is surrounded by an outer borosilicate glass tube (2.54 cm OD, 2.08 cm ID, Part: 8729K51, McMaster-Carr, USA) to prevent its interaction with the walls of the system.

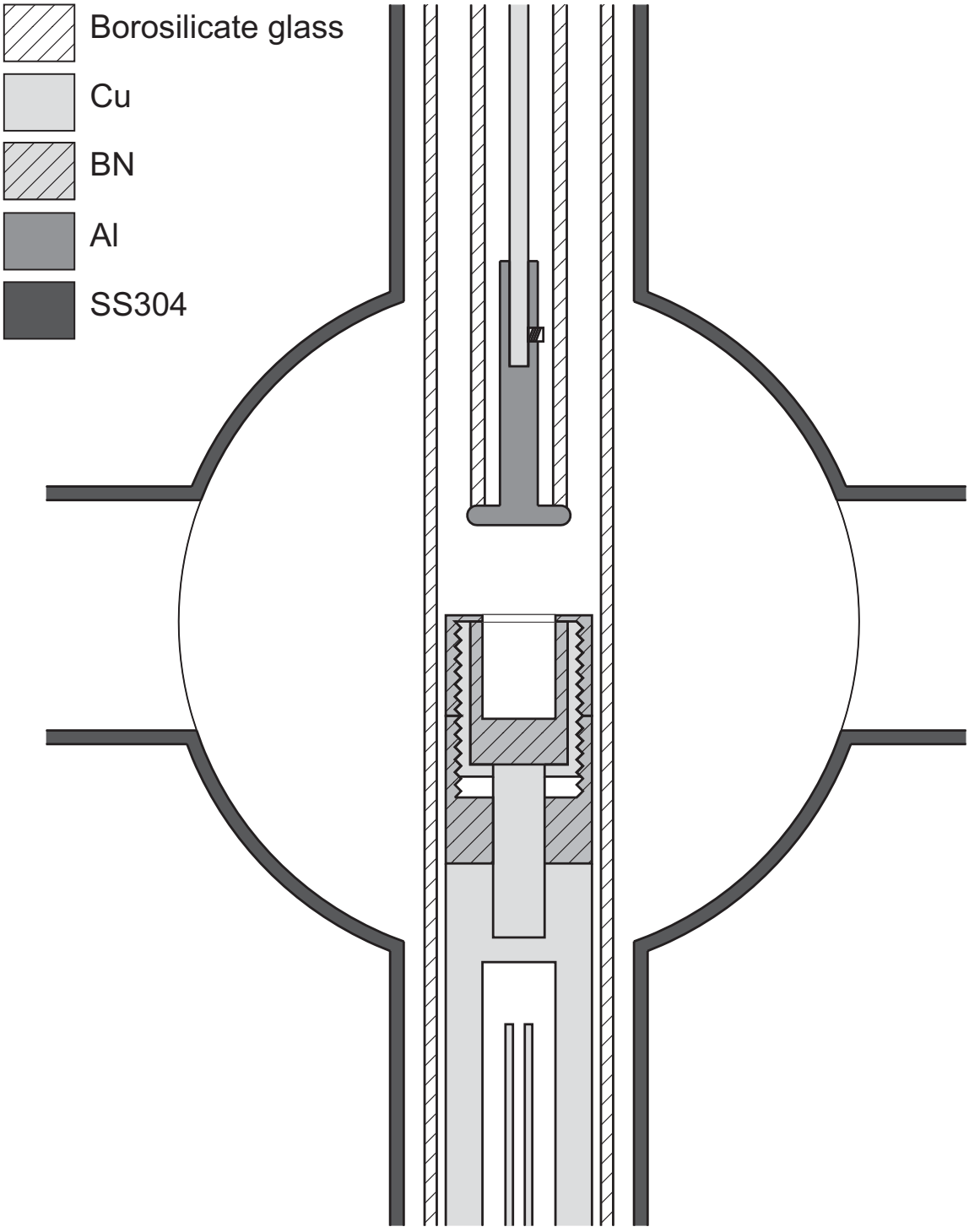


Figure 3–3: Cross-section of assembled DC glow discharge test apparatus.

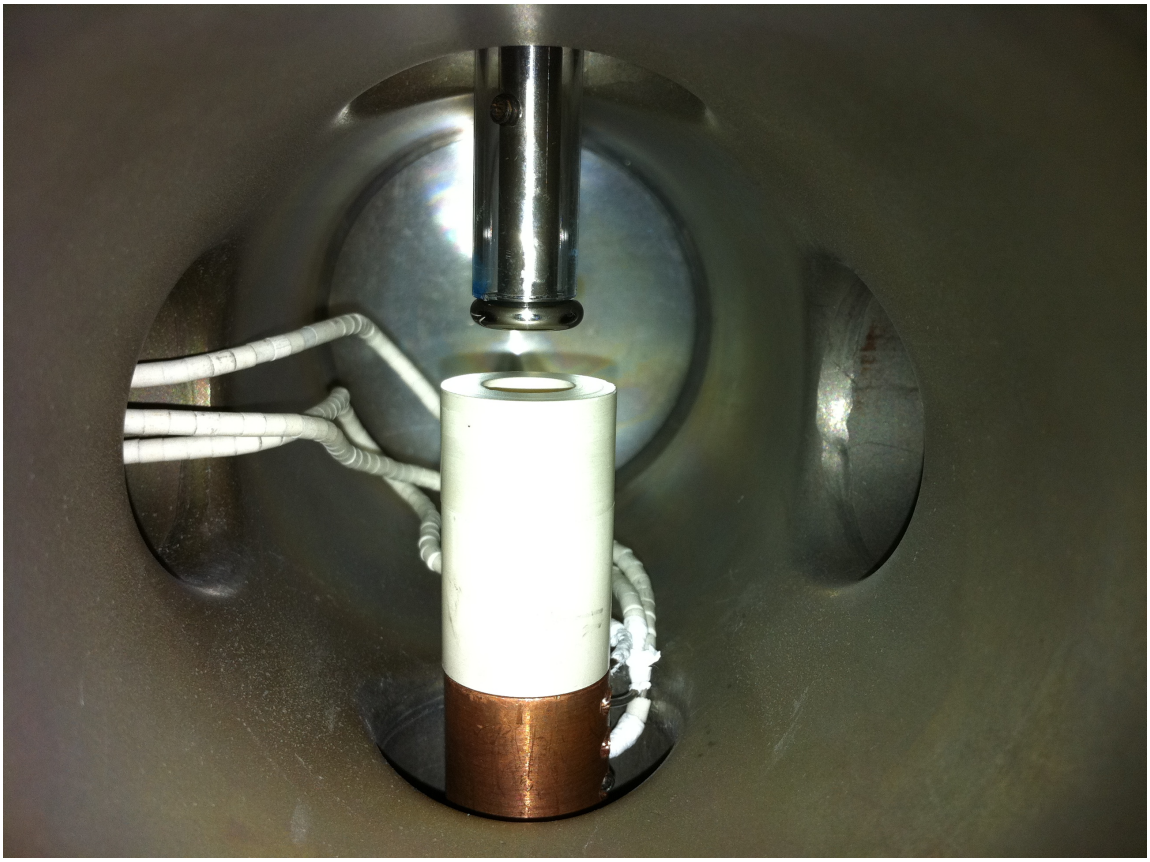

Figure 3–4: A photo of the interior of the DC glow discharge chamber, depicting the BN cathode holder, Al anode (top), the inner borosilicate glass tube, and water-cooled cathode (bottom). Note that in this photo, the outer borosilicate glass tube has been removed.

#### 3.2.2.2 Design considerations

With the objective of evaluating the performance of the synthesized cathodes in sustaining electrical discharges, a DC glow discharge system was chosen as a simple model system which could be used to measure both the breakdown and sustaining voltages required. As discussed in Section 2.2, these voltages are functions of the system's temperature, pressure, gas composition, and cathode properties, and their

regulation in the design of the apparatus was considered as follows. The temperature control of cathodes in plasma systems is commonly accomplished using water cooling, with the cathode electrically grounded to simplify safety considerations. To regulate the temperature of the plasma, the system was designed to accommodate a gas flow through the chamber with the DC glow discharge. In closed systems, the temperature regulation of a DC glow discharge (even though it is a non-equilibrium plasma) is difficult because the elastic collisions between plasma species result in temperature increases which raise the system pressure. This leads to increased voltage demands from the current-limited power supply. The net effect is a positive feedback loop which results in either a steady state at an unknown temperature and pressure particular to the system, once the heat generated by the plasma is balanced by its transfer out of the system, or in the extinguishment of the plasma once the sustaining voltage required exceeds the maximum voltage of the power supply. In addition to providing a means to control the temperature, the regulation of the gas flow rate through the system provided an effective method of controlling the chamber pressure. To ensure that only the effect of the cathode on the discharge was being measured, a test cell for the synthesized cathodes was constructed from boron nitride (BN, an insulating ceramic) and copper, and the distance between this holder and the anode was fixed. Lastly, sections of borosilicate glass tubing were used in the design to ensure the plasma was sustained only between the cathode to be tested, and the face of the anode.

#### 3.2.2.3 Testing procedure

Optimization of the DC glow discharge testing procedure revealed that chamber pressures between $P = 2.5$–$3.5$ Torr for an inter-electrode gap of $d = 7.5\,\text{mm}$ repeatedly produced glow discharges with distinct breakdowns that could be sustained within the 600 V upper voltage limit of the DC power supply. The minimum breakdown voltage required for any gas is often determined from Paschen curves, which plot the breakdown voltage of a gas as a function of the similarity parameter $Pd$. The Paschen curve is a function of the gas present and, more weakly, a function of the cathode material as a result of different values of $\gamma_i$ [48, 2]. For nitrogen, the minimum breakdown voltage generally occurs at approximately $Pd = 0.7$ Torr $\cdot$ cm, however breakdown voltages less than 600 V for values of $Pd$ ranging from 0.5 to 5 Torr $\cdot$ cm should be possible for this system [145].

The lower controllable current limit of the DC power supply was 3 mA. However, it was observed during tests at the above values of $P$ and $d$ that fluctuations in the current below this threshold to approximately 1 mA continued to produce cathode glows which still uniformly and completely covered the exposed surface of the cathode material.

Once the cathode to be tested was mounted in the system as described in Section 3.2.2.1, the sealed system was pumped-down for 15 min, and the system flushed three times with argon or nitrogen by filling the chamber to approximately atmospheric pressure and then fully opening the gate valve. The flow rate of the gas was then set at 100 sccm, and the gate valve adjusted to give the desired pressure. Data was collected for 1 min prior to activating the DC power supply.

### 3.2.3 Analytical techniques

#### 3.2.3.1 Electron microscopy

All electron microscope images shown or discussed in this chapter were obtained using a FEI Phenom Desktop SEM (FEI, The Netherlands). As a result of this system's design, the accelerating voltage and probe current are unknown.

#### 3.2.3.2 Optical emission spectroscopy (OES)

Light from the cathode and negative glow regions of the discharge is collected through the window of the DC glow discharge chamber using an optical fiber mounted on a post on the optical board at a 45° to the normal of the cathode. Spectra are recorded using a spectrometer (Model: USB2000, Ocean Optics, USA) using acquisition times of 3000 ms.

## 3.3 DC glow discharge testing of carbon nanotube composites

Based on previous reports of voltages less than 100 V sustaining DC electrical discharges when CNT-composite cathode materials were used [13], investigations as to the sustaining voltages required for unaligned CNT surfaces (synthesized as per the procedure given in Section 3.2.1.2) were undertaken. During experimentation at a pressure of 3 Torr, the cathodes tested generally resulted in glow discharges where the positive columns occupied approximately half the inter-electrode distance and the negative glow extended approximately 0.5 cm above the surface of the BN cathode holder.

Shown in Figure 3–5 is the result of one experiment where the performances of five samples ($n = 5$) of 14.3 mm diameter ($^{9}/_{16}''$) circular CNT-SS316 composite mesh cathodes from the same synthesis batch were compared to that of a similar

cathode composed only of the untreated SS316 mesh substrate as a control. Each of the five CNT-SS316 cathodes was used to sustain a total of six DC glow discharges at 3 Torr and 3 mA in nitrogen for 10 minutes. The order in which all cathodes were used to sustain this discharge was randomized in order to mitigate the effects of any confounding variables. The arrow shown in Figure 3–5 indicates the decreasing sustaining voltages observed for increasing trial numbers (i.e. progressing from the highest sustaining voltages required for the first trial through to the sixth trial). 95% confidence intervals are indicated at 1 min intervals with error bars for the first, sixth, and control trials.

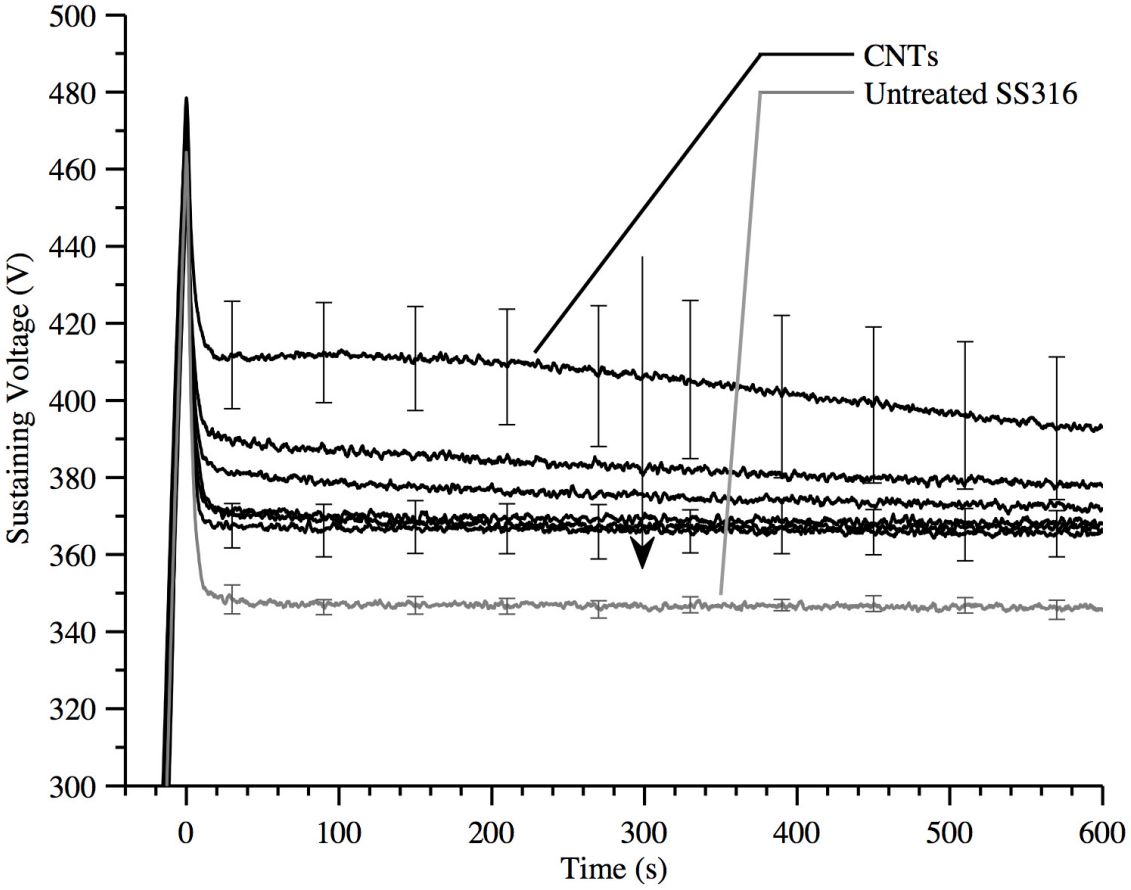


Figure 3–5: Preliminary investigation of the sustaining voltages required for unaligned CNT-SS316 cathodes. The arrow indicates the reduction observed for the required sustaining voltages in successive trials and the error bars indicate the 95% confidence intervals for Trial 1, Trial 6, and the control of untreated SS316 with $n = 5$.

As observed in the first trial of Figure 3–5, the approximately 60 V increase in the sustaining voltage (and thus the corresponding power increase) of Trial 1 (relative to the SS316 control) to 400–410 V indicated that the CNT coating as-grown from the SS316 surface made sustaining the plasma more difficult and inefficient. This increase was unexpected given the reviewed use of nanostructured CNT cathodes to reduce

voltage requirements in Section 2.3, and in consideration of the work of Dionne [13], which was able to sustain discharges at less than 100 V when using a CNT composite cathode, as compared to the sustaining voltages of 220 and 260 V needed in control experiments with bare aluminum and copper cathodes, respectively. As such, it was expected that the nanostructured surface of the CNT-SS316 composite used in this experiment would similarly reduce the sustaining voltages required to below that of the bare cathode material, and that this reduction would become smaller with time as the CNTs were degraded by the flux of ions and neutral species at the cathode of the DC glow discharge.

With regards to the former, the lack of an observed voltage reduction is attributed to the difference in the test apparatuses used, as a similar synthesis procedure with the same equipment was used in this work. In the work of Dionne [13], the cathode testing equipment relied on the transfer of a DC glow discharge from a primary, "starter" cathode to the nanostructured CNT cathode via the introduction of a high gas flow rate, and then measured the voltages required to sustain the discharge between the composite cathode and anode. Furthermore, the lack of CNT degradation observed indicates that these cathodes were not subjected to significant bombardment by ions or fast-moving neutral species. However, the use of a DC glow discharge in the current work meant that the electric field present at the cathode was that caused by the cathode fall, and that particle bombardment was present at the cathode. Considering the applied voltages used in this work were in the range of 350 to 450 V, with $d = 7.5$ mm, the resultant applied electric fields were in the range of 0.05 to 0.06 $\mathrm{V\,\mu m^{-1}}$. This is one to two orders of magnitude below the turn-on

electric fields reviewed in Section 2.3.1, and based on this, field emission in these experiments cannot be expected. Despite evidence that unaligned CNT cathodes can possess structures where the surface density of the tips of the CNTs is such that geometric enhancement of the applied electric field allows for field emission [13], no such effect was observed in the experiments performed. It was only possible to examine net effect of the composite cathode materials on the sustaining voltages required. In this regard, the disadvantage of increased sustaining voltages resulting from the presence of CNTs on the cathode is clear.

Regarding the trend seen in Figure 3–5 of the decreasing sustaining voltages required with increasing trial number, this could be attributed to erosion of the CNTs by bombardment of nitrogen ions and neutrals from the plasma. Since self-sustaining DC glow discharges rely on particle-induced secondary electron emission to replace electrons lost to ion-recombination, wall losses, and other processes dependant on the plasma species present, the magnitude of the secondary electron emission coefficient, $\gamma$ plays an important role [2]. Secondary electron emission coefficients generally increase with an increase in the reduced electric field ($E/P$) above values greater than a few hundred $\mathrm{V \cdot cm^{-1} \cdot Torr^{-1}}$ [2, 48, 146]. Very little data exists for the value of $\gamma$ for CNT surfaces; a value of $\gamma = 0.36$ has been reported [147], although this seems high as surfaces contaminated by adventitious carbon have been noted as having smaller values of $\gamma$ than their pristine counterparts [78], and that Cu and Fe cathodes have values of $\gamma$ on the order of $10^{-3}$ to $10^{-2}$ for $E/P = 10$ to $300\ \mathrm{V \cdot cm^{-1} \cdot Torr^{-1}}$. Thus assuming that the value of $\gamma$ for the CNT surface in this experiment is lower than that of the underlying SS316, and that no field-emission

is occurring from the CNTs, then it stands to reason that the gradual exposure of more of the SS316 surface by erosion of the CNTs could increase the effective value of $\gamma$, thereby reducing the sustaining voltage of the plasma.

Another, more likely explanation for the erosion of CNTs from the SS lies in the nature of the interface between the CNT and the SS substrate. It has been shown that the growth mechanism of CNTs from SS is a phase transition from austenitic iron to the CNT [141]. Consequently, the CNTs are extremely well-adhered to the SS surface [144, 13]. This results in an electrical contact resistance at the interface of the CNT and SS substrate that is sufficiently high to result into significant Joule heating of the CNT during current flow in the discharge, which ultimately leads to the destruction of the CNT [13]. It is likely this effect is responsible for the observed erosion of CNTs from the surface over time.

From Figure 3–5, it appears that there is only a slight reduction in the sustaining voltage over time in any given Trial. This is an artefact of plotting the mean of voltages measured. As seen in Figure 3–6, the individual runs comprising Trial 1 show reductions in the sustaining voltage over time.

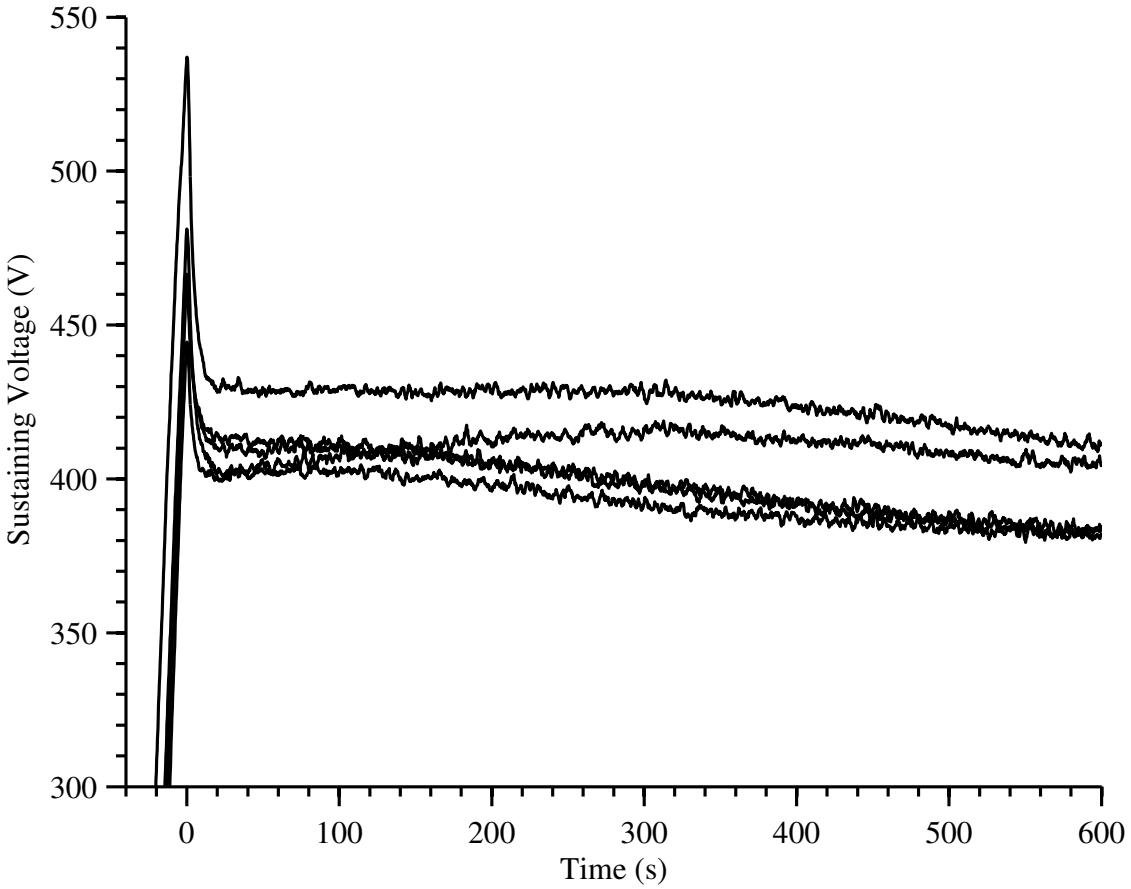


Figure 3–6: Sustaining voltages measured for the cathodes comprising Trial 1. The decreasing trend in the voltage is attributed to erosion of the CNTs at the cathode.

Confirmation of the removal of CNTs from the SS316 substrate was observed from SEM images of the cathodes before and after their use in sustaining DC glow discharges. Shown in Figure 3–7 is an example of a cathode before and after sustaining a discharge at 5 mA in argon at 3.5 Torr for 10 minutes. A residue of CNTs can be seen remaining on the substrate after its exposure to the plasma, with a greater amount of CNT residue present on the sides of the mesh's wires, where geometrical

effects may have reduced the amount of CNT erosion by ion bombardment and Joule heating. In general, all CNT residues on the SS cathodes tested were observed to be similar over the surface areas of the cathodes exposed to the plasma regardless of whether the discharge was sustained in argon or nitrogen, and subsequent use of the cathodes resulted in complete removal of these residues.

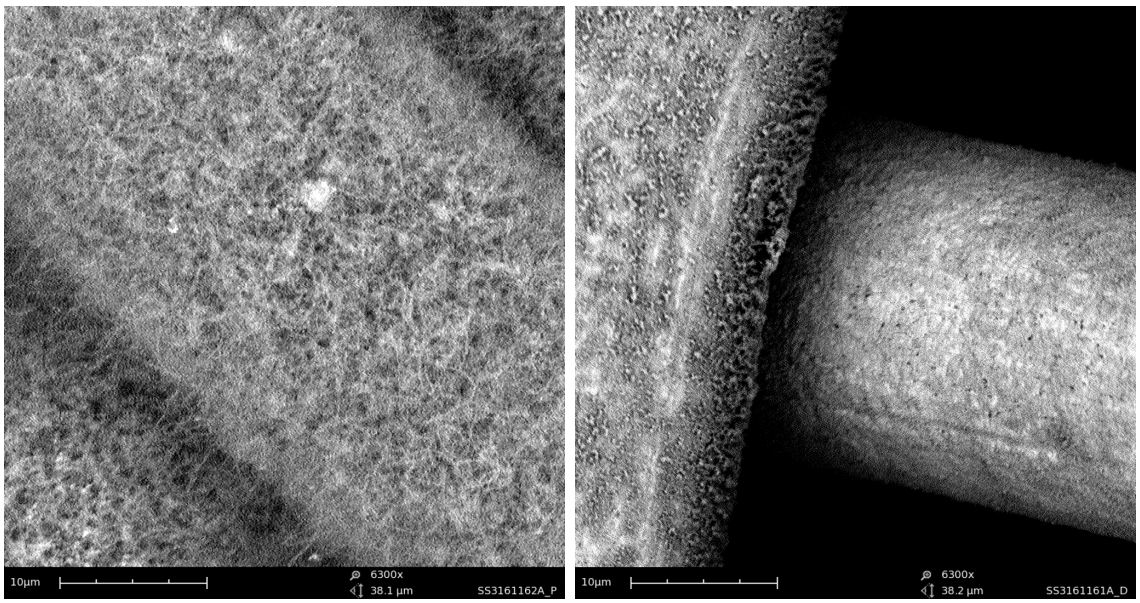


Figure 3–7: SEM image of a CNT-SS316 mesh cathode before (left) and after (right) its use in sustaining a DC glow discharge at 5 mA and 3.5 Torr for 10 min.

Figure 3–8 shows selected OES spectra of the combined regions of the glow discharge obtained at 15 s intervals of a discharge with a CNT-SS316 cathode sustained at 3 mA and 3 Torr. After initiation of the discharge, the spectra were time-invariant. Closer examination of the spectrum obtained at $t = 10$ min (Figure 3–9) shows that the ultraviolet and violet spectral lines for nitrogen dominated and assignment of the measured peaks is given in Table 3–1. The presence of peaks at approximately

300 nm indicates that carbon may have been present as a result of CNT degradation, however given the relatively small mass of CNTs deposited on the substrate relative to the amount of nitrogen present in the system and the fact that no other atomic lines corresponding to carbon are present, this assignment is highly suspect.

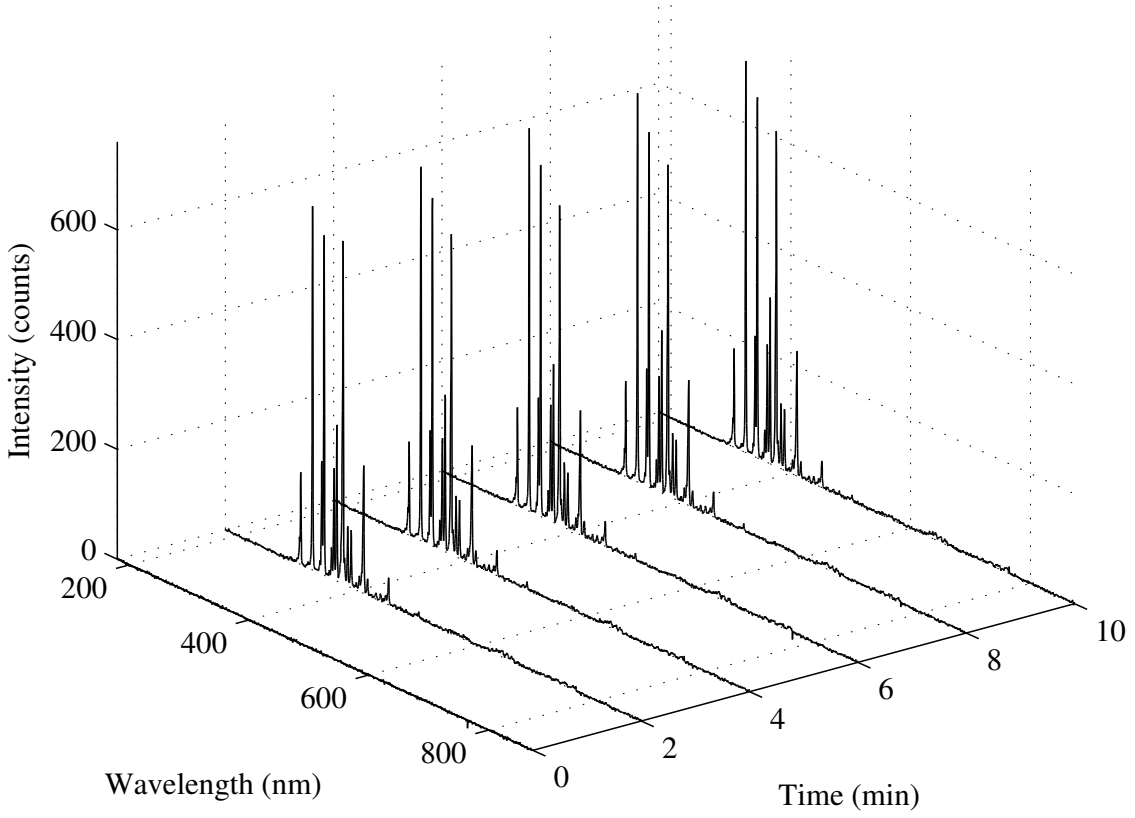


Figure 3–8: OES spectra of Trial 1 as a function of time. No evidence of carbon or zinc erosion was observed.

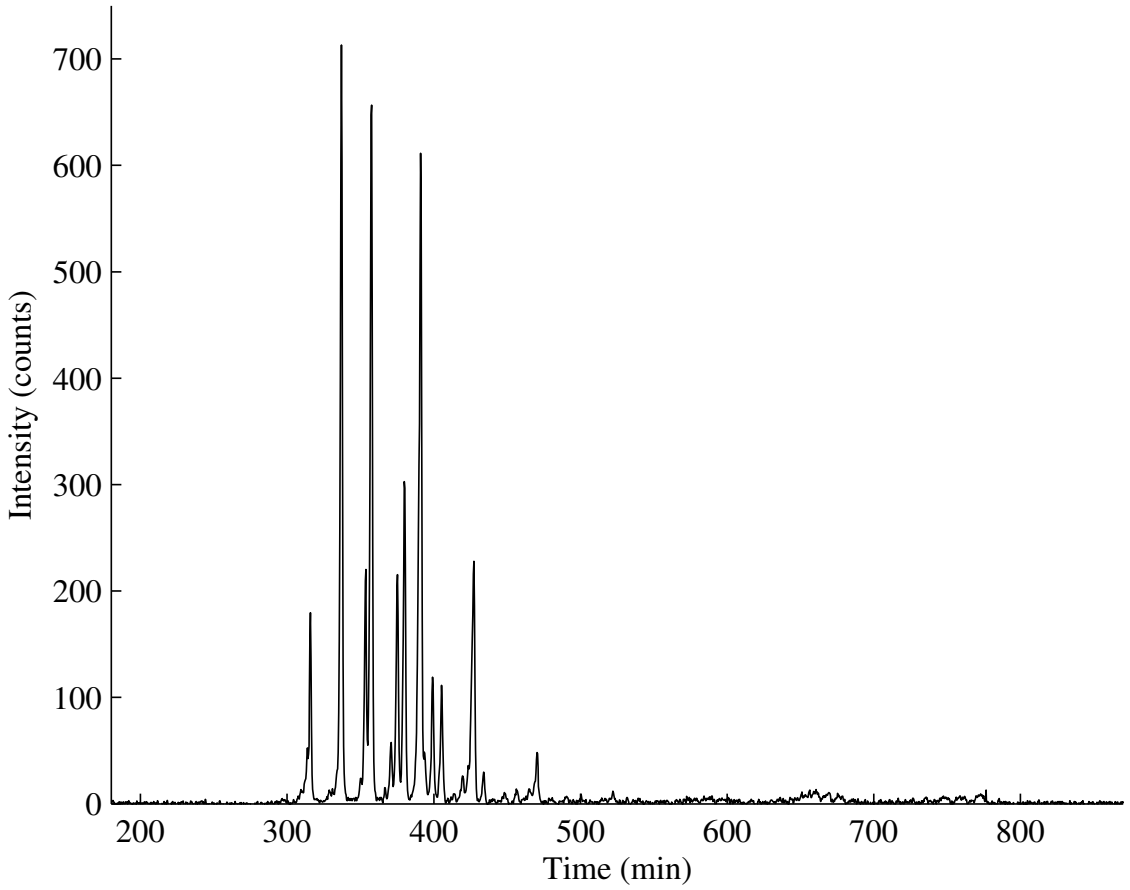


Figure 3–9: OES spectrum of the combined regions of the glow discharge at $t = 10$ min.

In light of the eventually complete removal of CNTs from the SS substrates, the fact that a significant difference existed between the sustaining voltages required for Trial 6 of Figure 3–5 and the control of untreated SS316 may be explained by the changes in the SS substrate as a result of CNT growth. It has been observed in other studies of the CNT synthesis procedure that the heat treatment of the substrates results in an increase in the surface roughness [144]. This increased roughness, specifically micro-scale features, can play an important role in reducing the voltage

Table 3–1: Peak assignments for Figures 3–8 and 3–9.

| Wavelength nm | Intensity counts | Assignment | Reference |
|---|---|---|---|
| 337 | 713 | $N_2$ | [148] |
| 354 | 220 | $N_2$ | [148] |
| 357 | 647 | $N_2$ | [148] |
| 371 | 58 | $N_2$ | [148] |
| 375 | 215 | $N_2$ | [148] |
| 380 | 303 | $N_2$ | [148] |
| 394 | 48 | $N_2$ | [148] |
| 399 | 119 | $N_2$ | [148] |
| 405 | 111 | $N_2$ | [148] |
| 391 | 611 | $N_2^+$ | [148] |
| 427 | 228 | $N_2^+$ | [148] |
| 314 | 53 | $C^{2+}$ | [149] |
| 316 | 180 | $C^{2+}$ | [149] |

requirements to initiate and sustain microplasmas [47], and this effect has also been observed at the macro-scale (electrode gaps between 3.0 and 12.1 mm) for vacuum breakdown ($10^{-7}$ mbar) [150]. Thus, in light of this, a SS mesh which had previously been used to grow CNTs and subsequently been cleaned of CNTs might have been a more appropriate control in the experiment described, and may have exhibited sustaining voltages equivalent to those of the CNT-SS meshes that had been exposed repeatedly to the DC glow discharge test system.

### 3.4 Summary

Experiments with CNT-SS composite cathodes were unable to reproduce DC glow discharges sustained with less than 100 V. The combination of the inter-electrode distance, $d = 7.5$ mm and the applied sustaining voltages of 350 to 450 V resulted in applied electric fields on the order of $10^{-2}$ V µm$^{-1}$ and this was one to

two orders of magnitude below the turn-on electric fields required for field electron emission. Erosion of the nanostructured CNT surface during testing in the DC glow discharge was attributed to Joule heating of the CNTs that resulted from the electrical resistance arising from the phase transition from the sites of CNT growth on the SS to the CNTs themselves [141, 13].

# CHAPTER 4
# Design considerations for the ZnO nanoparticle deposition reactor

After having reviewed the technologies available to synthesize such materials nanocomposites of ZnO nanoparticles and CNTs in Section 2.4.2, AFC was identified as a process which could be used to generate ZnO nanoparticles for deposition on CNTs. Previous work demonstrated the use of untreated CNTs as substrates for nanoparticle deposition [136], however the structural stability of these composites is unknown although there are indications that the high surface energies of the nanoparticles and CNTs are sufficient to maintain the adherence of nanoparticles to the substrate [74, 86]. In anticipation of addressing stability issues of the ZnO-CNT composites, a RF glow discharge was integrated into the AFC process to treat the surface of the nanoparticles in-flight, in the event that altering the surface chemistry of the nanoparticles became necessary to attempt to enhance their adhesion to CNTs. Similar in-flight treatment processes have been demonstrated previously as effective in generating both functional groups on nanoparticle surfaces, and plasma-polymer coated nanoparticles [151, 152, 28].

In this Chapter, a brief discussion of the design considerations of the ZnO nanoparticle deposition reactor is given.

## 4.1 Nanoparticle source

AFC was chosen as a nanoparticle production method for the following reasons:

1. In comparison to IGC processes, the presence of a gas flow over the metal vapour source serves to maximize nanoparticle production rates as well as direct the flow of nanoparticles through the system.
2. In order to reduce nanoparticle deposition on the walls, a "sheath gas" can be introduced around the primary, "quench gas" flow [112, 113]. This method of reducing losses is more easily implemented than those that attempt to direct the location of nanoparticle deposition by adjusting the temperature gradient driving thermophoretic deposition.
3. The nanoparticle production rate scales with the evaporative surface area of the metal vapour source.
4. The nanoparticle size can be controlled by adjusting the flow rate of quench gas [112, 113].
5. Given the motivation for including a RF glow discharge immediately downstream of the nanoparticle production location, the use of a resistively-heated nanoparticle source, rather than a plasma-based source such as cathodic arc erosion or magnetron sputtering, avoided design challenges inherent to dual-plasma processes. In such processes, the close proximity of two separately-powered electrodes can make it difficult to prevent interaction between the nanoparticle production plasma and its electrodes and the treatment plasma system [153].

To implement ZnO nanoparticle production using AFC, a molecular beam epitaxy cell (Model HTS-W-40, MBE Komponenten, Germany) was purchased and re-purposed to heat the substrate. Although effusions cells normally operate under

ultra-high vacuum conditions, operation at pressures on the order of 1–10 Torr was confirmed with the manufacturer to be within this equipment's specifications.

As reviewed in Chapter 2, and with regards to the production of ZnO nanoparticles in the designed process, both AFC and IGC have been demonstrated to be capable of producing metal and metal oxide nanoparticles. However, the production of metal oxide nanoparticles is slightly more involved, as either oxygen must be present in the reactor or the nanoparticles must be treated post-synthesis, either by exposure to ambient conditions or an active oxidation step, usually at elevated temperatures and/or imposed oxidizing atmospheres.

The production of ZnO nanoparticles by evaporation poses a particular problem, as ZnO does not appreciably evaporate, but rather thermally decomposes at temperatures above 1400 °C [154]. However, provided with excess $O_2$ in the quench gas, ZnO yields can be as high as 99%, or as low as 10% in $O_2$-limited atmospheres [155]. Yet the refractory metals which compose the effusion cell, in particular tungsten, become brittle when oxidized at high temperatures. Consequently, it was decided to produce Zn nanoparticles by evaporation and oxidize these either by the introduction of $O_2$ to the RF glow discharge downstream of the nanoparticle source, or rely on the oxidation of nanoparticles by atmospheric oxygen during storage of the synthesized nanocomposites under ambient laboratory conditions [156].

The manuscript presented in the following Chapter describes the experimental apparatus designed for the production of ZnO nanoparticles by AFC and their in-flight treatment with an RF glow discharge. An introduction to the nanocomposite materials synthesized is given in this manuscript, with the results of further

nanocomposite synthesis experiments to those presented being detailed in Chapters 6 and 7.

# CHAPTER 5
# Synthesis of Zn/ZnO nanoparticle-CNT composites

## 5.1 Preface

The following chapter presents an article published in the *Journal of Nanoparticle Research*, which was submitted in June 2012 and published in October 2012. This work was authored by the candidate, Martin Lennox, based on research done during the course of this project. Sylvain Coulombe, the research supervisor, provided project oversight and suggested changes to the manuscript.

## Dusty plasma synthesis of nanostructured Zn/ZnO-CNT composites

Martin Lennox, Sylvain Coulombe

Department of Chemical Engineering, McGill University

*Journal of Nanoparticle Research* 14(10):1245, 2012

## 5.2 Abstract

A new, dusty plasma process for depositing nanoparticles generated by aerosol flow condensation and treated using a 13.56 MHz capactively-coupled non-thermal glow discharge is described. The use of organometallic compounds as nanoparticle precursors is avoided, thereby allowing for a processing plasma free of contaminating degradation products. Nanostructured composites of zinc and zinc oxide were deposited on carbon nanotubes with complete coverage, and the influences of the argon quench and sheath gas flow rates, and the presence of 0.5%vol. ethane in

the processing plasma on the synthesized composites was investigated using electron microscopy and X-ray diffraction (XRD). In the absence of plasma, $\sim 1$ µm Zn microparticles composed of agglomerated nanoparticles were formed on the carbon nanotube surface. Plasma processing produced coatings of nanoparticles with log-normal size distributions and median diameters of $\sim 5$ nm. At maximum argon flow rates, the distribution was monomodal, whereas lower flow rates produced bimodal size distributions with the second mode having median values of $\sim 70$ nm.

## 5.3 Introduction

Metallic and semi-conducting nanoparticles are integral components of emerging technologies that make use of carbon nanotube (CNT) composite materials, such as photovoltaics, sensors and catalytic materials, yet the deposition of nanoparticles on CNTs to create such nanocomposites poses a significant manufacturing challenge. In liquids, this frequently necessitates chemical treatment of the CNTs [86, 21], which can damage their structure [82]. Moreover, the synthesis and deposition of nanoparticles is often complex and results in incomplete coverage of the CNTs, often referred to as nanoparticle "decoration" [86, 21]. Laser-induced coating of CNTs with ZnO nanoparticles in an "all-laser" process has been developed where chemical bonding of the nanoparticles to untreated CNTs has been suggested [36]. However "high" nanoparticle production rates in laser ablation processes are considered to be on the order of grams per hour [131] and generally have significant challenges in scale-up.

In the gas phase, nanoparticles have been synthesized and deposited on CNTs from evaporative processes [109] and plasma-based processes, including arcs [136, 29]

and plasma-enhanced chemical vapour deposition (PE-CVD) [157, 158]. In arc-based processes, rapid, localized heating of the cathode material at the arc attachment point causes vaporization of the cathode and ejection of the cathode material at high velocities, which subsequently condenses to form nanoparticles. On the other hand, PE-CVD of nanoparticles relies on the plasma-induced decomposition of an organometallic precursor, which produces metal vapour that then forms nanoparticles by condensation. Particularly interesting is the use of non-thermal plasmas in combination with the nanoparticle generation process, as the plasma can be used to add chemical functional groups and organic coatings to the nanoparticles *in-situ* [152]. The use of organometallics as nanoparticle precursors in PE-CVD processes can pose significant health and safety considerations, as well as placing restrictions upon the plasma composition. The decomposition products of the organometallic will be present in the plasma, consequently the chemistry of the nanoparticle coating or functionalization will be coupled to the chemistry of the chosen organometallic compound.

The following presents a dusty plasma process for depositing metal nanoparticles produced by evaporation/condensation in an aerosol flow condenser [113] on CNTs to synthesize a nanostructured composite material without the use of organometallic precursors. The nanoparticles are exposed in-flight to a non-thermal RF glow discharge and are deposited with complete coverage of the exposed CNT surfaces. This offers a new approach to aerosol-based nanoscale synthesis, which traditionally uses organometallics in PE-CVD, or thermal plasmas, flames, laser ablation, or other

thermal methods for nanoparticle synthesis [111], and allows for the functionalization of nanoparticles in-flight by a plasma whose chemistry is decoupled from the nanoparticle synthesis method.

## 5.4 Experimental

### 5.4.1 Nanoparticle synthesis

The experimental apparatus is shown in Figure 5–1 and consists of six connected systems: the gas handling system, the evaporative source, the cooling system, the plasma generation system, the substrate mounting system, and the vacuum system. In the gas handling system, Zn nanoparticles are condensed from the evaporative source using argon introduced by a water-cooled nozzle. This consists of a 20.64 mm $\times$ 1.59 mm ($^{13}/_{16}'' \times {}^{1}/_{16}''$) rectangular orifice centred in a "shower-head" arrangement of sixteen 1.59 mm ($^{1}/_{16}''$) diameter holes spaced evenly around the circumference of the reactor's interior wall. The flow rates of quench gas ($Q_N$) to the rectangular orifice and sheath gas ($Q_S$) to the shower-head are regulated by two rotameters. During heating and cooling of the system to the operating temperature (T), the quench and sheath gas is shut off and argon is introduced to the base of the reactor by a rotameter at a flow rate of 5-10 sccm to maintain the evaporative source in an inert atmosphere. The flow rates of argon and mixtures of argon and ethane used in plasma processing ($Q_{PP}$) are controlled by mass flow controllers (MFC) (Brooks 5850E) and are introduced downstream of the evaporative source. The pressure of the reactor ($P_R$) is regulated by choking the total flow ($Q_T$) to the vacuum pump.

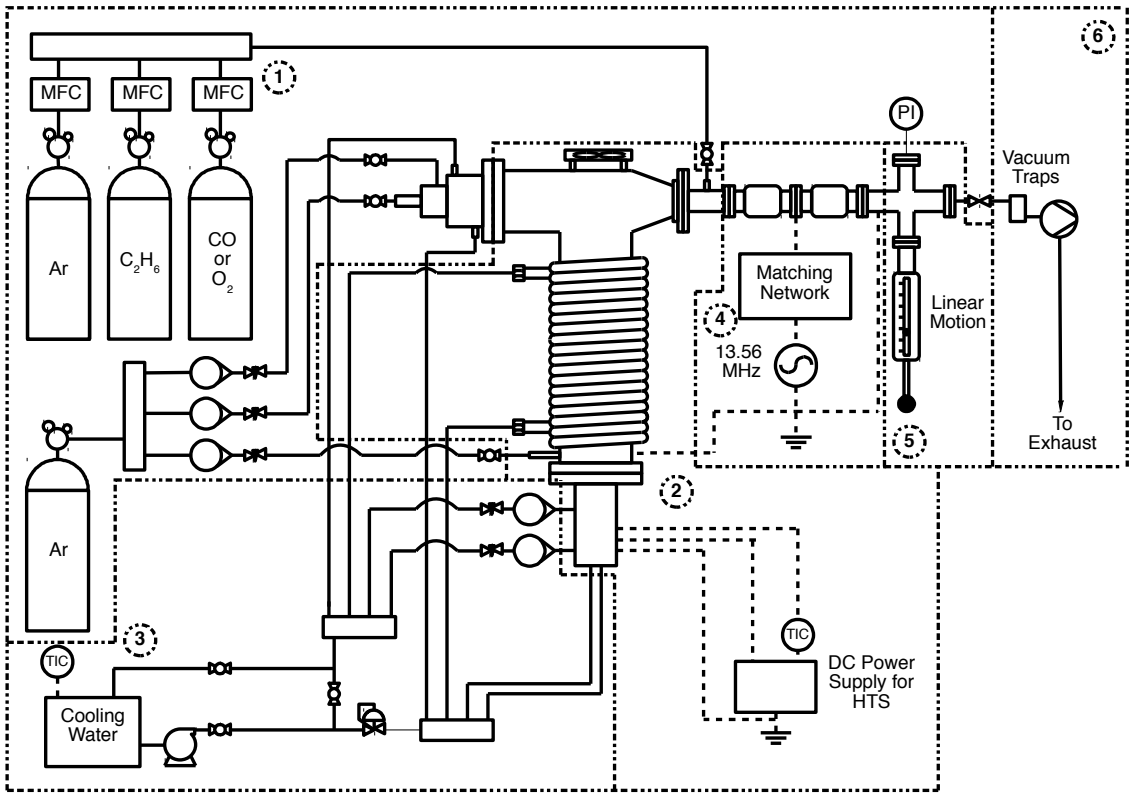


Figure 5–1: Schematic of the nanoparticle production and deposition apparatus. The six connected systems are 1) the gas handling system, 2) the evaporative source, 3) the cooling system, 4) the plasma generation system, 5) the substrate mounting system, and 6) the vacuum system.

The evaporative source (MBE Komponenten HTS-W-40) is mounted directly below the rectangular orifice of the nozzle, with the centre of its 16 mm ID $Al_2O_3$ crucible located 20 mm downstream. The source was initially loaded with approximately 20 g of 99.99% pure, 6.35 mm ($1/4''$) diameter $\times$ 6.35 mm ($1/4''$) cylindrical Zn pellets (Kurt J. Lesker), which subsequently melted during experimentation. Additional pellets were added between experimental trials to maintain the mass of Zn in the crucible between 15 g and 25 g. Cooling is supplied to the reactor wall via

eighteen turns of 6.35 mm (1/4″) copper tubing. Cooling water is circulated in a closed-loop between the nozzle, evaporative source, and copper tubing, and was maintained during experiments at 16 °C using a recirculating water bath (PolyScience 9601).

A capacitively-coupled, RF glow discharge operating at 13.56 MHz and 20 W was generated between two NW25 insulating glass breaks (MDC Vacuum). RF power is supplied by a Dressler CESAR model 1312 generator and model VM 1000 A matching network. Substrates were mounted on a 12.7 mm (1/2″) square copper target at the end of a linear motion (MDC Vacuum) and were exposed to the nanoparticle stream for the desired deposition times ($t_d$). A summary of the experimental conditions used is presented in Table 5–1.

For the CNT substrates, CNTs were grown directly from 14.29 mm (9/16″) diameter circles of 400×400 stainless steel 316 (SS316) mesh, using the method described previously [142].

Table 5–1: Experimental conditions used in the synthesis of Zn/ZnO-CNT nanocomposites. All flow rates listed are for argon, with the exception of $Q_{PP}$ in Trial 5, whose composition is listed in the "Plasma Composition" column.

| | $t_d$ | T | $Q_N$ | $Q_S$ | $Q_{PP}$ | $Q_T$ | $P_R$ | Plasma Composition |
|---|---|---|---|---|---|---|---|---|
| | min | °C | SLPM | SLPM | SLPM | SLPM | Torr | %vol. |
| 1 | 15 | 500 | 4.43 | 2.99 | 1.000 | 8.42 | 10.0 | N/A |
| 2 | 15 | 450 | 2.00 | 2.00 | 0 | 4.00 | 10.0 | N/A |
| 3 | 5 | 500 | 4.43 | 2.99 | 1.000 | 8.42 | 5.2 | 100% Ar |
| 4 | 5 | 500 | 0.84 | 0.90 | 0.324 | 2.06 | 5.2 | 100% Ar |
| 5 | 5 | 500 | 0.84 | 0.90 | 0.324 | 2.06 | 5.2 | 99.5% Ar<br>0.5% $C_2H_6$ |

### 5.4.2 Electron microscopy

Images of the nanocomposites were obtained using a Hitachi SU-8000 FE-STEM and Hitachi SU-4700 FE-SEM. Bright field TEM images and the corresponding selected area diffraction patterns (SAEDs) were obtained at an accelerating voltage of 200 kV using a Philips CM200 equipped with an AMT XR80C CCD and a camera constant of 65 mm·Å. SAED patterns were integrated radially to index the Debye-Scherrer rings in ImageJ (v. 1.45s). Nanoparticle size distributions of the nanocomposites were estimated by measuring particle lengths from STEM images using ImageJ [159].

## 5.5 Results and discussion

### 5.5.1 Nanoparticle deposition

The results from Trials 1 and 2 show that in the absence of plasma, hexagonal Zn microparticles were deposited on the CNTs of the substrate with separation between the particles on the order of 1 µm (image not shown). The shape of these particles was similar to those reported in earlier studies of inert gas condensation [97]. However, high-resolution FE-SEM imaging revealed that the microparticles appeared to be composed of individual nanoparticles that had agglomerated, as shown in Figure 5–2. In some instances, it appeared that these microparticles had formed around the CNTs of the substrate. This suggests the microparticle formation proceeds in two steps: firstly, nanoparticles nucleate from metal vapour produced by the evaporative source, then agglomerate in a preferential orientation.

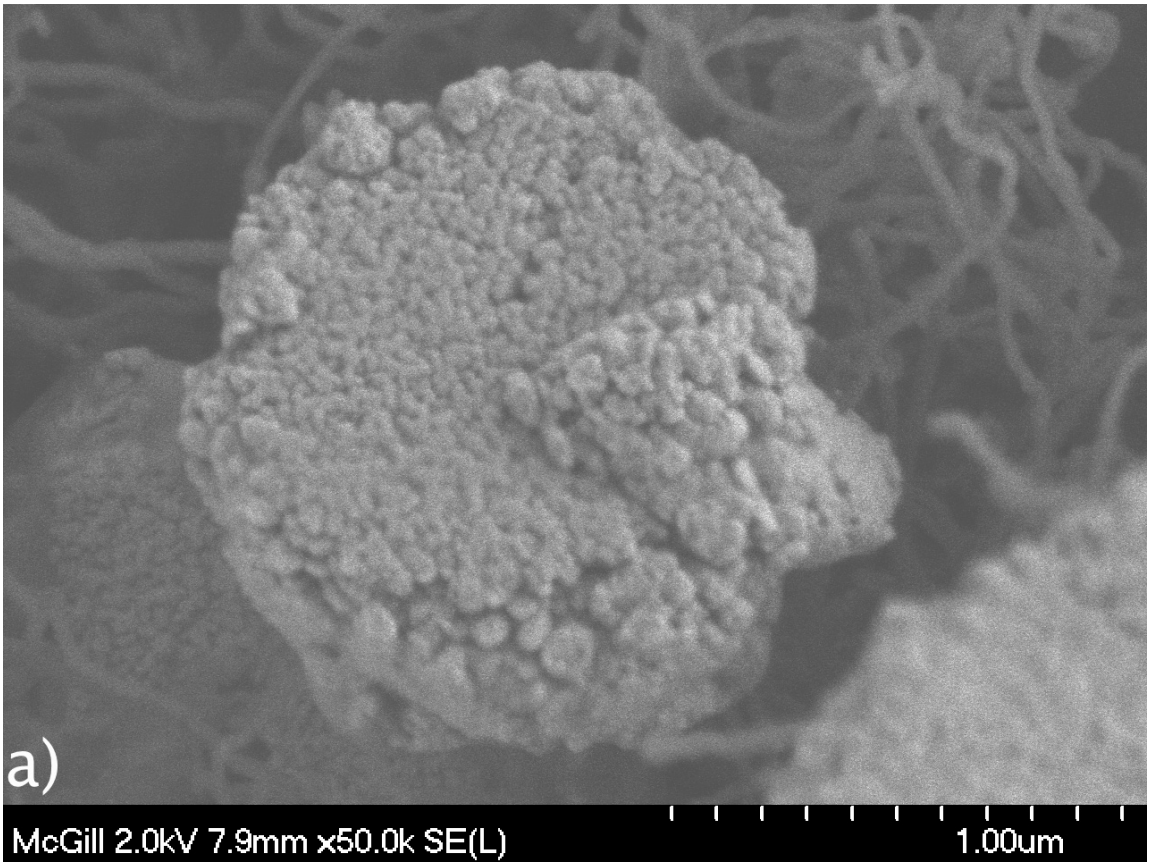
a)
McGill 2.0kV 7.9mm x50.0k SE(L)
1.00um

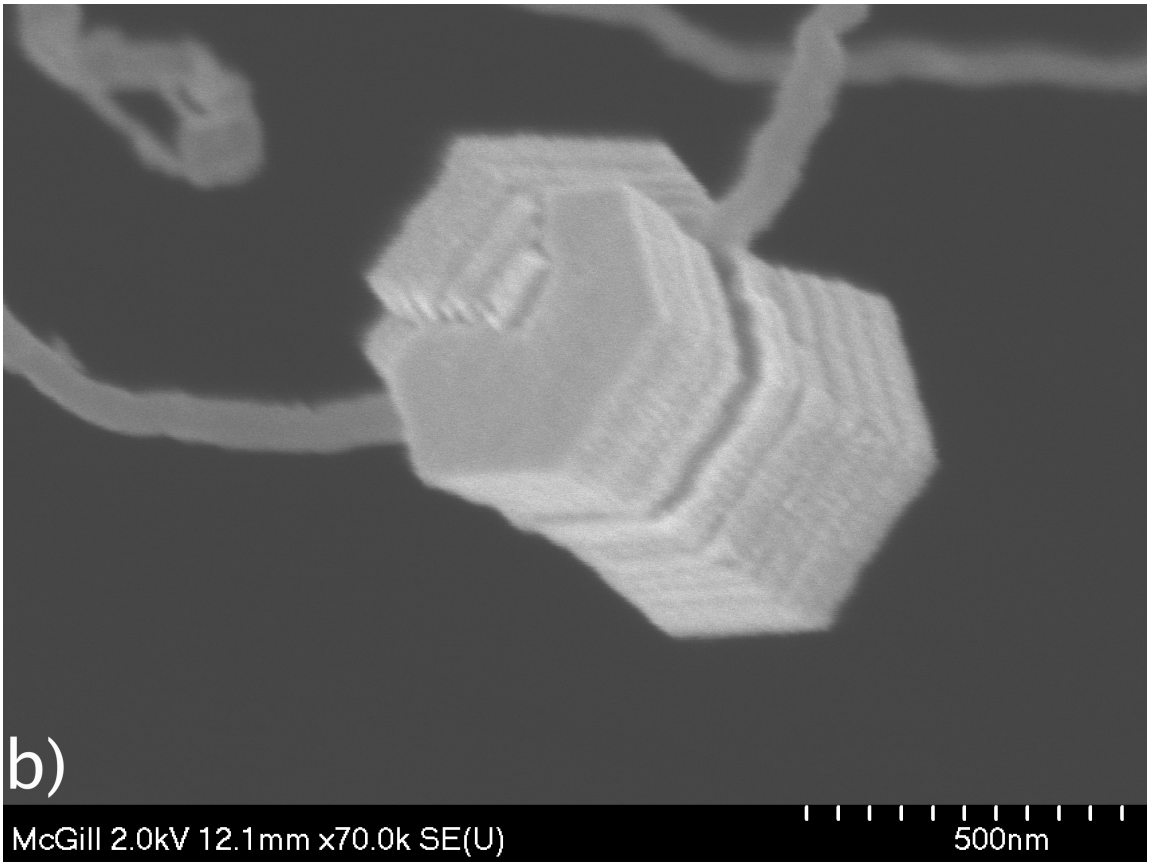


Figure 5–2: a) SEM image of a Zn microparticle composed of agglomerated nanoparticles deposited on CNTs (Trial 1) and b) SEM image of a Zn microparticle appearing to have formed around a CNT from (Trial 2).

In the presence of an argon plasma and at maximum flow rates of argon through the system (Trial 3), Zn nanoparticles were rapidly deposited on the CNT surfaces, as seen in Figures 5–3a) and 5–6. It is likely that the charge acquired by the nanoparticles while passing through the plasma prevents their agglomeration in-flight into microparticles. Upon deposition on the grounded CNT substrate, this charge would be lost, leaving the nanoparticles free to deposit as a coating of the exposed CNTs.

Reduction of the argon flow rates (Trial 4) favoured the production of a bimodal distribution of nanoparticles deposited on the CNTs (Figures 5–3b) and 5–7), with the smaller particles arranged in filamentous structures between larger particles. However, the addition of 0.5%vol $C_2H_6$ (Trial 5) prevented the formation of this mixed-mode filamentous structure, as seen in Figure 5–3c). Nanoparticles processed in similar plasmas [28] were coated with a plasma polymer coating, thus it is conceivable that a change in the surface chemistry of the nanoparticles could explain the observed formation of large agglomerates of nanoparticles, and so work is currently in progress to quantify the functional groups present in films of these nanoparticles. Particularly interesting is the structure of the coating on the CNTs between the agglomerates; the addition of $C_2H_6$ appears to have favoured the formation of a uniform nanoparticle coating similar to that of Trial 3, but at much lower argon flow rates. With regards to the uniformity of the nanoparticle deposition in Trials 3, 4, and 5, no lateral position-dependant variation of the nanoparticle deposits was observed under the electron microscope. However in areas of dense CNT coverage on the substrate, nanoparticles were prevented from depositing on CNTs lying underneath other CNTs as a shadow effect of the deposition process. An example of this, observed in Trial 4, is given in Figure 5–4.

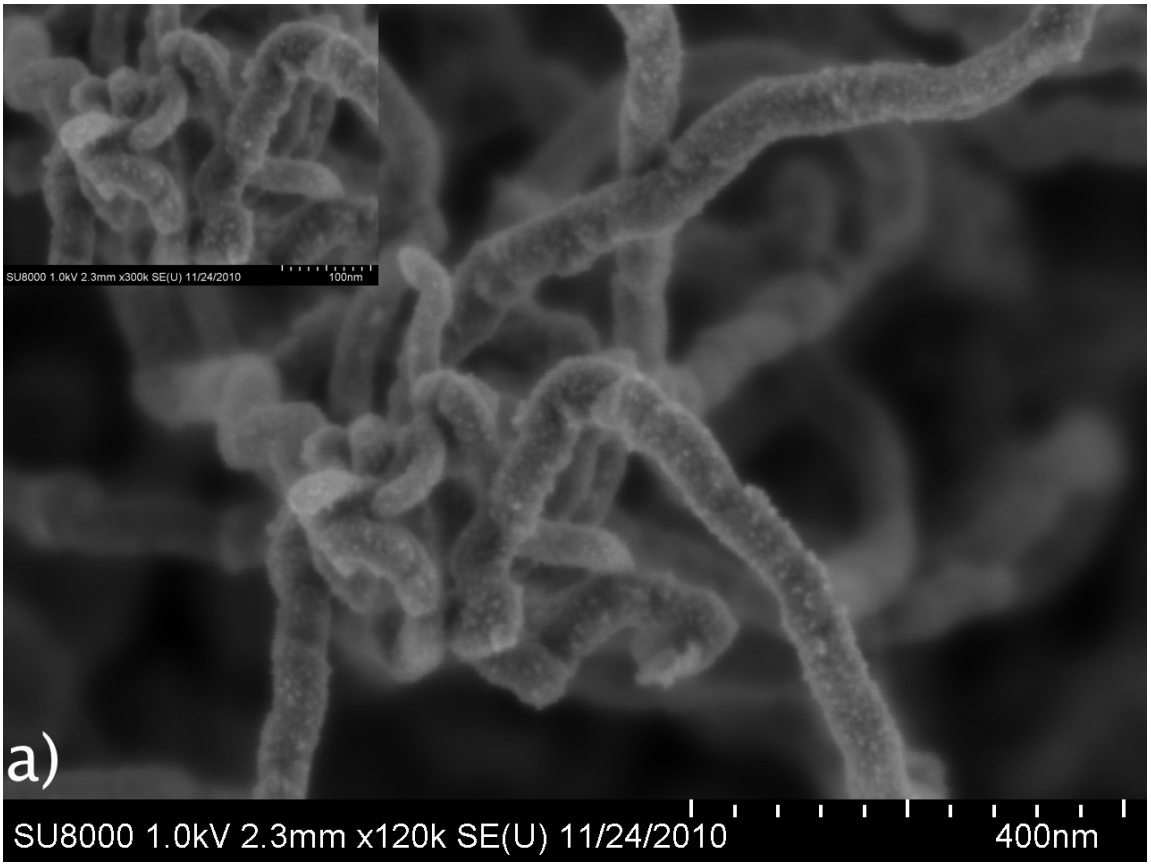
SU8000 1.0kV 2.3mm x300k SE(U) 11/24/2010
100nm
a)
SU8000 1.0kV 2.3mm x120k SE(U) 11/24/2010
400nm

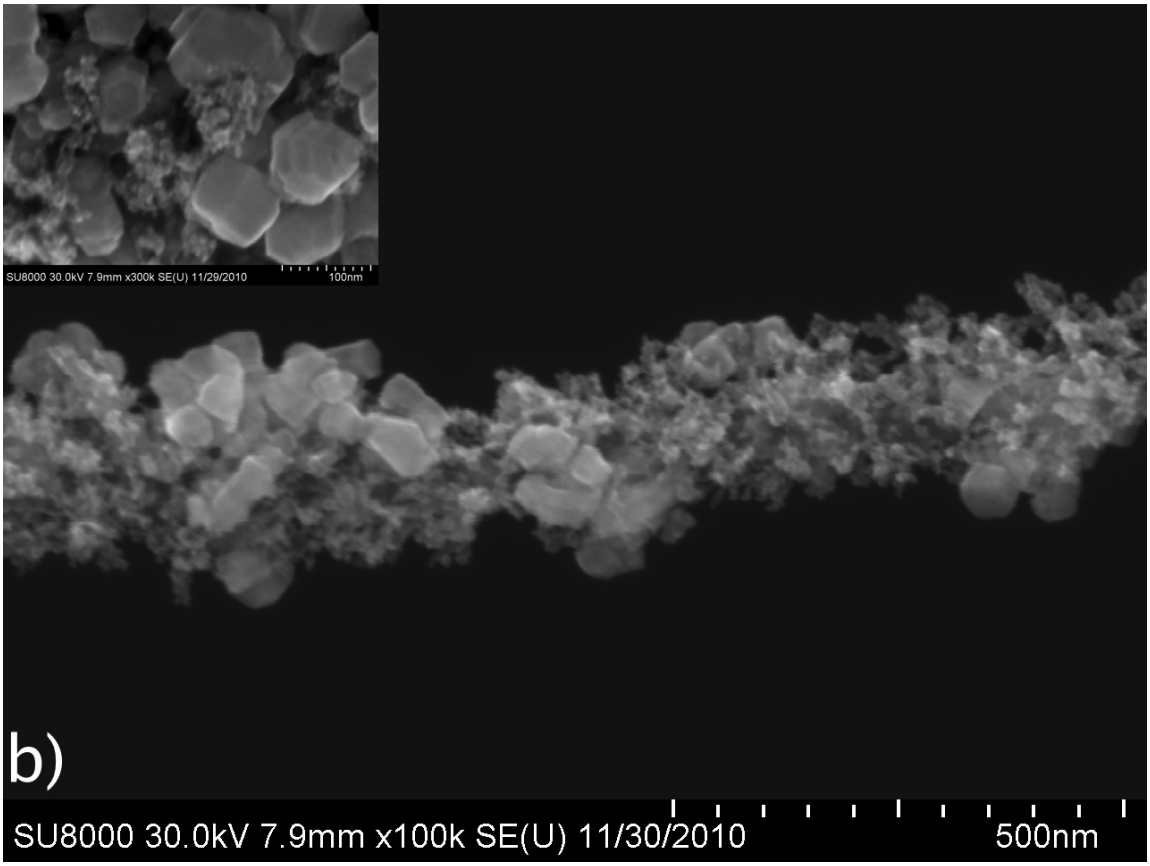
SU8000 30.0kV 7.9mm x300k SE(U) 11/29/2010
100nm
b)
SU8000 30.0kV 7.9mm x100k SE(U) 11/30/2010
500nm

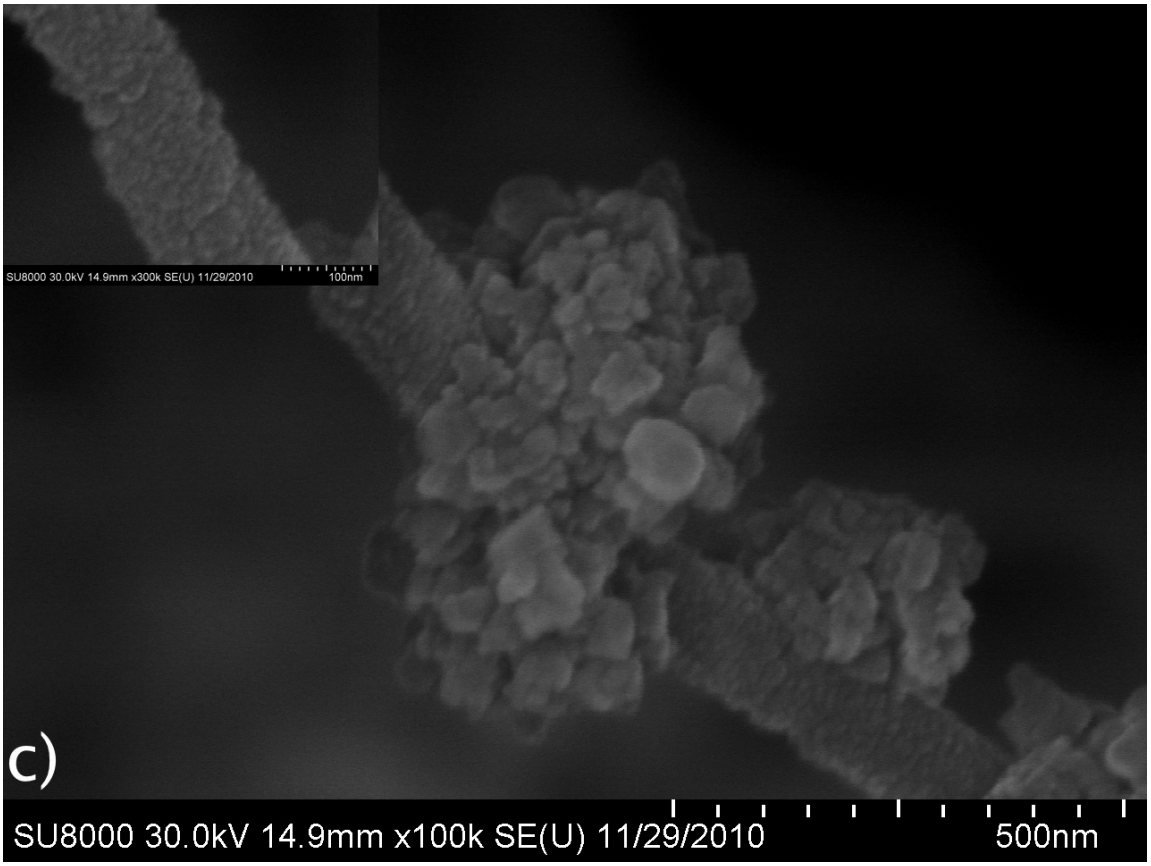


Figure 5–3: STEM images of nanoparticle-coated CNTs from a) Trial 3, b) Trial 4, and c) Trial 5.

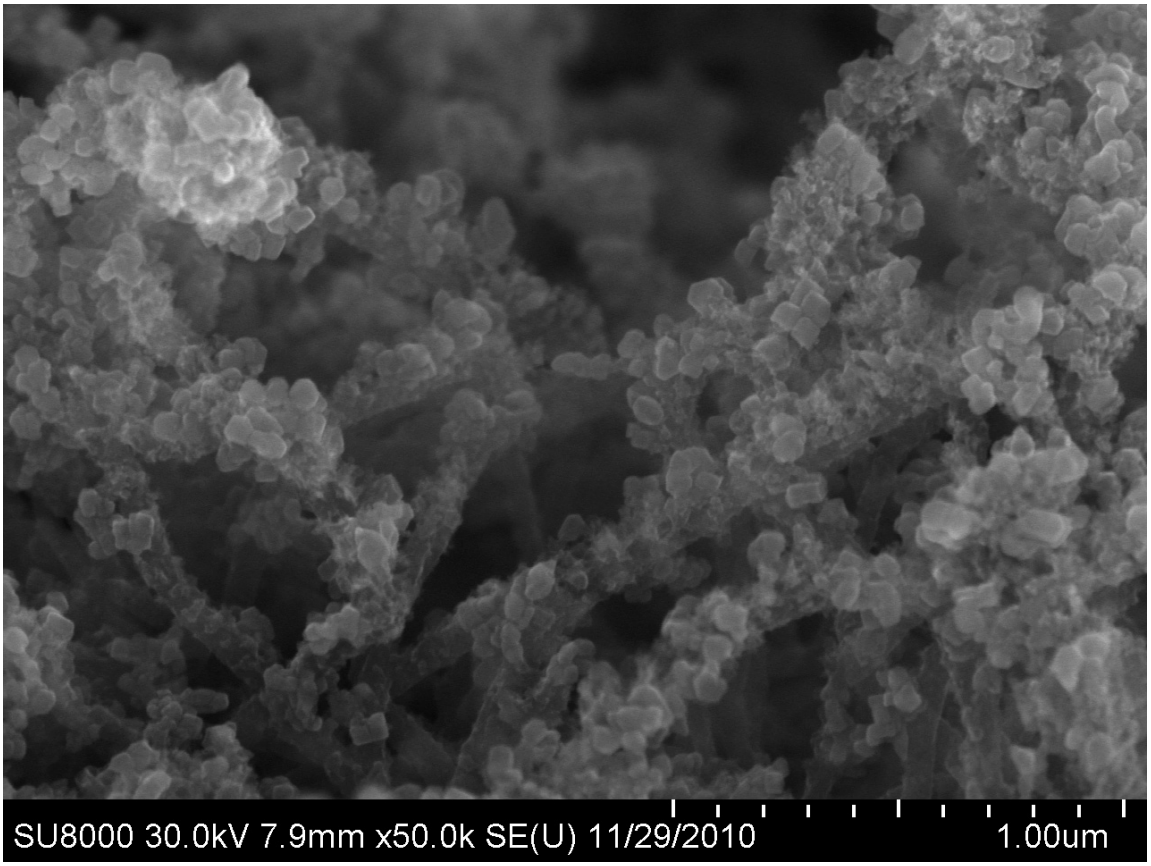


Figure 5–4: An example of reduced nanoparticle deposition in the vertical direction in Trial 4 as the result of the shadowing effect of overlying CNTs.

The measured nanoparticle size distributions for Trials 3, 4, and 5 are given in Figure 5–5. Log-normality of the distributions was confirmed from lognormal probability plots (not shown) and a summary of the values from the fit continuous lognormal probability distribution functions is given in Table 5–2. The modes of the measured distributions in Figure 5–5b) and 5–5c) are presented on separate axes since it was impossible to accurately measure smaller nanoparticle sizes at the magnifications required to obtain a representative sample of the larger nanoparticles. Thus

the ordinate of the larger and the inset axes correspond to the percent frequency of particles by count for that mode, rather than the overall frequency of particles by count. Two-tailed Kolmogorov-Smirnov tests at 95% confidence indicated that the size distributions of the larger nanoparticle modes in Trials 4 and 5 were statistically identical ($p = 0.680$), but the size distributions of the smaller nanoparticles in Trials 3, 4 and 5 were statistically unique ($p < 1 \times 10^{-6}$ in all cases). This provides evidence that, for nanoparticles $< 20\,\text{nm}$, the sizes synthesized were sensitive to both the system flow rate, and the composition of the processing plasma.

An explanation for the bimodal size distributions seen in Trials 4 and 5 may be found by analogy to experimental studies of RF silane plasmas [160, 161]. In this work, similar bimodal size distributions of nanoparticles were observed, although the gas flow rates were two orders of magnitude less than the present study and the nanoparticles were of course formed in the discharge, rather than condensed upstream of it. Referring to the model proposed by [160] and recent numerical investigations [162], it is possible that the injection of nanoparticles into the plasma at the lower argon flow rates of Trials 4 and 5 allowed for the growth of larger particles by coagulation, whereas the residence time in the plasma for the nanoparticles produced in Trial 3 was sufficiently low that growth by coagulation was not favoured.

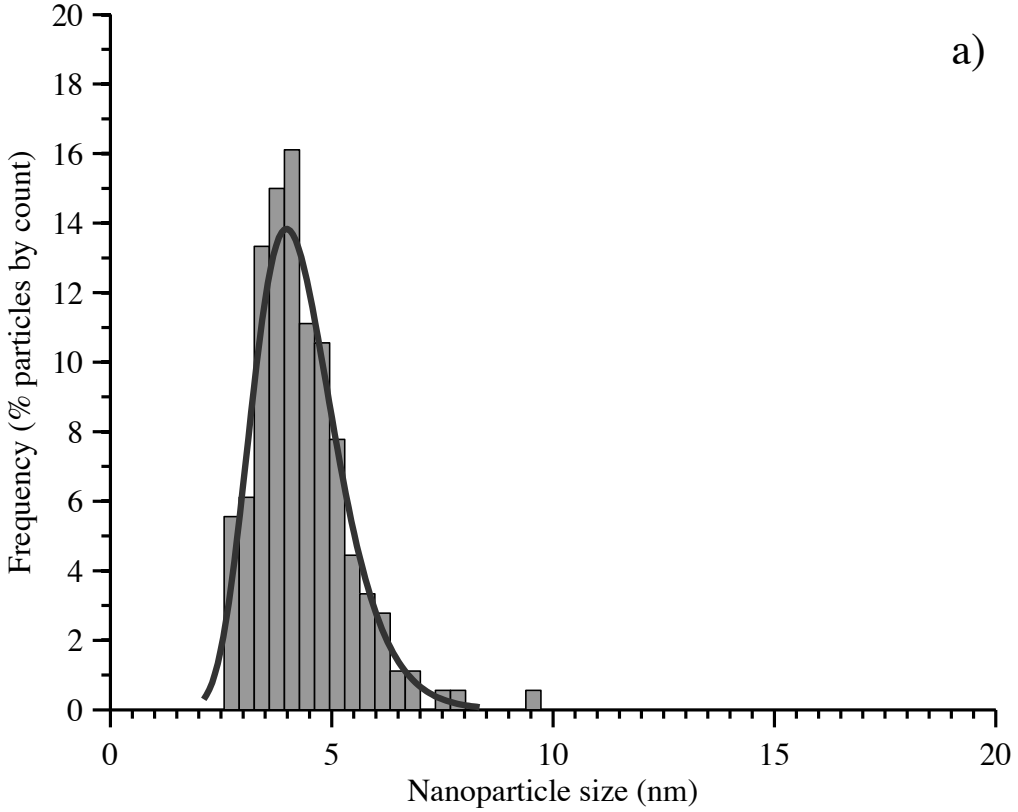
a)
Frequency (% particles by count)
Nanoparticle size (nm)
0
2
4
6
8
10
12
14
16
18
20
0
5
10
15
20

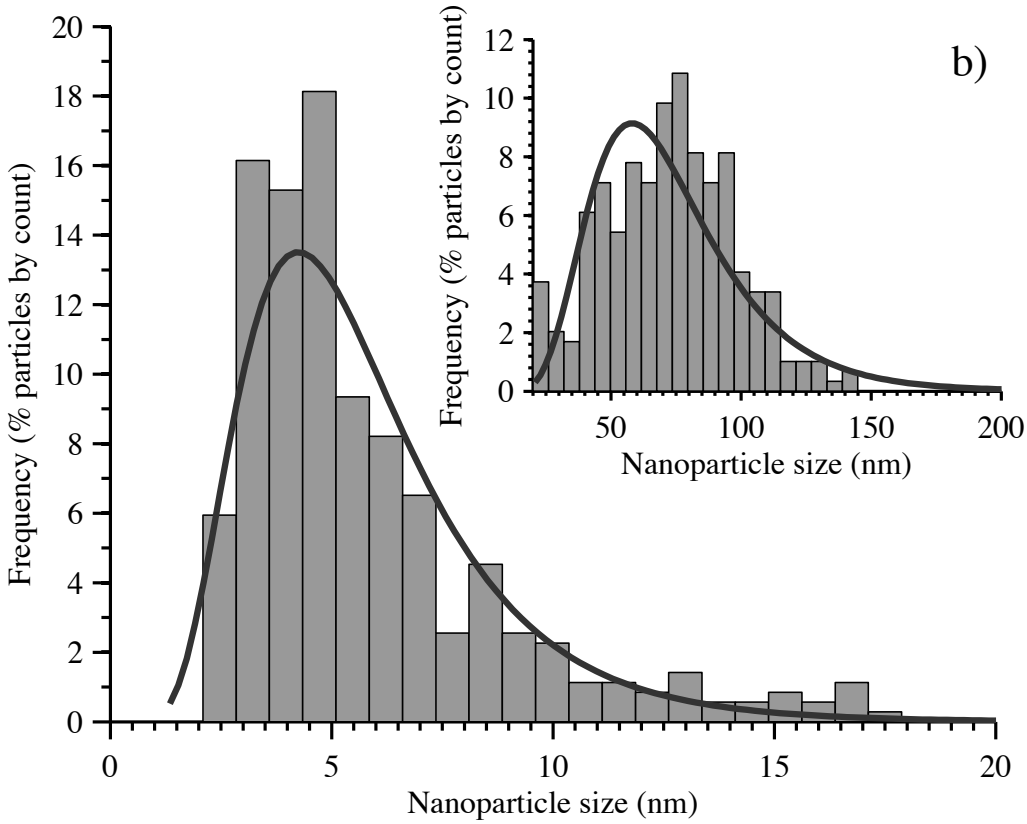
b)
Frequency (% particles by count)
Nanoparticle size (nm)
0
2
4
6
8
10
12
14
16
18
20
0
5
10
15
20
Frequency (% particles by count)
Nanoparticle size (nm)
0
2
4
6
8
10
12
50
100
150
200

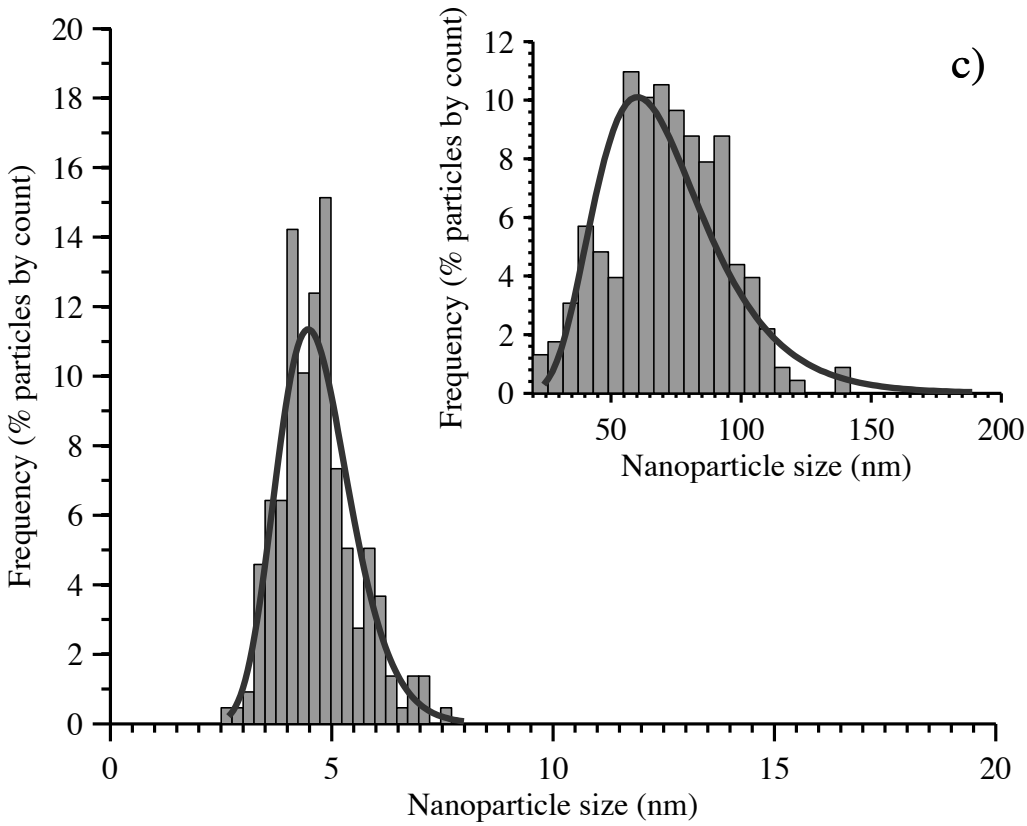


Figure 5–5: Measured nanoparticle size distributions and the fit continuous lognormal size distribution for a) Trial 3 b) Trial 4 and c) Trial 5.

Table 5–2: Summary of the means ($\mu$) and standard deviations ($\sigma$) of the corresponding normal distribution of the lognormal size distributions fit to the data in Figure 5–5. Also given are the median of the measured particle sizes and the number of measurements ($n$). Shaded rows indicate statistically identical size distributions.

| Trial | $n$ | Median | $\mu$ | $CI_{95}$ | | $\sigma$ | $CI_{95}$ | |
|---|---|---|---|---|---|---|---|---|
| | | nm | nm | nm | nm | nm | nm | nm |
| 3 | 180 | 4.2 | 1.43 | 1.40 | 1.47 | 0.229 | 0.208 | 0.255 |
| 4 | 353 | 4.6 | 1.53 | 1.51 | 1.55 | 0.183 | 0.167 | 0.202 |
| | 295 | 67.6 | 4.21 | 4.17 | 4.26 | 0.342 | 0.314 | 0.377 |
| 5 | 218 | 5.2 | 1.65 | 1.59 | 1.71 | 0.450 | 0.410 | 0.498 |
| | 228 | 67.8 | 4.22 | 4.16 | 4.28 | 0.393 | 0.355 | 0.440 |

Indexation of the the SAED patterns for Trials 3 and 4 (Figure 5–6 and 5–7) indicated a mixture of both Zn and ZnO was present. Debye-Scherrer rings unique to (100), (101), (102), and (201) for Zn, and to (100), (102), (103), (110), (200), and (203) for ZnO were identified. Given the lack of oxygen in the system during nanoparticle synthesis, this was attributed to the surface oxidation of the nanoparticles by atmospheric oxygen, as previously reported [156].

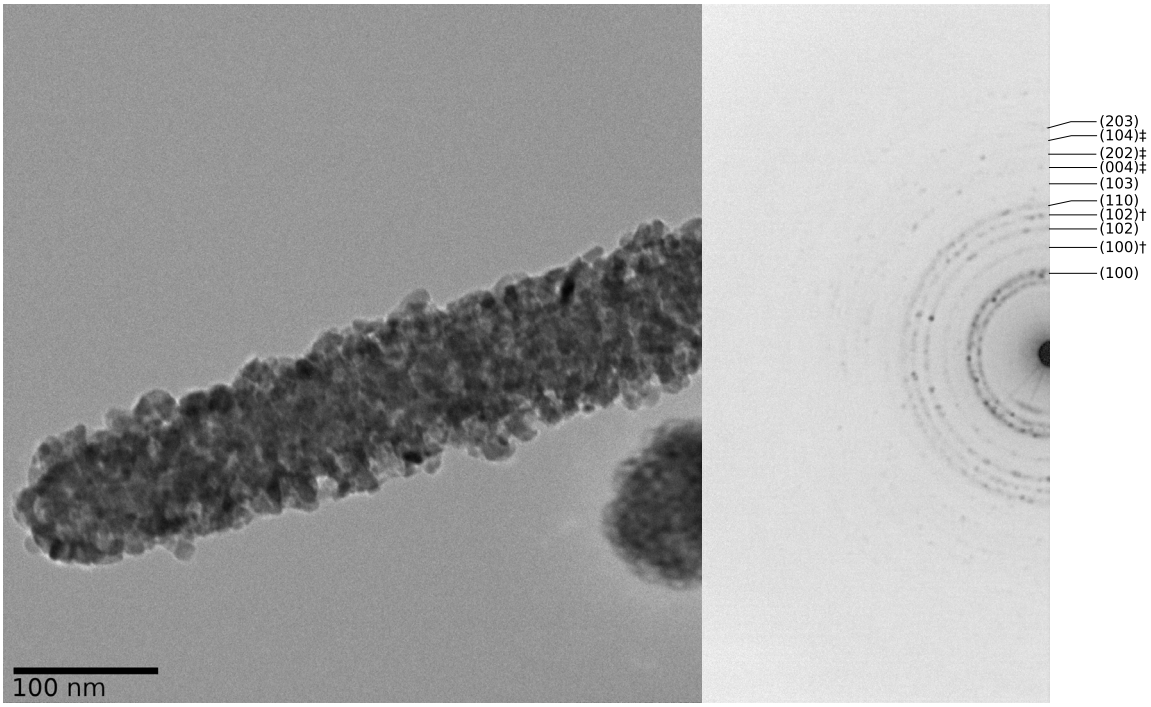


Figure 5–6: TEM image of the Zn/ZnO-CNT nanocomposite synthesized in Trial 3, and the corresponding indexed electron diffraction pattern. Unmarked indices correspond to ZnO rings, while those marked with † correspond to Zn. Rings marked with ‡ may correspond to either Zn or ZnO.

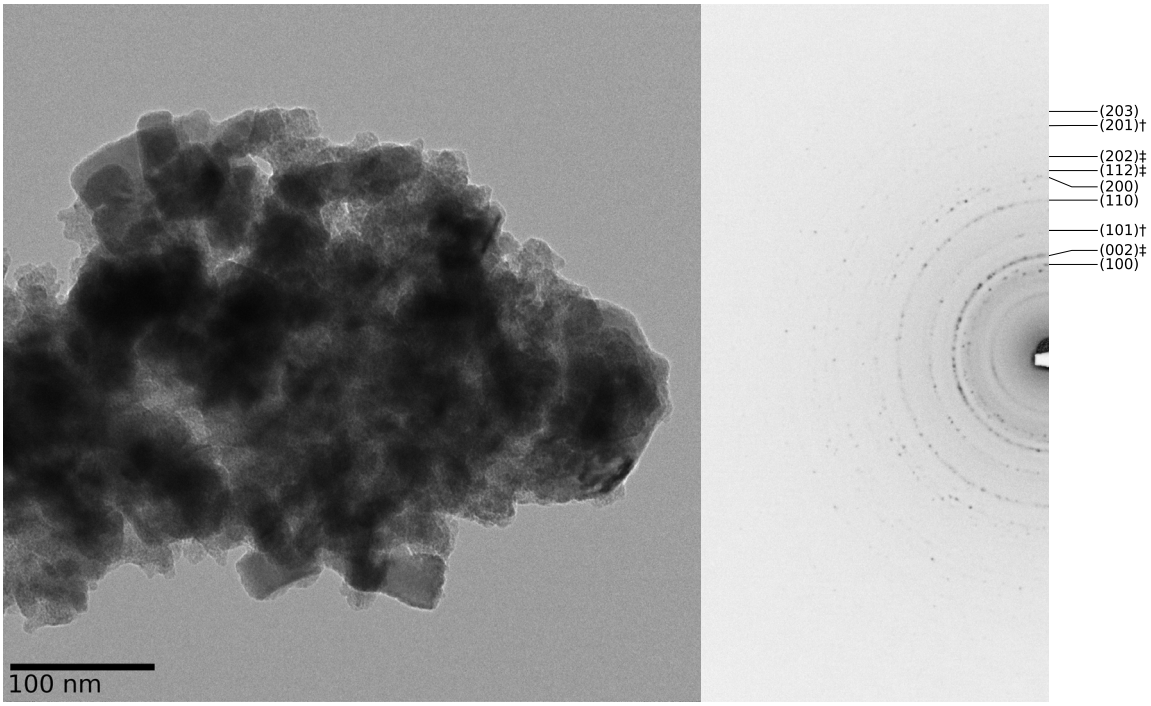


Figure 5–7: TEM image of the Zn/ZnO-CNT nanocomposite synthesized in Trial 4, and the corresponding indexed electron diffraction pattern. Unmarked indices correspond to ZnO rings, while those marked with † correspond to Zn. Rings marked with ‡ may correspond to either Zn or ZnO.

## 5.6 Conclusions

Zn/ZnO-CNT nanocomposites were synthesized using a dusty plasma process based on aerosol flow condensation of Zn nanoparticles at low pressures from an evaporative source into a capacitively-coupled RF glow discharge of both pure Ar and a $Ar/C_2H_6$ mixture. The morphologies of the nanoparticle films on the CNT substrates and the measured nanoparticle size distributions showed a dependence on both the flow rate of Ar as well as the gas composition of the plasma. Indexed SAED patterns indicated the presence of both Zn and ZnO, which was attributed to

surface oxidation of the nanoparticle coating. The structure and composition of the produced nanocomposites, with complete coverage of the CNTs with nanoparticles of mean sizes of approximately 5 nm and 70 nm, makes them interesting candidates for further study in solar energy harvesting applications for the generation of electron-hole pairs, as electrode materials with potential enhanced electron emission and photo-luminescent properties, and in catalytic and photo-catalytic applications. The described nanocomposite synthesis method provides a new approach to coating CNTs with non-thermal-plasma-treated nanoparticles that avoids liquid-phase chemistry and organometallic precursors, in contrast to other aerosol-based techniques.

### 5.6.1 Acknowledgements

The authors gratefully acknowledge the financial support of the Natural Sciences and Engineering Research Council of Canada (NSERC), le Fonds de recherche du Québec - Nature et technologies (FRQ_NT), and McGill University.

## 5.7 Bibliography

Please refer to the bibliography at the end of this thesis.

# CHAPTER 6
# Optimization of the Zn/ZnO-CNT nanocomposite synthesis conditions

## 6.1 Introduction

In this chapter, the optimization of the nanoparticle deposition conditions in the AFC reactor is described. The results and interpretation of DC glow discharge experiments for the synthesized Zn/ZnO nanocomposite cathode materials are then presented, followed by a characterization of the Zn evaporation rates observed in the synthesis procedure. The latter prompted further characterization of the nanoparticle deposition rate and the effect of the RF glow discharge on the surface chemistry of the synthesized nanoparticles, which are explored in Chapter 7.

## 6.2 Experimental Procedure

Except where noted, all procedures for the synthesis of CNT-SS nanostructures and Zn/ZnO-CNT nanocomposites on SS, and the acquisition of OES spectra, TEM images, and SEM images were executed as previously described.

## 6.3 Optimizing nanoparticle deposition conditions

During the synthesis of the nanocomposites as described in Chapter 5, it became apparent that CNT-SS meshes exposed to the same deposition conditions (i.e. for identical values of $t_d$, T, $Q_N$, $Q_S$, $Q_{PP}$, and $P_R$) could result in pronounced differences in the extent of nanoparticle coverage when these samples were examined by electron microscopy. An example of this is given in Figure 6–1, where two 3 mm diameter CNT-SS316 meshes were exposed to the nanoparticle deposition conditions

listed in Table 6–1 in separate trials. The sample shown in Figure 6–1 a) exhibited none of the mixed-mode coverage reported in Chapter 5; instead only nanoparticles approximately 10 nm in size were deposited, with some agglomerated particles in isolated areas (for example, the upper-right region of the field of view in Figure 6–1 a)). In contrast, the sample shown in Figure 6–1 b) exhibits coverage similar to that previously reported.

Table 6–1: Nanoparticle deposition conditions for Figure 6–1.

| $t_d$ | T | $Q_N$ | $Q_S$ | $Q_{PP}$ | $Q_T$ | $P_R$ | Plasma Composition |
|---|---|---|---|---|---|---|---|
| min | °C | SLPM | SLPM | SLPM | SLPM | Torr | %vol. |
| 6 | 500 | 0.84 | 0.90 | 0.324 | 2.06 | 1.8 | 99.5% Ar<br>0.5% $C_2H_6$ |

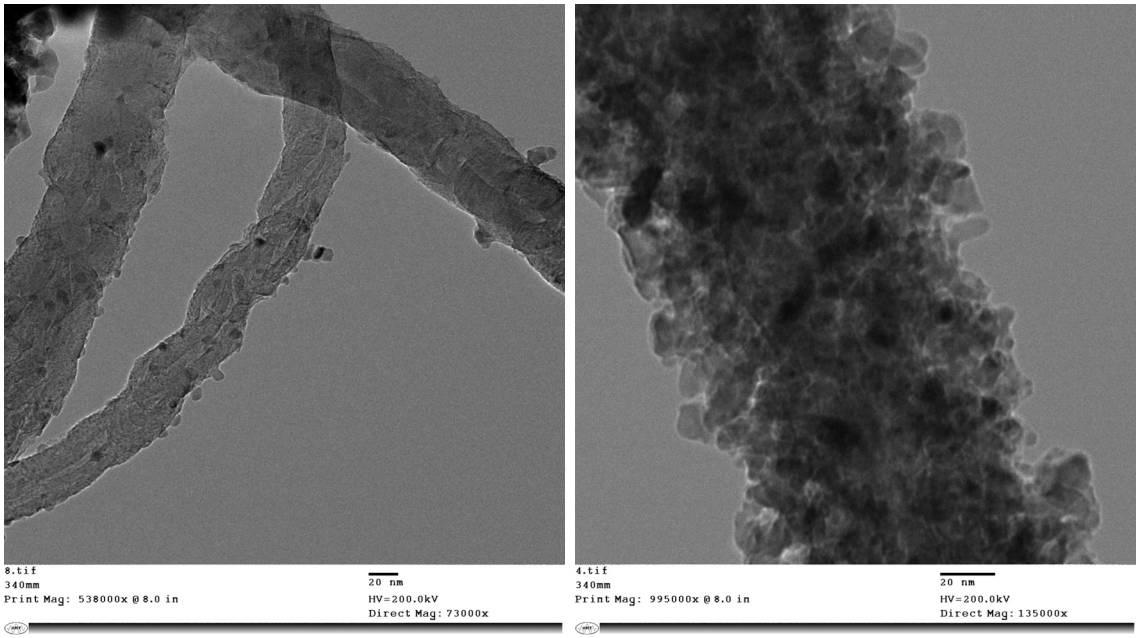


(a) Sporadic nanoparticle deposition.

(b) Nanoparticle coverage typical of that reported in Chapter 5.

Figure 6–1: Two composites produced in separate trials using the conditions listed in Table 6–1.

In a similar experiment, 3 mm diameter CNT-SS316 meshes, covered with CNTs with diameters of approximately 40 to 60 nm were exposed to the deposition conditions listed in Table 6–2 for 6 s, 1 min, and 6 min. Figure 6–2 reveals a marked increase in the deposition rate of nanoparticles on the CNTs with time. A ten-fold increase in the deposition time from Figure 6–2 a) to Figure 6–2 b) only produced an approximately 60% increase in the diameter of the coated CNT from $\sim$ 70 to $\sim$ 100 nm. However a six-fold increase in the deposition time from Figure 6–2 b) to Figure 6–2 c) produced an approximately 450% increase in the diameter of the coated CNT to $\sim$ 450 nm. This increase in the deposition rate could be attributed to the three-dimensional structure of the underlying CNTs. As compared to deposition

processes where the substrate surface area is flat and effectively two-dimensional (i.e. ignoring the effects of surface topography), the surface area available for nanoparticle deposition on the coated CNTs increases as its diameter increases. Given the collisional nature of nanoparticle deposition, the frequency with which individual nanoparticles will collide with, and be deposited on, the substrate will increase with the surface area, and so the nanoparticle deposition rate increases.

Table 6–2: Nanoparticle deposition conditions for Figure 6–2.

| | $t_d$ | T | $Q_N$ | $Q_S$ | $Q_{PP}$ | $Q_T$ | $P_R$ | Plasma Composition |
|---|---|---|---|---|---|---|---|---|
| | min | °C | SLPM | SLPM | SLPM | SLPM | Torr | %vol. |
| a) | 0.1 | 500 | 0.84 | 0.90 | 0.324 | 2.06 | 1.8 | 100% Ar |
| b) | 1 | 500 | 0.84 | 0.90 | 0.324 | 2.06 | 1.8 | 100% Ar |
| c) | 6 | 500 | 0.84 | 0.90 | 0.324 | 2.06 | 1.8 | 100% Ar |

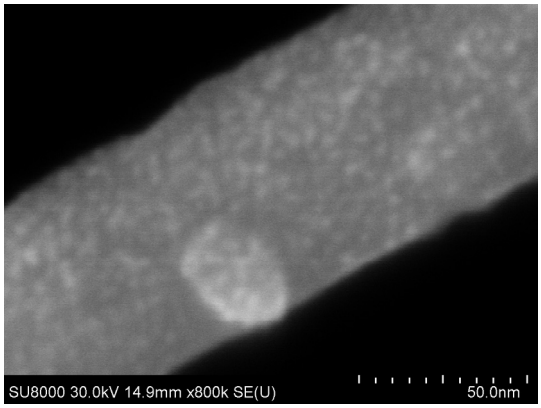


(a) Nanocomposite synthesized with $t_d = 6$ s.

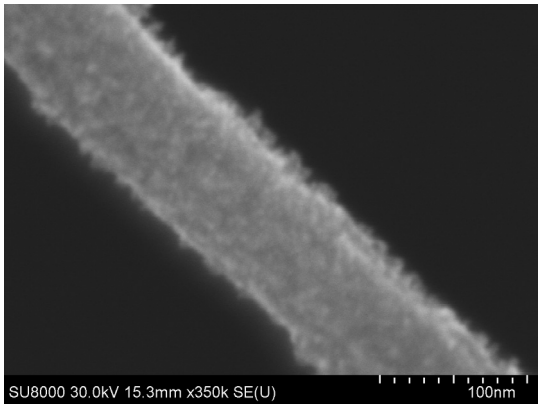


(b) Nanocomposite synthesized with $t_d = 1$ min.

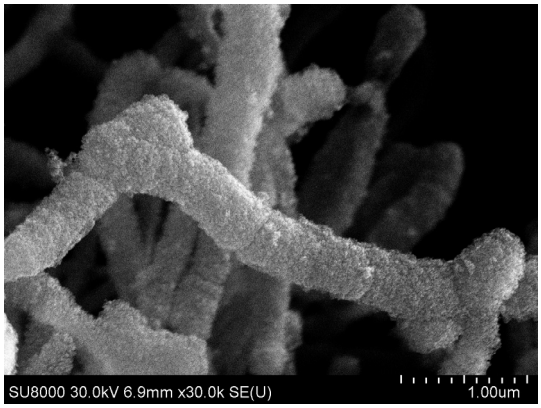


(c) Nanocomposite synthesized with $t_d = 6$ min.

Figure 6–2: Variation in the nanoparticle coating thicknesses for CNT-SS nanostructures with initial diameters of approximately 40 to 60 nm that were exposed the conditions listed in Table 6–2.

Prior to addressing the challenge imposed by the observed variability in the nanoparticle deposition rate, other practical and theoretical considerations were taken into account. For the rotameter used to meter the gas flow rate through the nozzle, the upper limit of $Q_N$ is 4.43 SLPM for argon. However at this flow rate, the crucible was often dislodged as a result of the 5 mm distance between the nozzle orifice and crucible edge. Consequently, a useable upper limit of $Q_N = 2.00$ SLPM was established, which prevented crucible displacement.

Secondly, the nanoparticle deposition rate for nanoparticle synthesis had to be minimized, since heavily-coated CNT-SS samples, such as that shown in Figure 6–3, could not be used to ignite DC glow discharges when used as cathodes in experiments. Given the semiconducting nature of ZnO, it is reasonable to assume that the thick film of the as-deposited nanoparticles increased the effective resistance in the circuit of the DC glow discharge, increasing the slope of the load line such that, when the DC power supply provided its maximum potential of 600 V, negligible currents were observed. Moreover, it has been previously reported that the electrical resistivity of similar porous ZnO nanoparticle films is higher than films with less porosity and/or larger particle sizes [163, 164]. Thus, it was of interest to investigate and evaluate methods of controlling the thicknesses of the nanoparticle layers deposited in order to minimize the thicknesses of the layers deposited, thereby minimizing the effect of electrical resistances introduced by the deposition of the nanoparticles upon the CNT substrates.

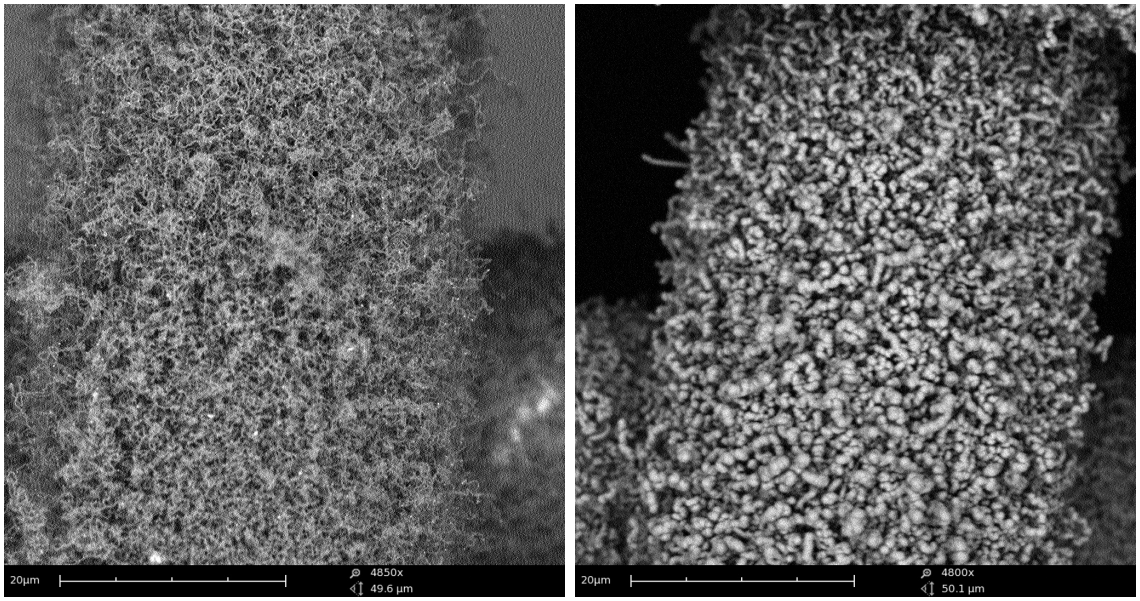


(a) CNT-SS substrate prior to coating. (b) Heavy nanoparticle coating after deposition.

Figure 6–3: CNT-SS nanostructure before and after nanoparticle deposition using the same conditions listed in Table 6–1, but for $t_d = 15\,\text{min}$.

Similar motivation for reducing the nanoparticle deposition rate to levels that would produce usable cathode materials was provided by other studies of electron emission from nanoparticle-CNT composite materials. Enhanced electron field-emission has been reported for decorated CNTs, as reviewed in Section 2.3.2, thus the interest in this project was to produce structurally similar materials, i.e. CNTs with very thin or sporadic coatings of nanoparticles with diameters on the order of 10 nm.

Consideration of the evaporation-condensation mechanism of nanoparticle formation (Section 2.4.2.1) suggested process conditions to synthesize the nanoparticle coatings described above. By increasing the cooling rate of the zinc vapour and

consequently the saturation ratio in the system, the resulting increased driving force for nanoparticle nucleation would favour the increased production of small nanoparticles. In the deposition system, this suggested increasing the value of $Q_N$. Yet with the simultaneous objective of achieving low nanoparticle deposition rates to yield usable cathode materials when exposing the CNT-SS substrates to the process stream, the use of decreased values of $Q_N$ was implied. Examination of the literature indicated that the average synthesized nanoparticle diameter in similar systems was not a strong function of the nozzle gas flow rate; for systems that produced nanoparticles with median diameters less than 20 nm, the median diameter was altered by less than 10 nm for gas flow rates of 0–1 SLPM [113] and for increments of 5 SLPM [112]. These studies also reported a similar trend with respect to the median nanoparticle size and the total gas flow rates. Thus, in the interests of lower deposition rates, it appeared that not only low values of $Q_N$, but low total gas flow rates would be useful. With regards to other process parameters, using reduced temperatures of the metal vapour source should favour reduced deposition rates resulting from lower evaporation rates [112]. Reduced pressures also favour the production of smaller nanoparticles as a consequence of the reduced metal vapour density [97].

Overall, the above suggested the following process parameters for minimizing the observed nanoparticle deposition rates in order to reproduce cathode materials for testing in the DC glow discharge apparatus. Firstly, the flow rates of argon for the nozzle and sheath gas flow rates were set to values near their lower metered limit,

that is $Q_N = 0.84$ SLPM and $Q_S = 0.90$ SLPM, respectively. Whereas $C_2H_6$ concentrations between 0.05 and 1%vol. have been previously used to deposit organic functional groups and plasma polymer coatings on nanoparticles in RF glow discharges [28, 27, 151], and given an upper limit of 10 sccm for the metered flow rate of $C_2H_6$ through its MFC, the value of $Q_{PP}$ was adjusted so that the total concentration of $C_2H_6$ in contact with the synthesized nanoparticles could be controlled between 0.1 and 0.5%vol. For the reactor pressure, a base pressure of approximately 30 mTorr could be achieved, and with a nominal pumping speed of $6.5\,m^3h^{-1}$ for the rotary vane vacuum pump (Pascal 2006SD, Pfeiffer Vacuum, Germany), the lower limit of the reactor pressure was $P_R = 1.8$ Torr at a total gas flow rate of $Q_T = 2.06$ SLPM.

With the observed variability in the nanoparticle deposition rate, a strategy of testing small batches of replicated composite cathode materials in the DC glow discharge was adopted, and this is described below in Section 6.4. In order to characterize the variability of the the nanoparticle production process, a brief investigation of the evaporation rate of zinc in the process was undertaken in parallel, which is described in Section 6.4.3.

## 6.4 Zn/ZnO-CNT composite cathode evaluation

Following the above strategy, a number of experiments were performed for small batches of Zn/ZnO-CNT composites, which were produced from the same batch of CNT-SS316 substrates. In all cases and regardless of the deposition treatment on the CNTs, no statistically significant reduction in the sustaining voltage was observed over the entire duration of experiments when the Zn/ZnO-CNT composites were compared to controls of untreated CNT-SS316 substrates, or bare, untreated

SS316. Presented below are the results of one such experiment as an example of the investigations conducted.

### 6.4.1 Effect of nanoparticle treatment on DC glow discharge sustaining voltages

In this experiment, the Zn/ZnO-CNT composites listed in Table 6–3 were synthesized and tested in the DC glow discharge apparatus previously described using $N_2$ at a system pressure of 3.5 Torr and 5 mA current. Whereas prior experiments had indicated the Zn/ZnO-CNT nanocomposites synthesized from RF glow discharges containing only argon were also subject to degradation by ion- and molecular-bombardment at the cathode, ethane was introduced to the RF plasma to surface-treat the synthesized nanoparticles with functional groups.

Trials 1, 7, and 8 were controls of CNT-SS316 that were not exposed to nanoparticle deposition, while Trials 2–6 and Trials 9–12. The measured sustaining voltages are presented in Figures 6–4, 6–5, 6–6, and 6–7, below.

Table 6–3: Sample synthesis conditions to evaluate the effect of Zn/ZnO and $C_2H_6$-treated Zn/ZnO coatings on CNT-SS316 substrates as cathode materials for sustaining DC glow discharges.

| Trial | $t_d$ | T | $Q_N$ | $Q_S$ | $Q_{PP}$ | $Q_T$ | $P_R$ | Plasma Composition |
|---|---|---|---|---|---|---|---|---|
| | min | °C | SLPM | SLPM | SLPM | SLPM | Torr | %vol. |
| 1 | N/A | N/A | N/A | N/A | N/A | N/A | N/A | N/A |
| 2 | 1 | 500 | 0.84 | 0.90 | 0.324 | 2.06 | 1.8 | 99.5% Ar<br>0.5% $C_2H_6$ |
| 3 | 1 | 500 | 0.84 | 0.90 | 0.324 | 2.06 | 1.8 | 99.5% Ar<br>0.5% $C_2H_6$ |
| 4 | 1 | 500 | 0.84 | 0.90 | 0.324 | 2.06 | 1.8 | 100% Ar |
| 5 | 1 | 500 | 0.84 | 0.90 | 0.324 | 2.06 | 1.8 | 100% Ar |
| 6 | 1 | 500 | 0.84 | 0.90 | 0.324 | 2.06 | 1.8 | 100% Ar |
| 7 | N/A | N/A | N/A | N/A | N/A | N/A | N/A | N/A |
| 8 | N/A | N/A | N/A | N/A | N/A | N/A | N/A | N/A |
| 9 | 1 | 500 | 0.84 | 0.90 | 0.324 | 2.06 | 1.8 | 99.5% Ar<br>0.5% $C_2H_6$ |
| 10 | 1 | 500 | 0.84 | 0.90 | 0.324 | 2.06 | 1.8 | 99.5% Ar<br>0.5% $C_2H_6$ |
| 11 | 1 | 500 | 0.84 | 0.90 | 0.324 | 2.06 | 1.8 | 99.9% Ar<br>0.1% $C_2H_6$ |
| 12 | 1 | 500 | 0.84 | 0.90 | 0.324 | 2.06 | 1.8 | 99.9% Ar<br>0.1% $C_2H_6$ |
| 13 | 5 | 500 | 0.84 | 0.90 | 0.324 | 2.06 | 1.8 | 99.5% Ar<br>0.5% $C_2H_6$ |
| 14 | 5 | 500 | 0.84 | 0.90 | 0.324 | 2.06 | 1.8 | 99.9% Ar<br>0.1% $C_2H_6$ |

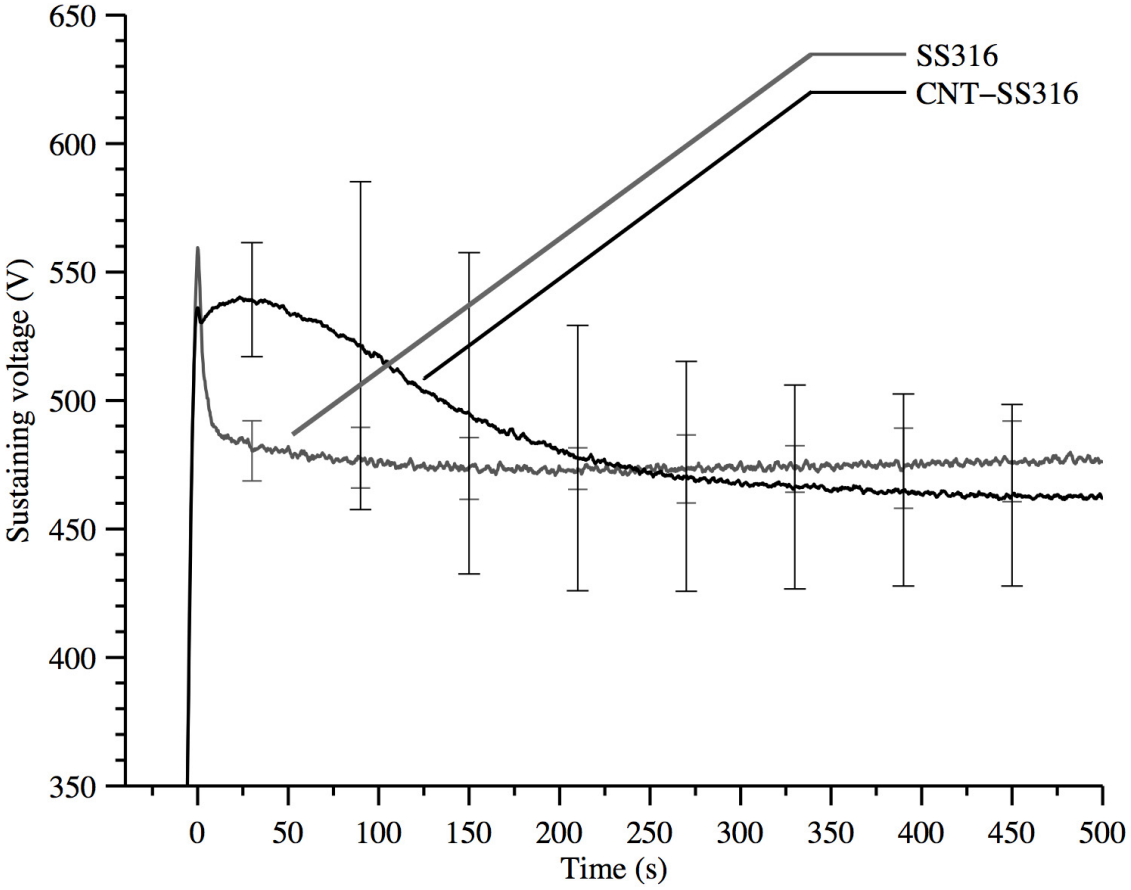


Figure 6–4: A comparison of the average sustaining voltages required for the controls of untreated SS316 ($n = 3$) and the control samples from Trials 1, 7, and 8. Error bars indicate 95% confidence intervals.

In Figure 6–4, a comparison is made between the two controls used in this experiment: untreated samples of SS316 and CNT-SS316. The only statistically significant difference between the two trials occurred within approximately 60 s after breakdown at t = 0 s, where the CNTs coating the SS316 acted to increase the sustaining voltage required. Contrary to the results presented in Chapter 3, the erosion of the CNTs resulted in both controls requiring statistically similar sustaining

voltages at approximately t = 100 s. This could be attributed to the 0.5 Torr increase in pressure used in this experiment, as the current density (and thus the rate of bombardment of the cathode) in abnormal glow discharges scales with the square of the pressure [2]. Thus it is possible that this higher rate of CNT erosion led to the statistically similar performance of the CNT-SS316 cathode to the control after less than 5 min of exposure to the DC glow discharge.

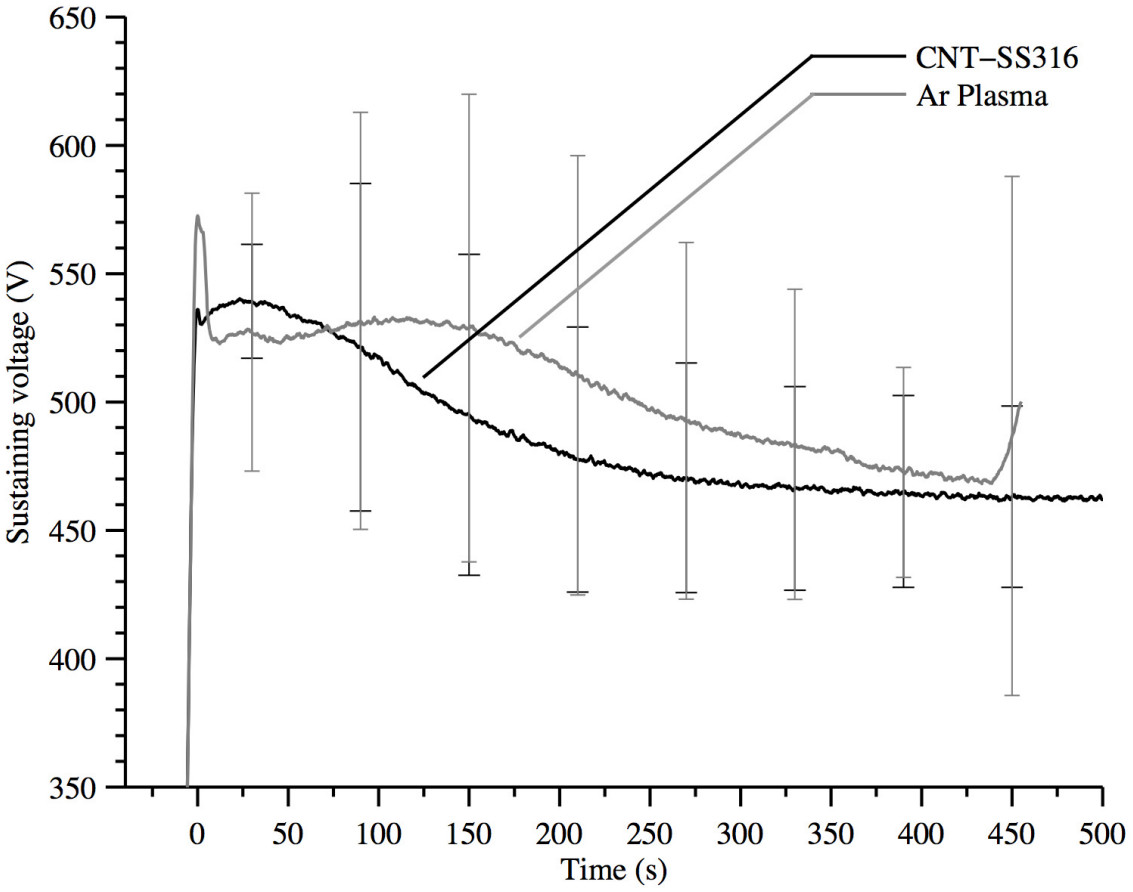


Figure 6–5: A comparison of the average sustaining voltages required for Trials 4–6, as compared to the CNT-SS316 control ($n = 3$). Error bars indicate 95% confidence intervals.

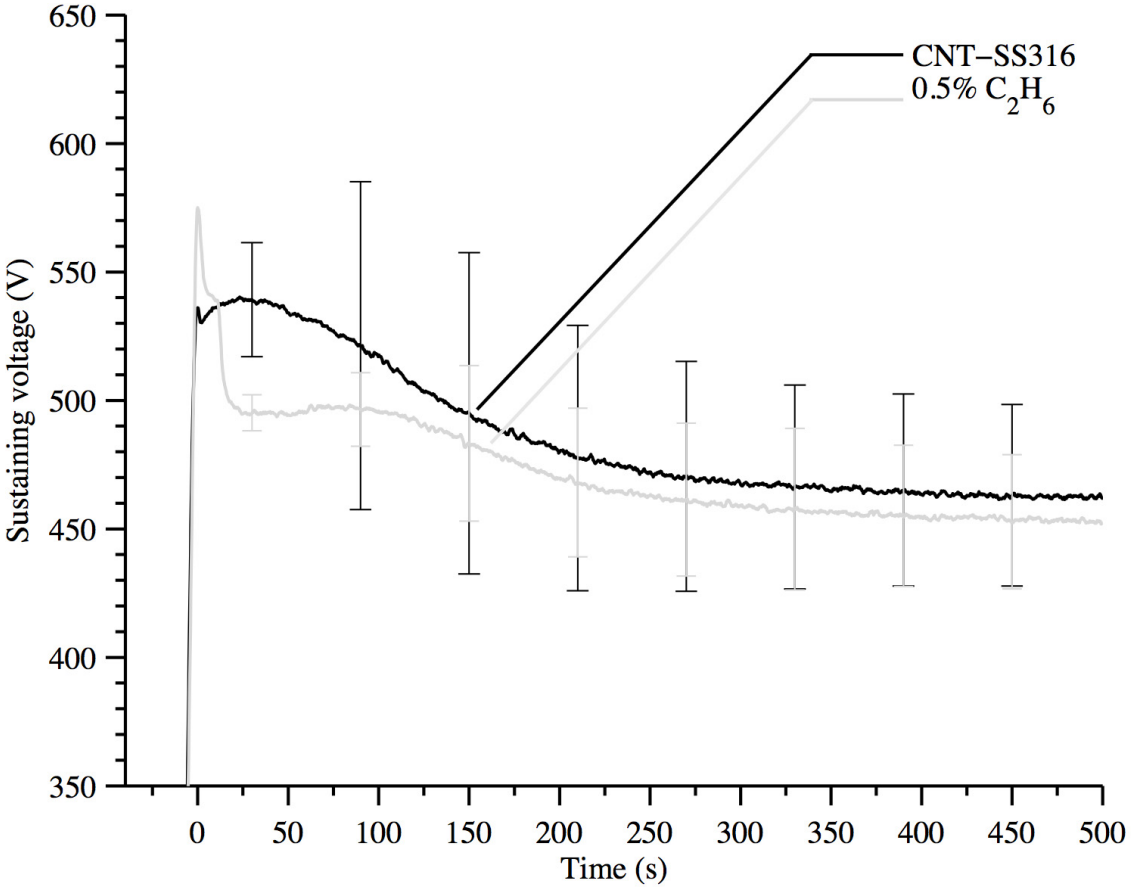


Figure 6–6: A comparison of the average sustaining voltages required for Trials 2, 3, 9, and 10, as compared to the CNT-SS316 control ($n = 3$). Error bars indicate 95% confidence intervals.

Treatment of the CNT-SS316 substrates with either Zn/ZnO nanoparticles deposited from RF glow discharges containing only argon (Figure 6–5) or 0.5%vol. $C_2H_6$ (Figure 6–6) resulted in cathode materials which required sustaining voltages statistically similar to the CNT-SS316 and SS316 controls. The sole exception to this in these experiments occurred at approximately t = 30 s in Figure 6–6 when less voltage was required to sustain the DC glow discharge for the $C_2H_6$-treated sample than

the CNT-SS316 control. This indicated that, for less than 30 s, the treatment was effective in reducing the sustaining voltage required, as compared to the untreated CNT-SS316. However, this point is moot in consideration of Figure 6–7, where at this time the average sustaining voltage required for the $C_2H_6$-treated composite was statistically similar to the untreated SS316 control. In terms of utility, this indicates that the as-synthesized $C_2H_6$-treated Zn/ZnO-CNT composite performed no better than the raw cathode material. It should be noted that in Figure 6–5, the sudden rise in the sustaining voltage at approximately t = 430 s was the result of the sudden extinguishment of the DC glow discharge when testing Trial 6, which was attributed to a fluctuation in the DC power supply. Once the plasma was extinguished, the power supply attempted to re-ignite the discharge by increasing the system voltage, however the trial was aborted at this point.

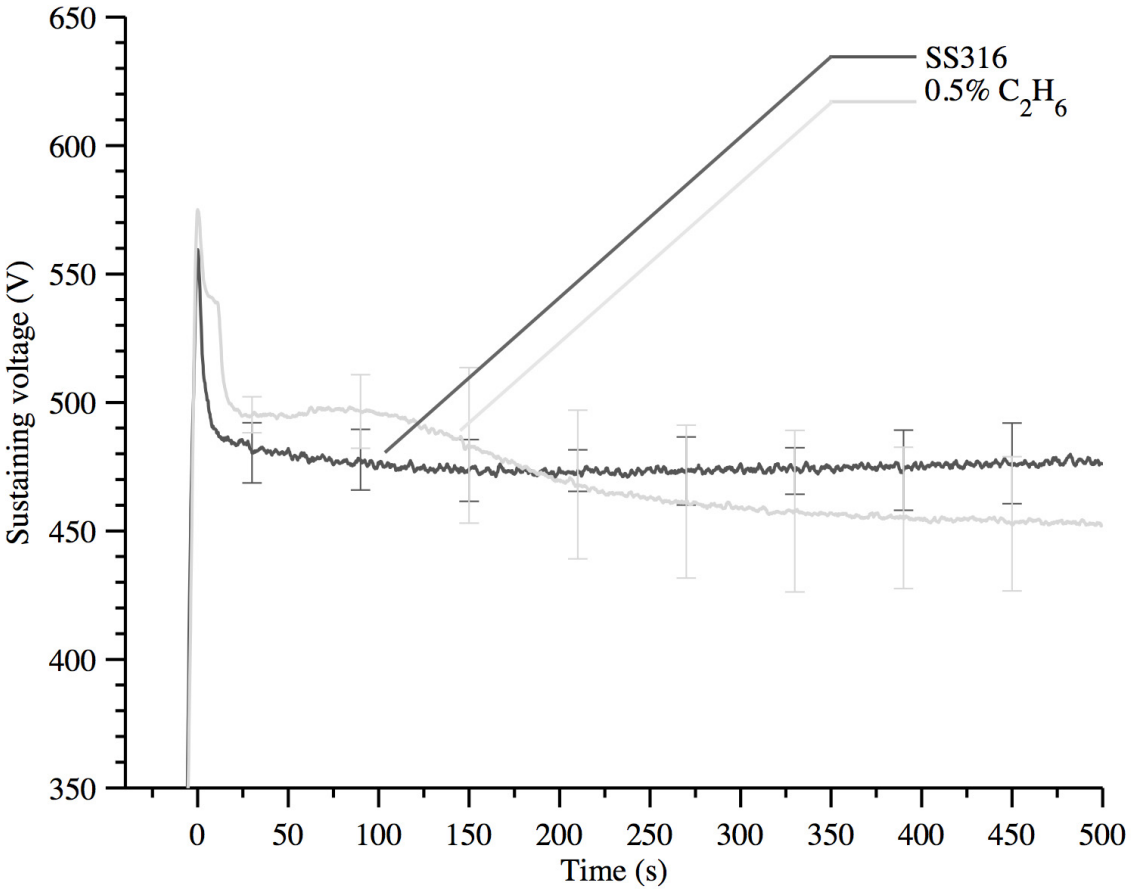


Figure 6–7: A comparison of the average sustaining voltages required for Trials 2, 3, 9, and 10, as compared to the untreated SS316 control ($n = 3$). Error bars indicate 95% confidence intervals.

Shown in Figures 6–8 and 6–9 are the OES spectra of Trials 2 and 4, which were typical of their replicates in Trials 3, 9, and 10, and Trials 5 and 6, respectively. OES spectra for all trials were examined for evidence of CNT degradation or the liberation of nanoparticles from the CNTs. However, the spectra were invariant with time, moreover, the peaks present could only be attributed to $N_2$ and $N_2^+$, as per Chapter 3. This was attributed to the much smaller concentrations of CNTs and

Zn/ZnO nanoparticles present, relative to the concentration of $N_2$ in the DC glow discharge system.

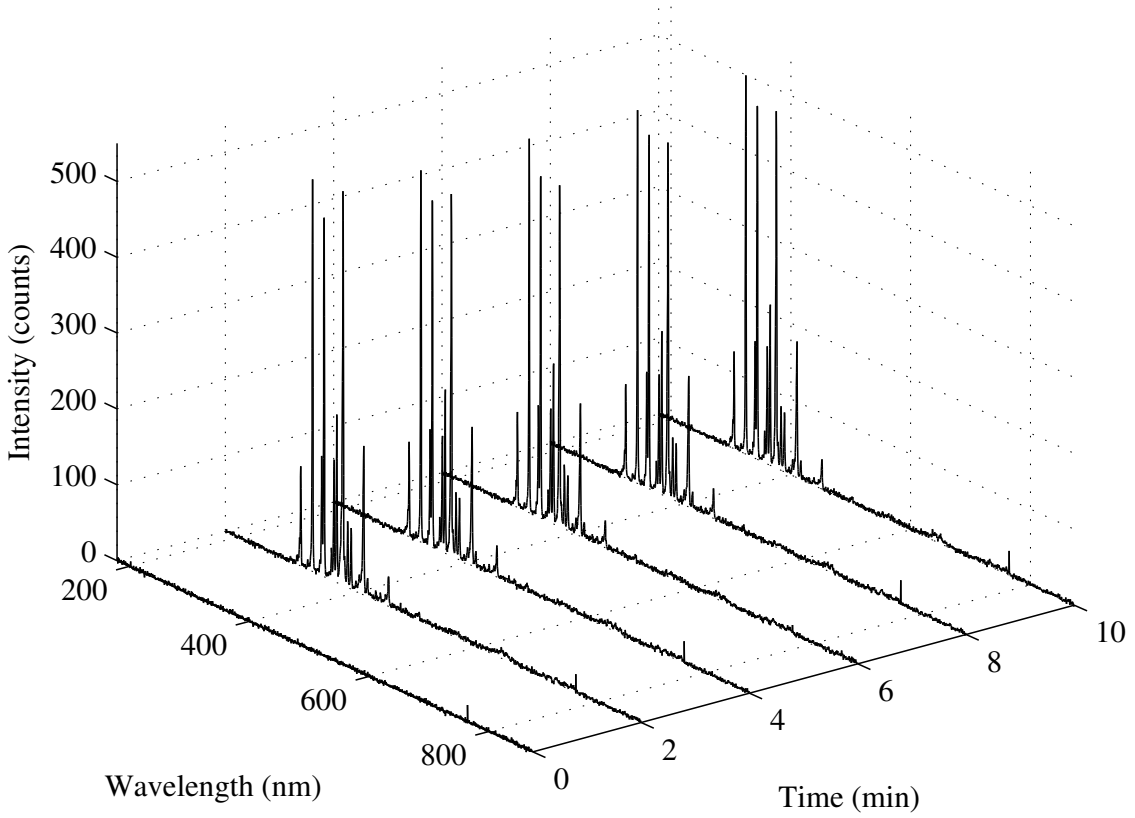


Figure 6–8: OES spectra of Trial 2 as a function of time. No evidence of carbon or zinc erosion was observed, despite the presence of 0.5% $C_2H_6$ in the RF plasma.

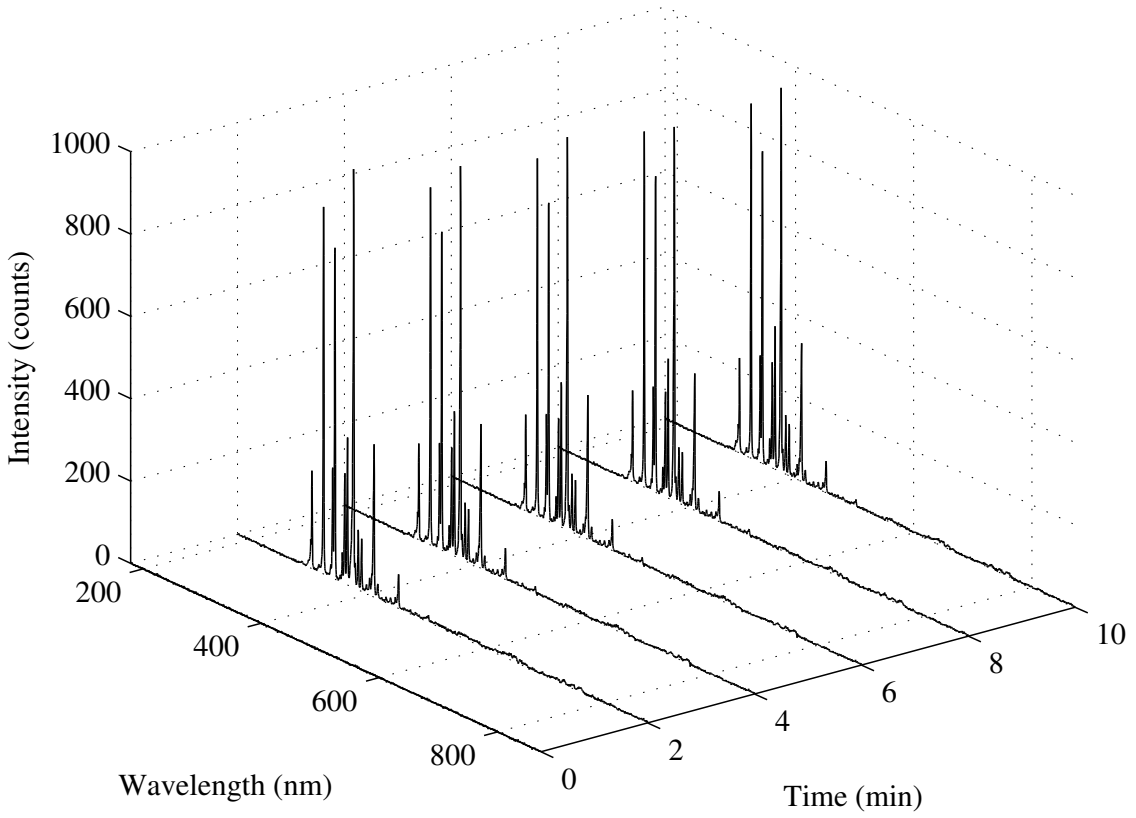


Figure 6–9: OES spectra of Trial 4 as a function of time. No evidence of carbon or zinc erosion was observed.

Evidence of the degradation of the Zn/ZnO composite coatings was observed in SEM images of the synthesized cathodes by comparing images of the cathode surfaces before and after testing in the DC glow discharge. For example, shown in Figure 6–10 is the cathode surface of Trial 4, while Figure 6–11 shows that of Trial 2. Generally, the residues of the composite coating appeared, by visual inspection, to be more pronounced in samples composed of nanoparticles treated with ethane (Figure 6–11) than those that were treated with RF plasmas containing only argon. However,

this observation appeared to have no statistically significant effect on the sustaining voltages required during testing.

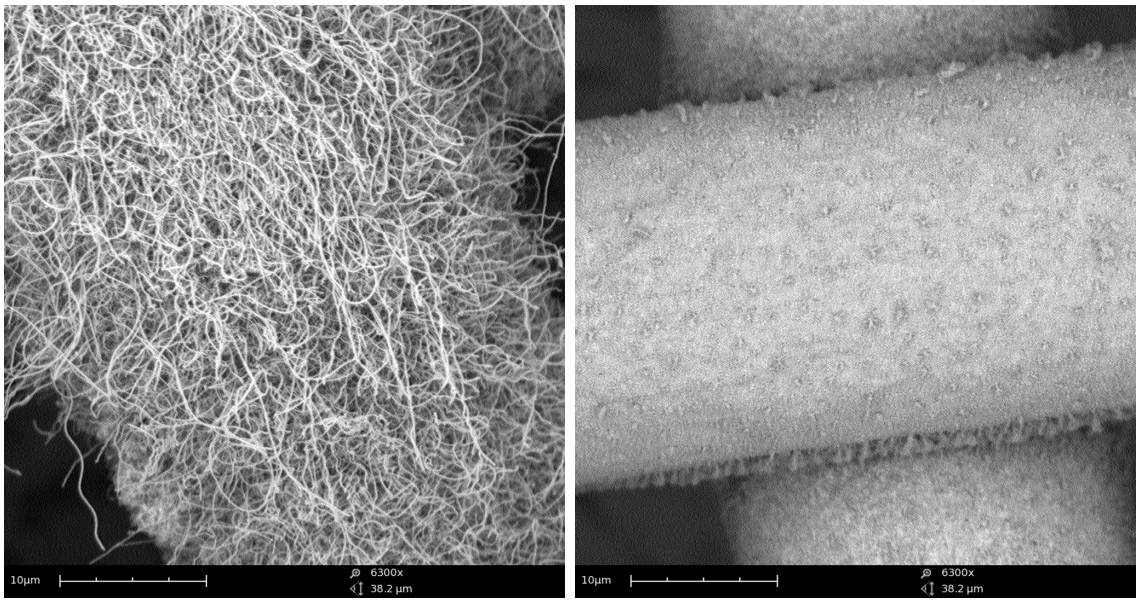


(a) Before exposure to the DC glow discharge. (b) After cathode testing.

Figure 6–10: SEM images of the nanocomposite cathode produced in Trial 4, before and after testing in a DC glow discharge in $N_2$ at 3.5 Torr, 5 mA for 10 min.

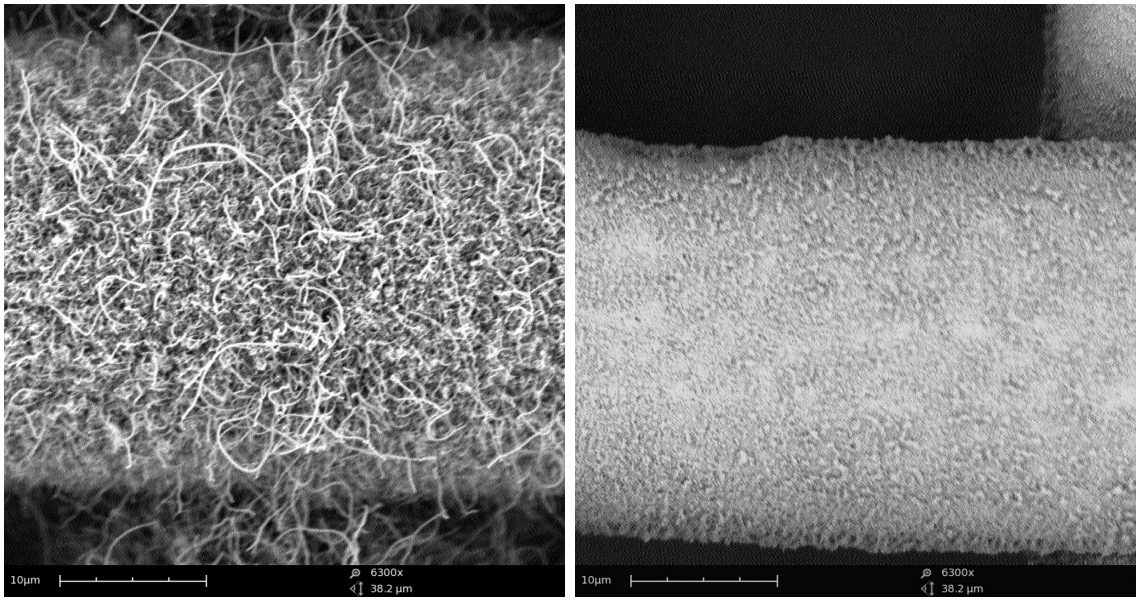


(a) Before exposure to the DC glow discharge. (b) After cathode testing.

Figure 6–11: SEM images of the nanocomposite cathode produced in Trial 2, before and after testing in a DC glow discharge in $N_2$ at 3.5 Torr, 5 mA for 10 min.

### 6.4.2 Sample performance variability during testing

Comparing the performance of the synthesized Zn/ZnO-CNT nanocomposite cathodes against controls of CNT-SS cathodes was hindered in this project by the observed variance in the sustaining voltage measurements for both types of samples, as indicated by the relatively large and overlapping 95% confidence intervals in the measured sustaining voltages of samples tested in the DC glow discharge. Given the variability observed in SEM and TEM images of the number of nanoparticles deposited on CNT substrates for identical experimental conditions in the AFC-RF deposition apparatus, the amount of nanoparticle deposition from trial-to-trial is the likely source of the observed variance in the sustaining voltage measurements.

However, the SS controls exhibited significantly less variance when replicate measurements were made in the DC glow discharge apparatus. Consequently, the following presents a brief discussion of the statistical power of these tests by using the results of Section 6.4.1 as an example.

In the case where the null hypothesis is false when testing two normally-distributed, random variables with unknown variances, then the distribution of the test statistic for Student's $t$-test is unknown. Consequently, no operating characteristic curves or tables of values exist to determine the minimum difference in means that can be discriminated in using a two-tailed $t$-test [165]. However, if we consider the performance of replicated trials in Table 6–3 as representative of that treatment, some insight can be inferred as to the difference in means that can be detected at a given power, and the number of samples required to do so.

For example, since the SS316 control of Figure 6–7 was not subjected either to CNT growth or Zn/ZnO nanoparticle deposition, then the variance observed in this sample can be attributed to the measurement error if we assume the control samples were identical. Using the mean measured sustaining voltage and the sample variance as estimates of the true mean and variance, the minimum mean that could be discriminated with a power of 0.95 was calculated at each point of the measured values of the SS316 replicates using MATLAB® for samples sizes of $n = 3$ and $n = 5$. The results of this, shown in Figure 6–12, indicate that for a hypothetical sample of $n = 3$ or $n = 5$, with a sample variance statistically equivalent to that of the measurement error, then a shift in the mean sustaining voltage of approximately 20 V and 10 V, respectively, could be detected with a probability of 95%.

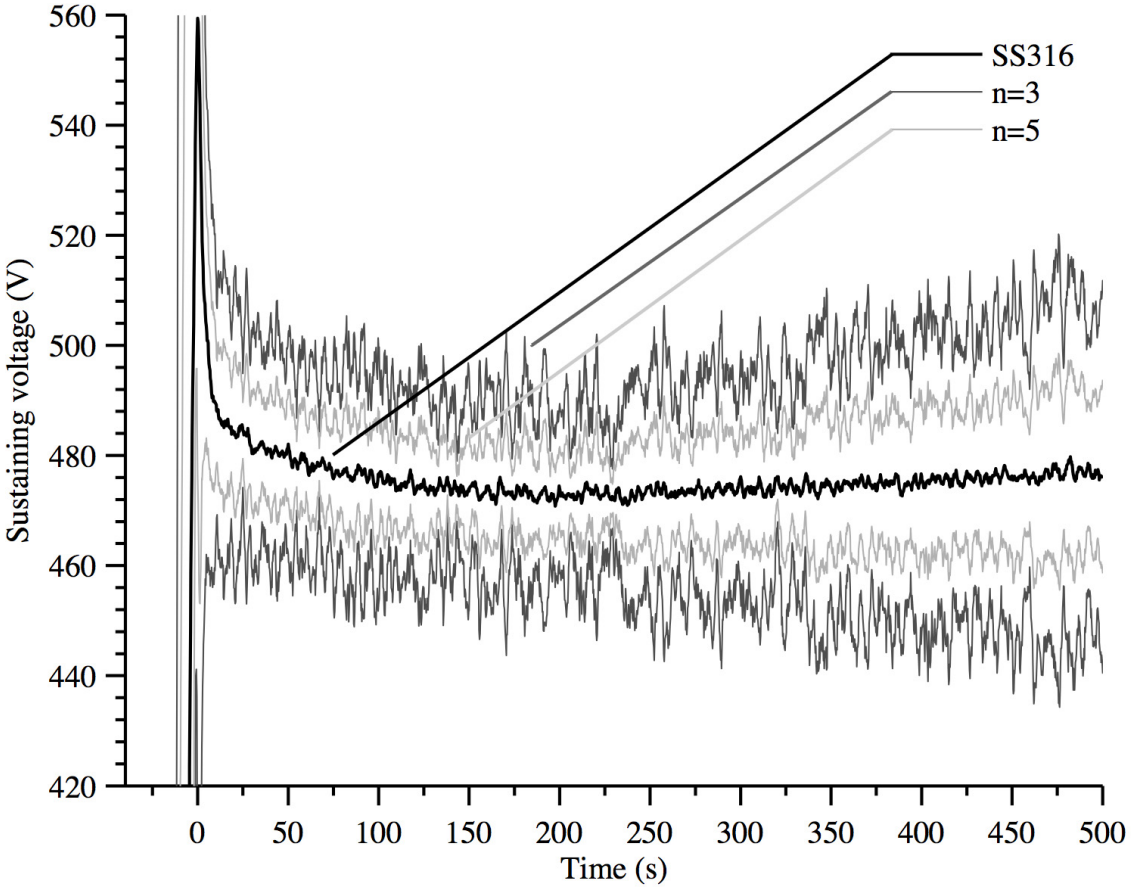


Figure 6–12: Minimum difference in means that can be discriminated with a power of 0.95 for $n = 3$ and $n = 5$, based on the mean measurements of the SS316 control as representative of the measurement error.

However, the variances of the CNT-SS316 controls and those of the synthesized composites were significantly different than that of the SS316 control, thus there is no way to calculate the difference in means that can be discriminated between these samples and the SS316 control. Yet, to gain a better sense of the obfuscating effect of the increased observed variances in the CNT-SS316 and composite samples, the same calculation can be performed on these samples in order to assess what shift

in the mean sustaining voltage could be detected for a presumably different level of treatment. In this analysis, the implicit assumption is that any hypothetical sample with a shift in the sustaining voltage caused by a treatment would have a statistically equivalent variance to that of the sample to which it was being compared.

For example, this analysis was performed on the mean of Trials 2, 3, 9, and 10, and is shown in Figure 6–13. Since these trials pertained to composite cathodes, the upper and lower bounds shown for $n = 3$ and $n = 5$ contain the effect of both measurement error and variance from the sample treatments. This indicates that if, for example, a set of three additional replicated samples were to be synthesized and tested against the mean values of the 0.5%vol. $C_2H_6$ treatment of Trials 2, 3, 9, and 10, only an approximately 60 V difference in the sustaining voltage would be detected with a probability of 95%.

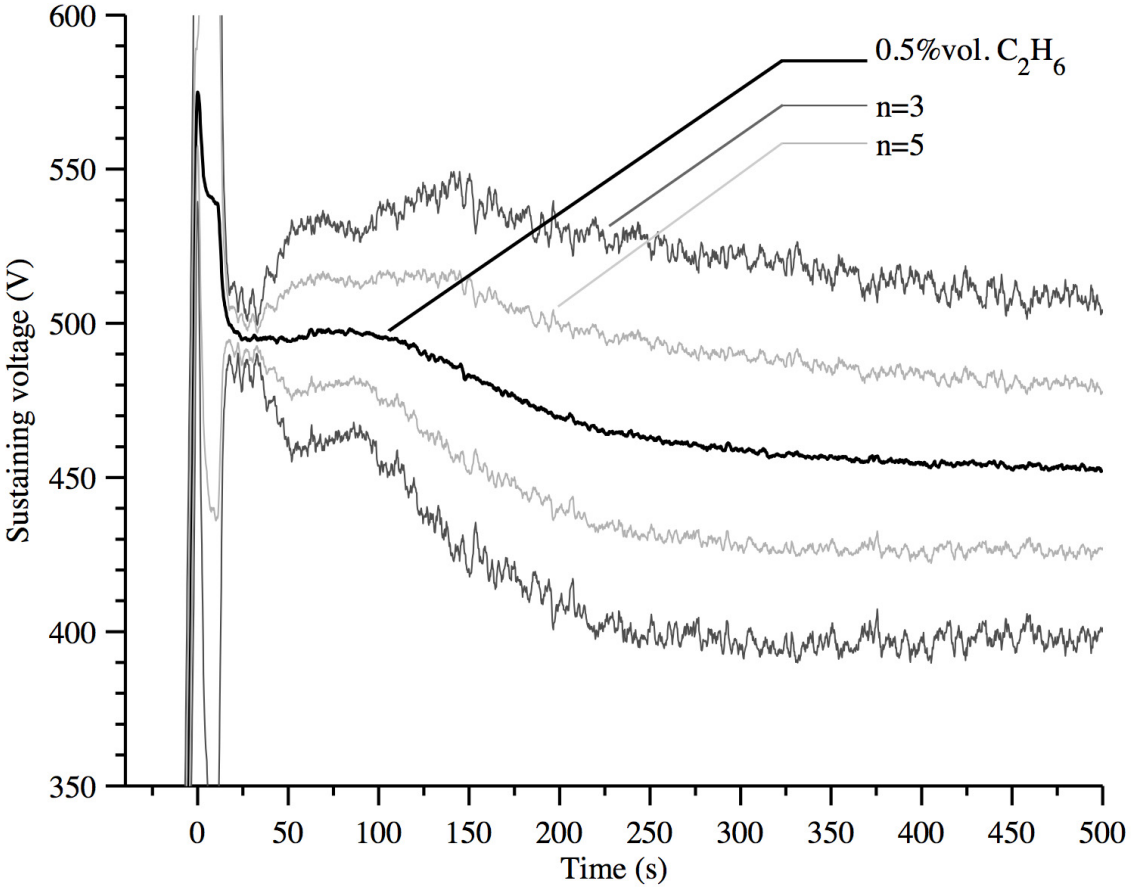


Figure 6–13: Minimum difference in means that can be discriminated for $n = 3$ and $n = 5$ based on the mean measurements of Trials 2, 3, 9, and 10 as an illustrative example of the obfuscating effect of the sample variance.

In this analysis, the increased variance in the cathode performance that was caused by the synthesis of CNTs or Zn/ZnO-CNT composites may have prevented the detection of any reduction in the DC glow discharge sustaining voltage. An example of this may have occurred in Trial 10, shown in Figure 6–14. If the variance of the 0.5%vol. $C_2H_6$ treatment had a statistically equivalent sample variance to that of the SS316 control, then the ultimate reduction in the sustaining voltage of Trial 10

would have been detected as significant. However, calculation of the sample mean and variances from Trials 2, 3, 9, and 10, and the testing of these two populations at 95% significance, as illustrated in Figure 6–7 indicated that no such improvement occurred. However, given that a rather large reduction in the sustaining voltage is expected, on the order of 100 V [13], the most likely explanation remains that the applied electric field, as discussed in Chapter 3, was at least an order of magnitude too small to initiate the field electron emission required.

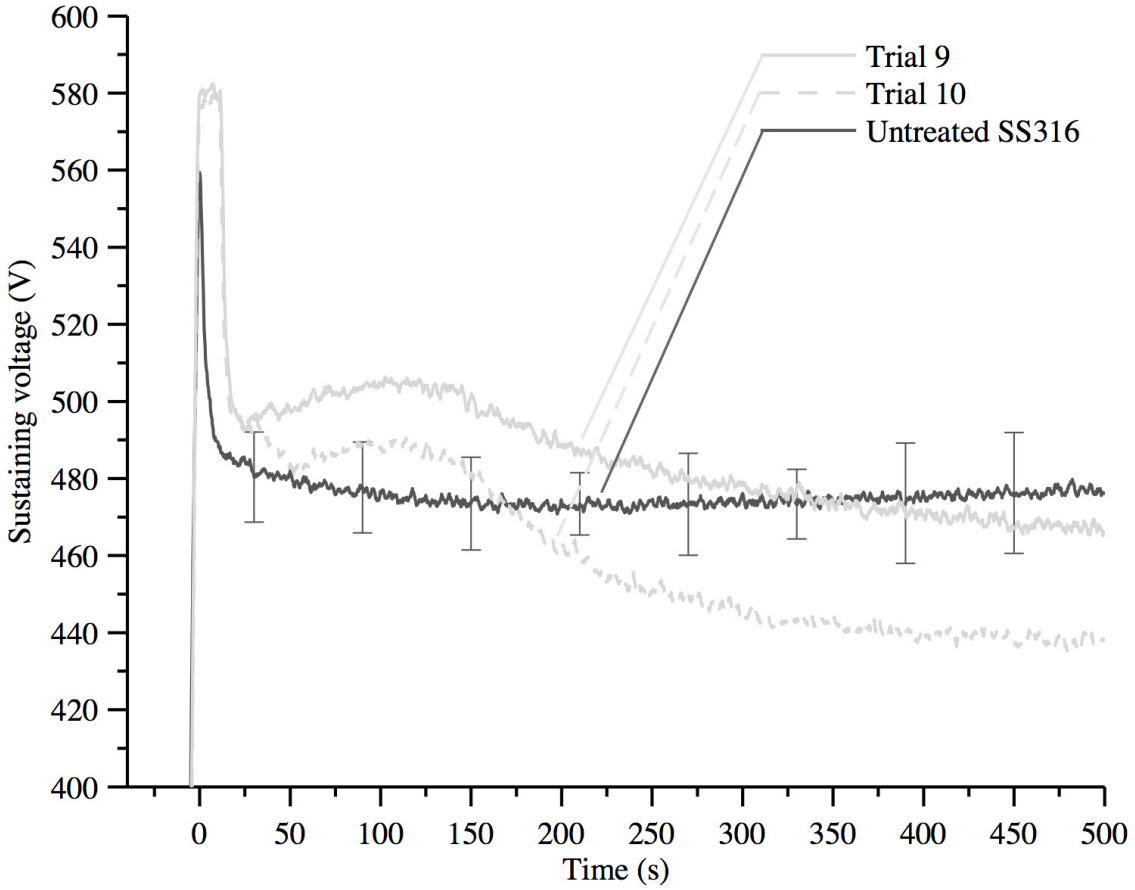


Figure 6–14: A comparison of Trials 9 and 10 with the untreated SS316 control as an example of the possibly confounding effect of the measured sample variance.

Given the obfuscating effect of the variances as discussed above, it was of interest to isolate and adjust their source(s) in the composite synthesis procedure in order to mitigate their effects on the statistical comparison of the measured sustaining voltages. As discussed in Section 6.3, the rate of nanoparticle deposition appeared to introduce significant variation in the composite synthesis, and investigations into this are detailed in the following Chapter. Presented below are the results of an investigation into the evaporation rate of Zn as a source of variance in the composite synthesis procedure.

### 6.4.3 Zinc nanoparticle production rate

Shown in Figure 6–15 are the evaporation rates measured from the mass change of the Zn-containing crucible as a function of the evaporation source setpoint temperature. In order to obtain measurable mass changes, all measurements were taken after at least 15 min of evaporation with an average evaporation time of 43 min, using argon as the carrier gas with the operating conditions of $Q_N = 0.84$ SLPM, $Q_S = 0.90$ SLPM, $Q_{PP} = 0.324$ SLPM, and $P_R = 1.8$ Torr. At evaporation temperatures of $T = 575\,^{\circ}C$ and above, the measured evaporation rates were statistically identical at 95% confidence. Further examination of the data revealed a decreasing trend in the evaporation rate with respect to increasing values of the initial mass of the zinc and crucible, shown in Figure 6–16. This suggested a heat transfer limitation in the process resulting from the construction of the evaporation source and the mode of heat transfer.

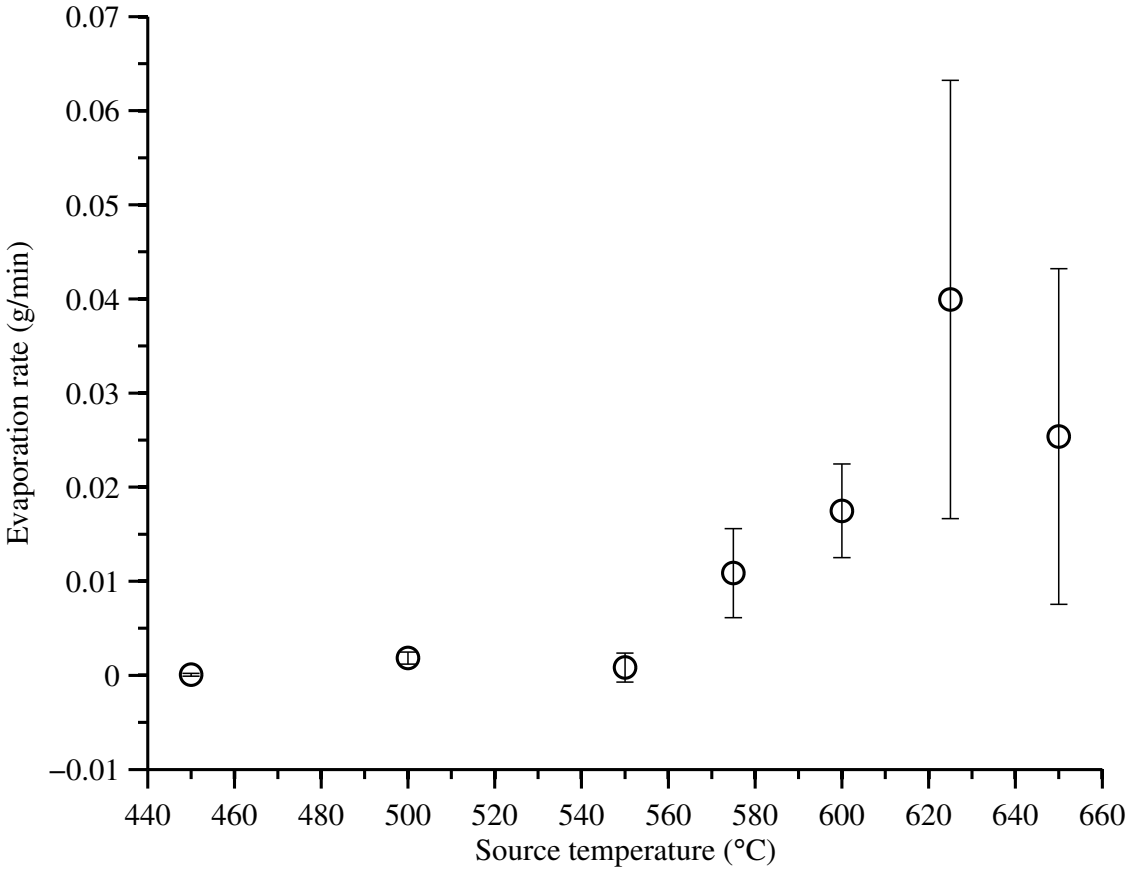


Figure 6–15: Measured zinc evaporation rate as a function of the evaporation source setpoint temperature. Error bars indicate 95% confidence intervals about the mean values for the set of $n = \{3, 7, 4, 3, 24, 3, 10\}$ at $T = \{450, 500, 550, 575, 600, 625, 650\}$ °C, respectively.

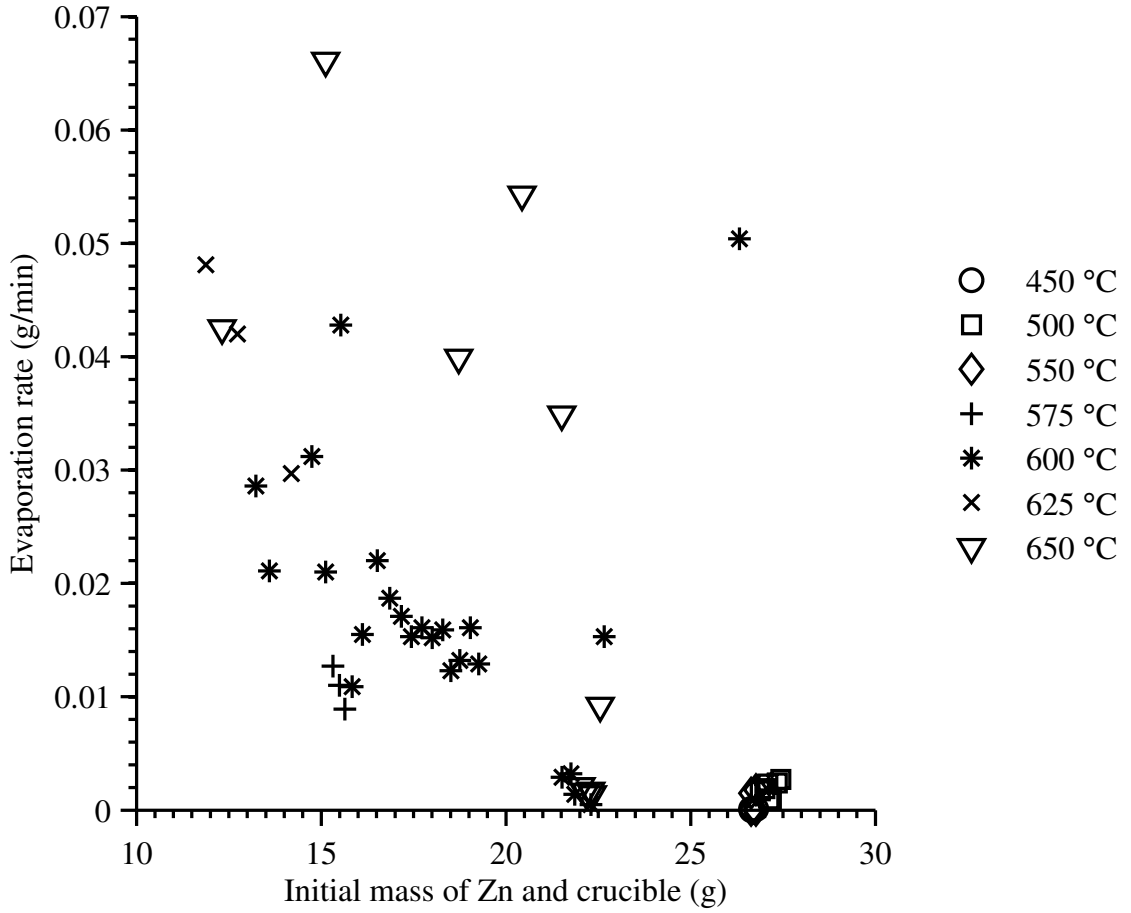


Figure 6–16: A comparison of the gravimetrically measured evaporation rates of Zn from the evaporation source for various crucible loadings and evaporation source setpoint temperatures.

In the evaporation source, heat is supplied to the bottom of the crucible by a double-layer coil of a 30 cm length of tungsten filament with a diameter of 0.6 mm. This is located 3.1 mm from the bottom of the crucible, with a Type C thermocouple placed approximately 2 mm below the bottom layer of the tungsten coil. Since the dominant heating mode of the crucible in the evaporation source is normally

by radiation under UHV, the use of elevated pressures in the deposition apparatus described in this work would have reduced the heat flux to the bottom of the crucible by heat lost to heating the gas present in the system. This is demonstrated in Figure 6–17, where the temperature of the tungsten filament was calculated from its resistivity [166] and measurements of the voltage and current supplied by the evaporation source's power supply at a pressure of 2.0 Torr. The approximately 400 °C difference in the measured and filament temperatures can be attributed to convective heat losses if we assume the heat transfer between the filament and thermocouple is comparable to that between the filament and crucible. Thus, with heat losses by convection and the presence of a flowing gas over the semi-molten surface of the zinc pellets, it is likely that a large temperature gradient existed between the bottom of the crucible and the zinc surface. Moreover, the geometry of the nozzle and the expansion of the quenching gas into the vacuum and over the surface of the evaporation source likely caused eddies which may have contributed to the variable evaporation rates observed in Figures 6–15 and 6–16. Since the causes attributed to the observed variable evaporation rates were fixed by the reactor design, a quantification of the deposition rates was undertaken and this is described in the following Chapter.

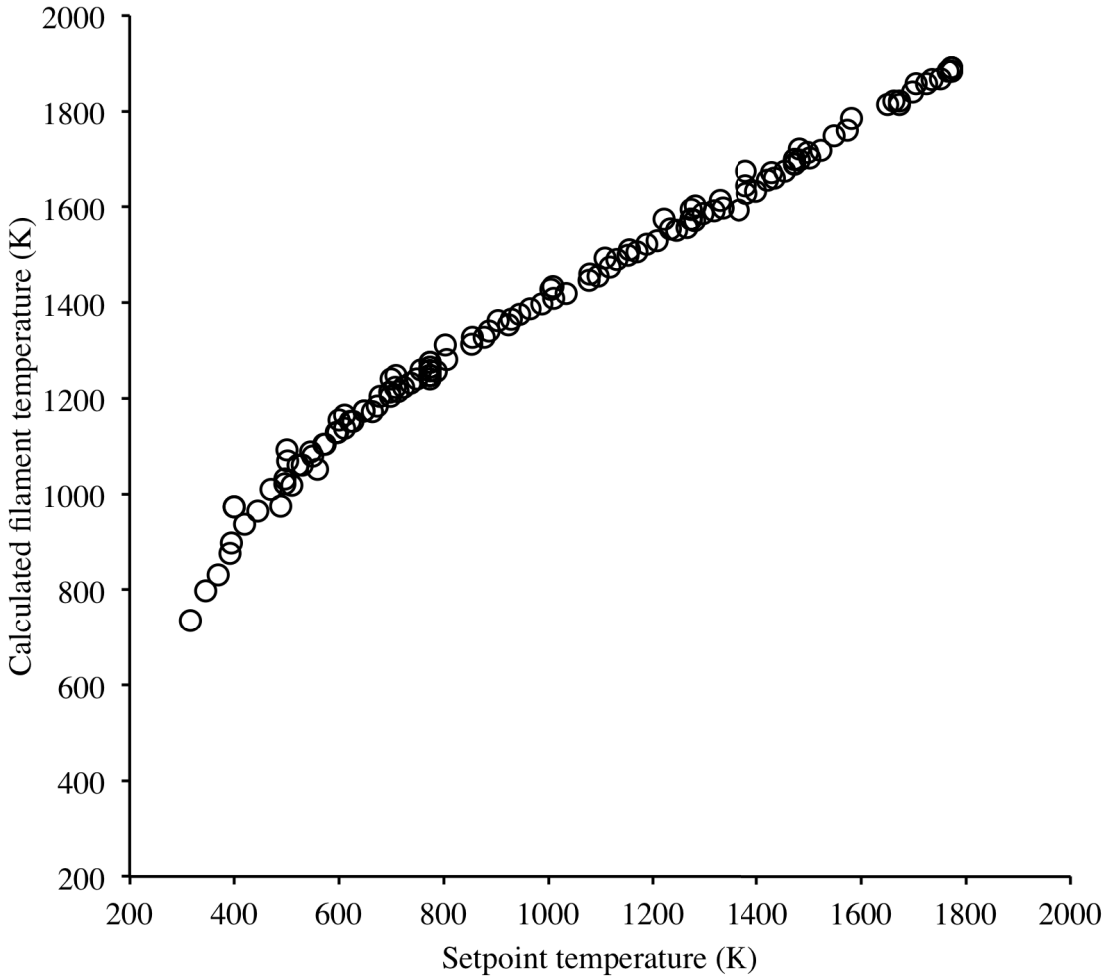


Figure 6–17: Calculations of the filament temperature in the evaporation source from measurements of the supplied voltage and current, as compared to the setpoint temperature, indicating a heat transfer limitation.

## 6.5 Summary

Experimentation in synthesizing Zn/ZnO-CNT nanocomposites using the constructed deposition apparatus revealed that CNT substrates could be rapidly coated

with nanoparticles from an evaporative source. However, examination of the synthesized nanocomposite materials using electron microscopy revealed large variation in the extent to which samples were coated with nanoparticles.

The evaluation of the synthesized Zn/ZnO-CNT composites as cathode materials used to sustain a DC glow discharge in $N_2$ revealed no significant reduction in the sustaining voltages required when these samples were compared to controls of CNT-SS316 and untreated SS316 substrates. This was attributed to the observed degradation of the composite materials resulting from erosion by ion bombardment at the cathode surface and a significant increase in the variance of the voltage measurements for treated samples. Examination of the evaporation rate as an explanation for this increased variance revealed large variance at elevated temperatures which, between 575 °C and 650 °C, were statistically equivalent.

# CHAPTER 7
# Characterization of nanoparticle deposition rates and composition

## 7.1 Introduction

For the developed metal nanoparticle synthesis and deposition technique to be viable as a deposition process for synthesizing nanoparticle coatings, then control of the process, regardless of the substrate, is imperative. The apparatus constructed to synthesize these coatings posed a number of challenges resulting from variability in the metal evaporation rate of the nanoparticle evaporation-condensation process. This translated to limitations in the temperature and gas flow rates that could be used in the process to obtain the nanoparticle coatings desired.

Given the clear need for future design iterations to reduce the process variance, the establishment of a baseline for future process improvements was necessary. Consequently, presented in this Chapter is an investigation of the thicknesses of nanoparticle layers deposited on silicon wafers and their correlation with the measured evaporation rates in the system. Following this, the effect of the RF glow discharge on the surface composition of the nanoparticle films is evaluated using XPS, and the bulk composition is evaluated using XRD.

## 7.2 Nanoparticle coating thickness measurements

### 7.2.1 Experimental procedures

#### 7.2.1.1 Masked substrate preparation

In order to generate nanoparticle coatings for surface analysis using atomic force microscopy (AFM), flat, 5 mm × 5 mm silicon chip specimen supports (Part: 16008, Ted Pella, USA) were used as substrates. A masking technique using freshly-cleaved mica was used to generate sharp discontinuities between the silicon substrate and the deposited nanoparticle coatings in order to measure the thicknesses of the nanoparticle layers.

Masked silicon wafer substrates for thickness measurements were prepared for deposition by first ultrasonically cleaning the wafers for 5 min in a 150 mL Pyrex® beaker containing methanol, and left to dry at room temperature for approximately 30 min. Freshly-cleaved mica (Part: 52-6, Ted Pella, USA) was used as a masking material. A short length of approximately 5 mm-wide mica was cut from the larger sheet, and cleaved using adhesive tape. This thin layer was then applied to the silicon wafer and trimmed using scissors to cover approximately half of the wafer's surface area. No adhesives were required as the mica layer was held in place by electrostatic forces. Following nanoparticle deposition on the wafer, the mica mask was lifted at one corner using tweezers and removed. This resulted in a clearly defined discontinuity in the deposited nanoparticle layer that could be measured using AFM.

#### 7.2.1.2 Atomic force microscopy measurements

AFM measurements were performed using a Veeco MultiMode V in semi-contact mode. For each sample generated, the thickness of the nanoparticle layer was measured at three random locations along the discontinuity. All scans of the discontinuity were made for a 1 µm × 1 µm area at a resolution of 128 lines/µm, except as noted. Exceptions to this were either caused by particularly thick nanoparticle coatings, or by defects in the uniformity of the nanoparticle layer resulting from ambient particle contamination. In the former case, the scan speed was reduced and the resolution increased in order to ensure the AFM probe was able to track sudden changes in height. In the latter case, the scan area was reduced in order to avoid disruptions to the scan caused by the defect or contaminant.

#### 7.2.1.3 Experimental conditions

The evaporation source temperatures corresponding to the samples synthesized for step height measurements are listed in Table 7–1. In all trials, argon was used as the carrier and RF glow discharge gas. The deposition reactor conditions used were: $t_d = 1.5$ min $Q_N = 0.84$ SLPM $Q_S = 0.90$ SLPM $Q_T = 2.06$ SLPM $P_R = 2.0$ Torr. The surface area of the RF electrode is $39.4\,\mathrm{cm}^2$, which at the applied RF power of 20 W gave a power density of $0.5\,\mathrm{W\,m^{-2}}$.

Table 7–1: Evaporation source temperatures corresponding to the synthesized samples.

| Trial | T<br>°C |
|---|---|
| 2, 3, 4 | 575 |
| 1, 5, 6 | 600 |
| 7, 8, 9 | 625 |

### 7.2.2 Results and discussion

Nanoparticle coatings with distinct discontinuities were synthesized and examined using SEM prior to AFM analysis. Examples of the generated discontinuities in the nanoparticle layers are shown in Figure 7–1 and in Figure 7–2 for SEM and AFM, respectively.

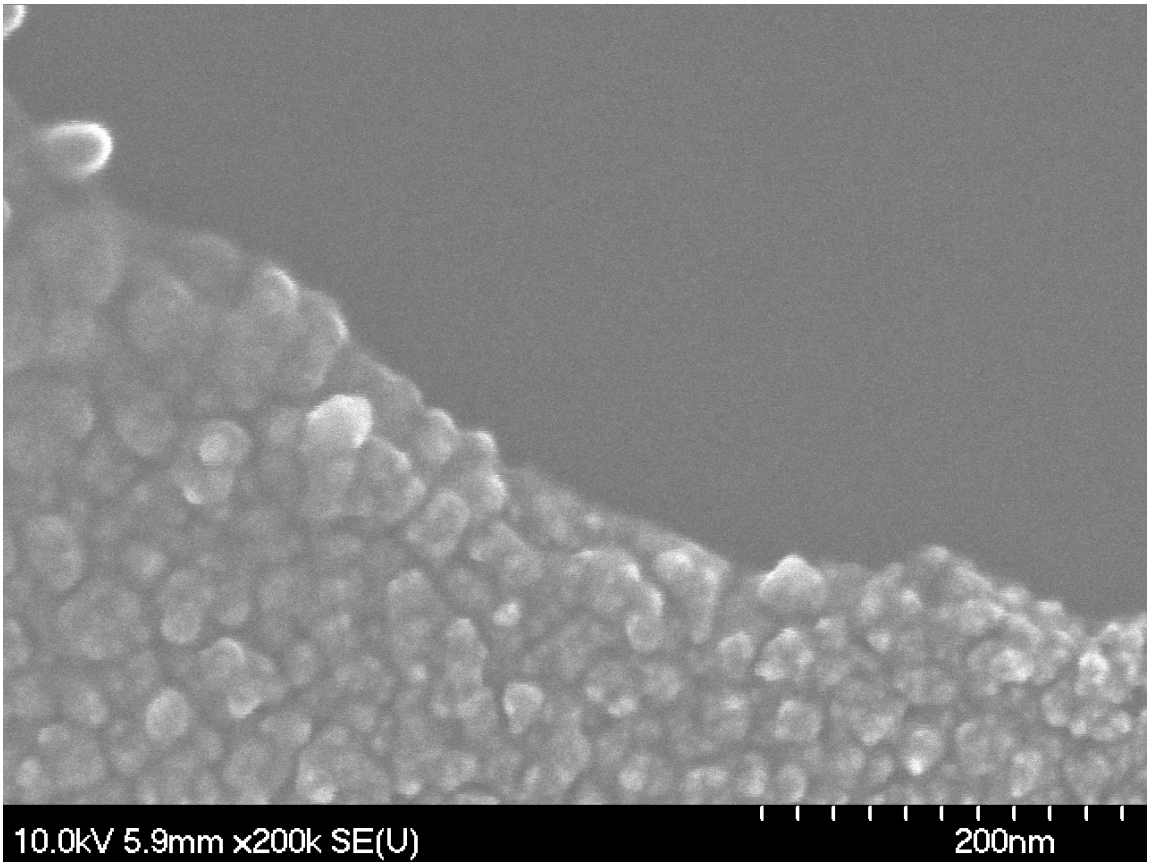


Figure 7–1: SEM image of a discontinuity in the nanoparticle layer deposited on a Si wafer, produced using the described masking technique.

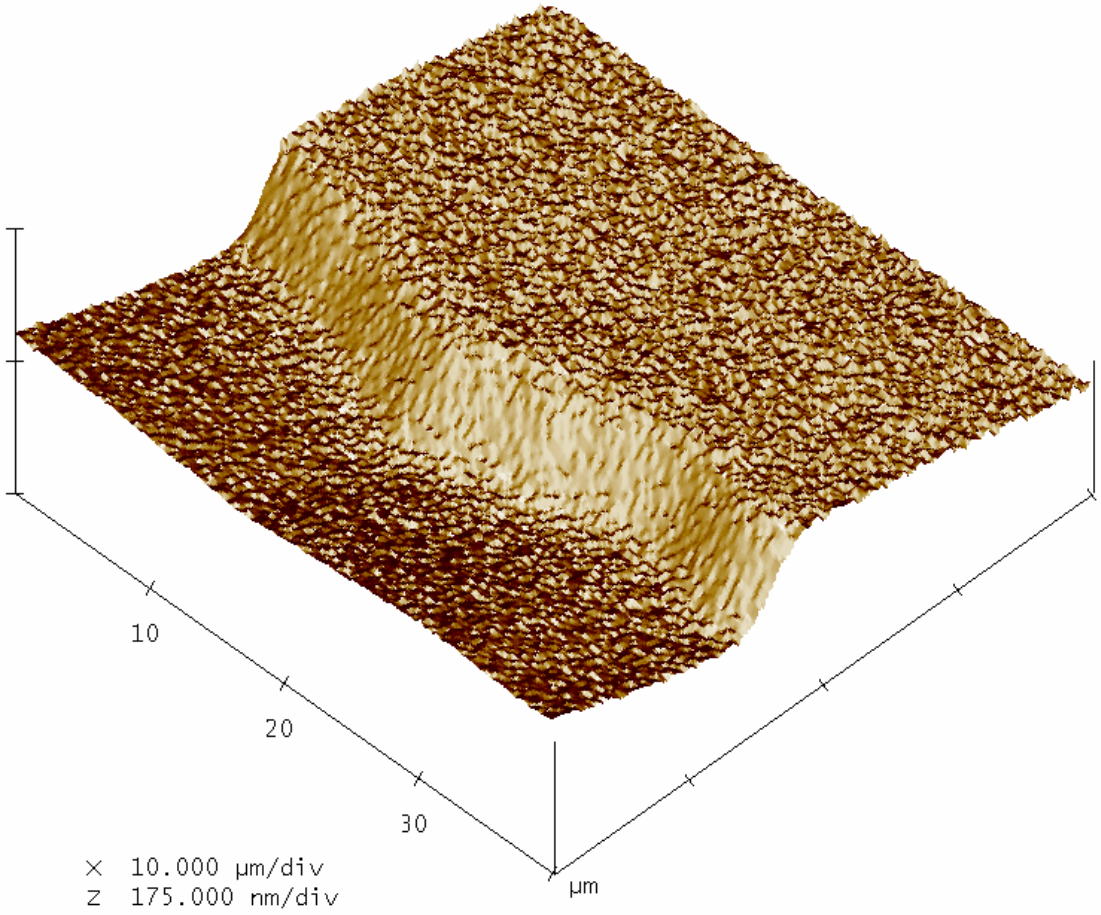


Figure 7–2: An example of the step heights generated using mica masks and measured using AFM. Shown is a film thickness of $109.5 \pm 0.9$ nm (95% confidence interval for $n = 128$ scan lines across the measured area shown).

As shown in Figure 7–3, the surface of the nanoparticle layers appeared to be quite granular and porous with many topographical features at the nm-scale. The

deposited nanoparticle layers were also susceptible to mechanical damage; shown in Figure 7–4 is the effect of the brief physical contact between the sample and plastic tweezer tips used in positioning the sample of the AFM mount. Practically, the porosity and fragility of the films had little effect on the $1\,\mu m \times 1\,\mu m$ scans used for film thickness measurements, however they posed significant challenges in obtaining high-resolution AFM scans of the sample surfaces, as the AFM probe had difficulty resolving sudden height changes resulting from the porosity of the film. Moreover, contamination of the probe was frequently an issue at high resolution. This was most likely caused by nanoparticles dislodged from the film as a result of the increased frequency of interaction between individual nanoparticles and the AFM probe at high resolution in semi-contact mode.

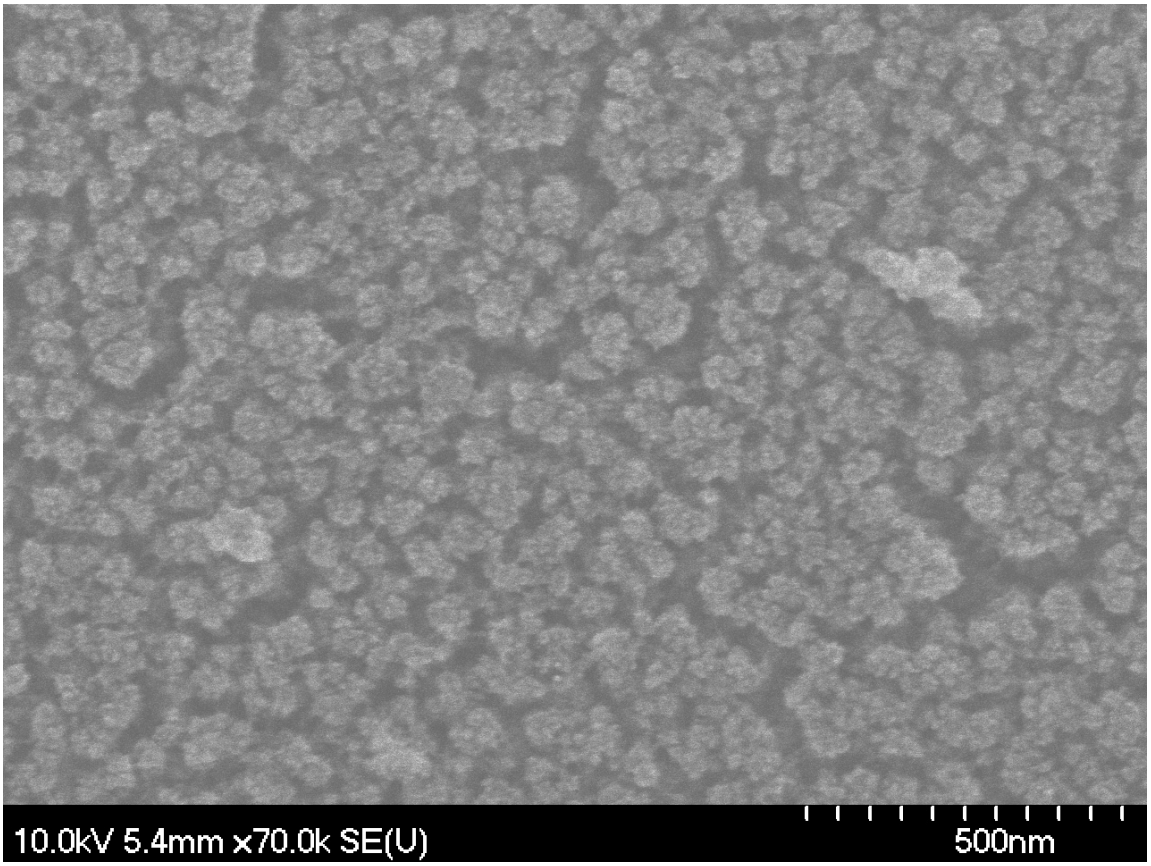


Figure 7–3: SEM image of the porous, granular structure of the deposited nanoparticle layers.

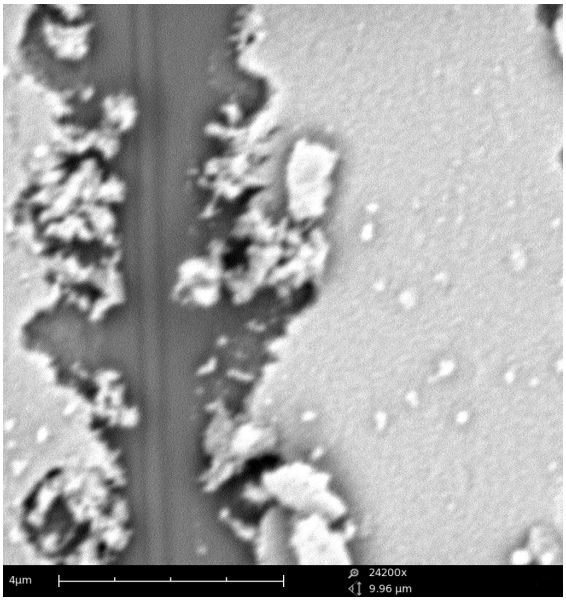


Figure 7–4: Damage to the deposited nanoparticle layer caused during sample mounting in the AFM.

The film thickness measurements of all trials are shown in Figure 7–5. Excepting the last two measurements of Trial 5, all measurements were significantly different at 95% confidence, indicating that the films of nanoparticles varied in height over the surface of the substrate. Certainly this can be attributed to the previously-measured variance of the zinc evaporation rate, yet another likely effect is that of the reactor pressure of 2.0 Torr. As reviewed in Chapter 2, the increased system pressures of AFC reduces the mean free path of evaporated atoms/molecules, thus favouring the nucleation and condensation of nanoparticles near the source of evaporated material and transporting these nanoparticles downstream in the process. As a consequence, the deposition of nanoparticles from the carrier gas is a function of the flow field of the gas around the substrate. This was observed qualitatively in the visible diffraction

pattern of the nanoparticle films deposited on the silicon wafers, an example of which is shown in Figure 7–6. In all samples, these diffraction patterns appeared to be uniform near the masked edge, but changed markedly near the edges of the 460–530 µm thick Si wafers.

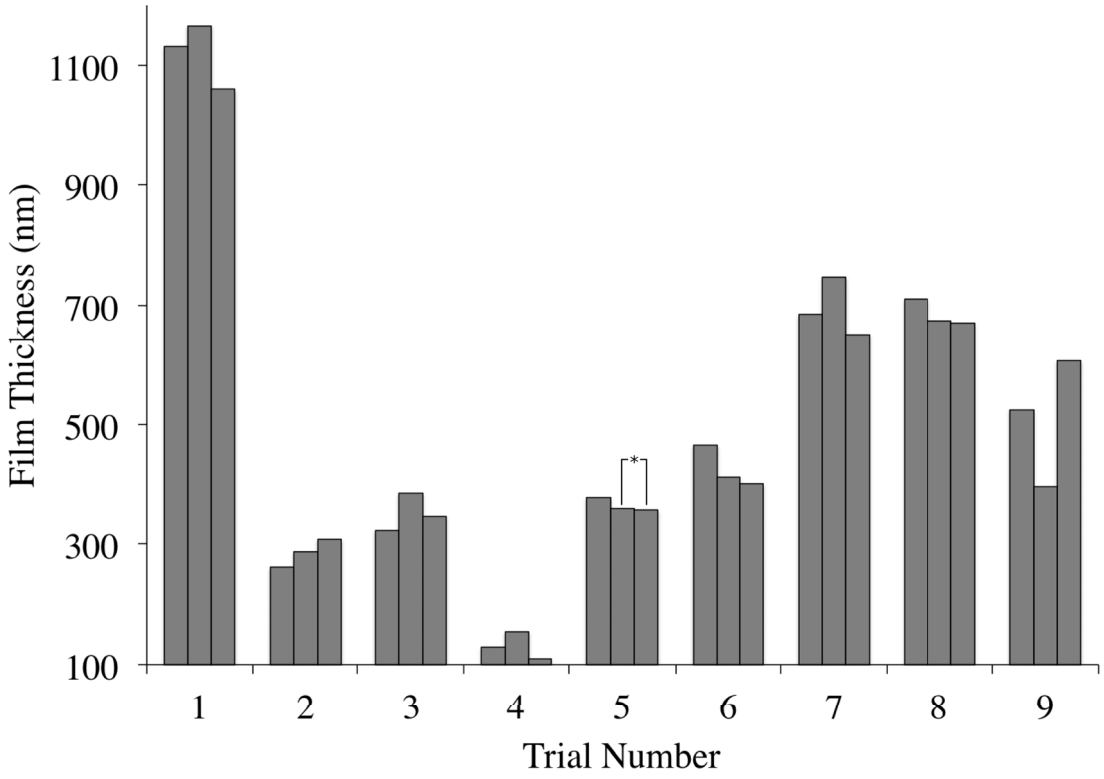


Figure 7–5: Triplicate film thickness measurements of the samples synthesized in Table 7–1. $n = 128$ for for all measurements excepting the first and second measurements of Trial 1 ($n = 358$ and $n = 462$, respectively), and the first measurement of Trial 2 ($n = 65$). 95% confidence intervals on individual measurements are on the order of $\approx 1$ nm and thus are below the resolution of the Figure. Statistically equivalent measurements at 95% confidence are indicated by *.

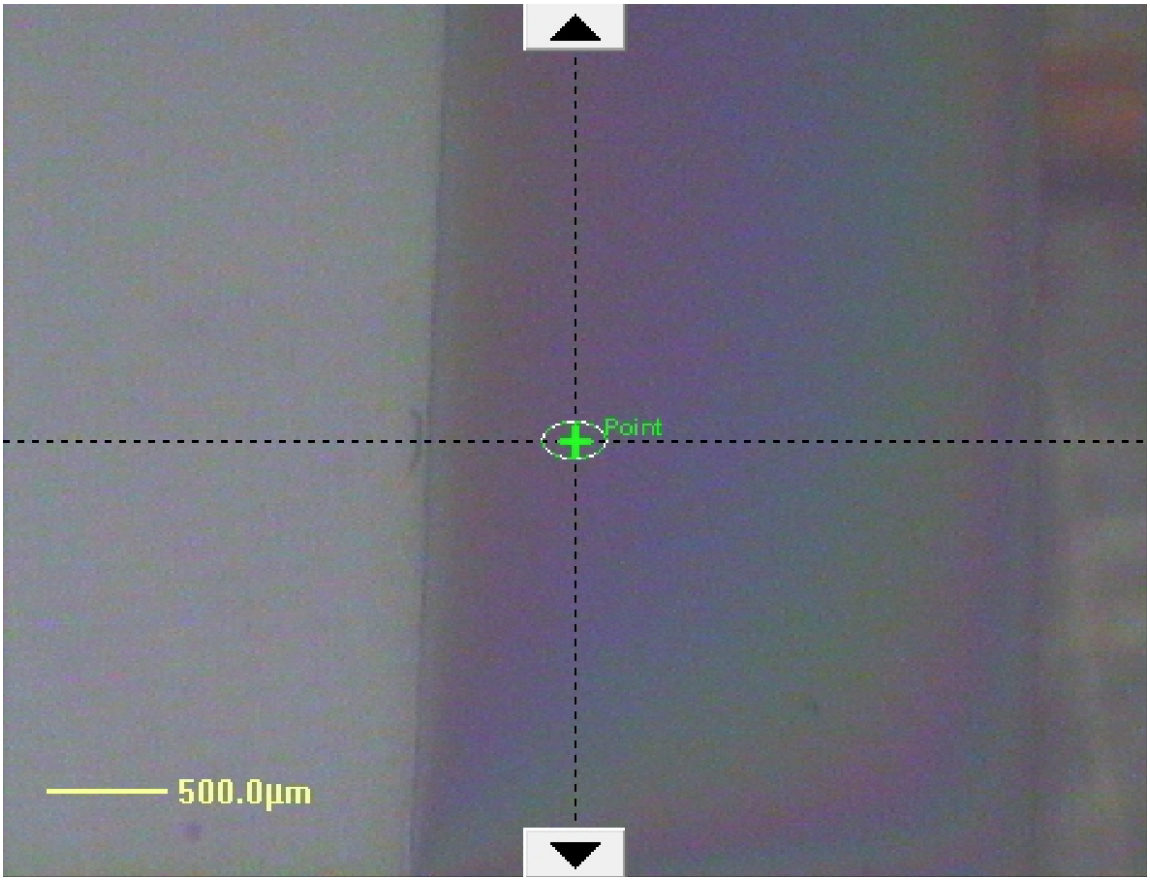


Figure 7–6: Diffraction patterns caused by variations in the thickness of the deposited nanoparticle layer on silicon wafers.

Linear regressions of the measured film thicknesses as functions of the source temperature and the measured evaporation rate, shown in Figures 7–7 and 7–8 respectively, were performed in order to assess the extent to which the evaporation temperature could control the rate of nanoparticle deposition, and to evaluate the contribution of the variability observed in the evaporation rate to that observed in the deposition rate of nanoparticles on the silicon wafers. The regressions presented in Figures 7–7 and 7–8 are for the data from Trials 2–9. Initial regressions of the

entire data set revealed no influential points as possible outliers using the criterion of Cook's distances greater than unity, yet those for Trial 1, ranging from 0.1045 to 0.2479, were generally an order of magnitude larger than those of the other data points. Moreover, in both regressions of the full data set, normal probability plots of the residuals revealed strongly non-normal distributions resulting from the residuals of Trial 1. Removal of this data restored linearity to both normal probability plots, and further plots of the residuals against the predicted values of the film thicknesses, or of the residuals as functions of the source temperature and evaporation rate revealed no trends remaining in the data. Thus, in the following analysis, the results of Trial 1 were not considered.

The regression of Figure 7–7 resulted in:

$$\text{Deposited Film Thickness} = 7.48T - 4060 \tag{7.1}$$

where the Deposited Film Thickness is measured in nm and $T$ is the setpoint temperature of the evaporation source in °C. For this regression, $R^2 = 0.766$ and the 95% confidence interval on the slope is [5.66..9.31]. While this analysis indicates the regression is technically valid, from a practical standpoint the primary issue is the large 95% confidence interval on the value of a future predicted response. Effectively, any attempt to control the deposited film thickness using the given experimental conditions is 95% likely to have a margin of error of approximately $\pm 225$ nm. Thus, while rapid deposition of nanoparticles is possible, control of the rate of deposition using temperature would require further development.

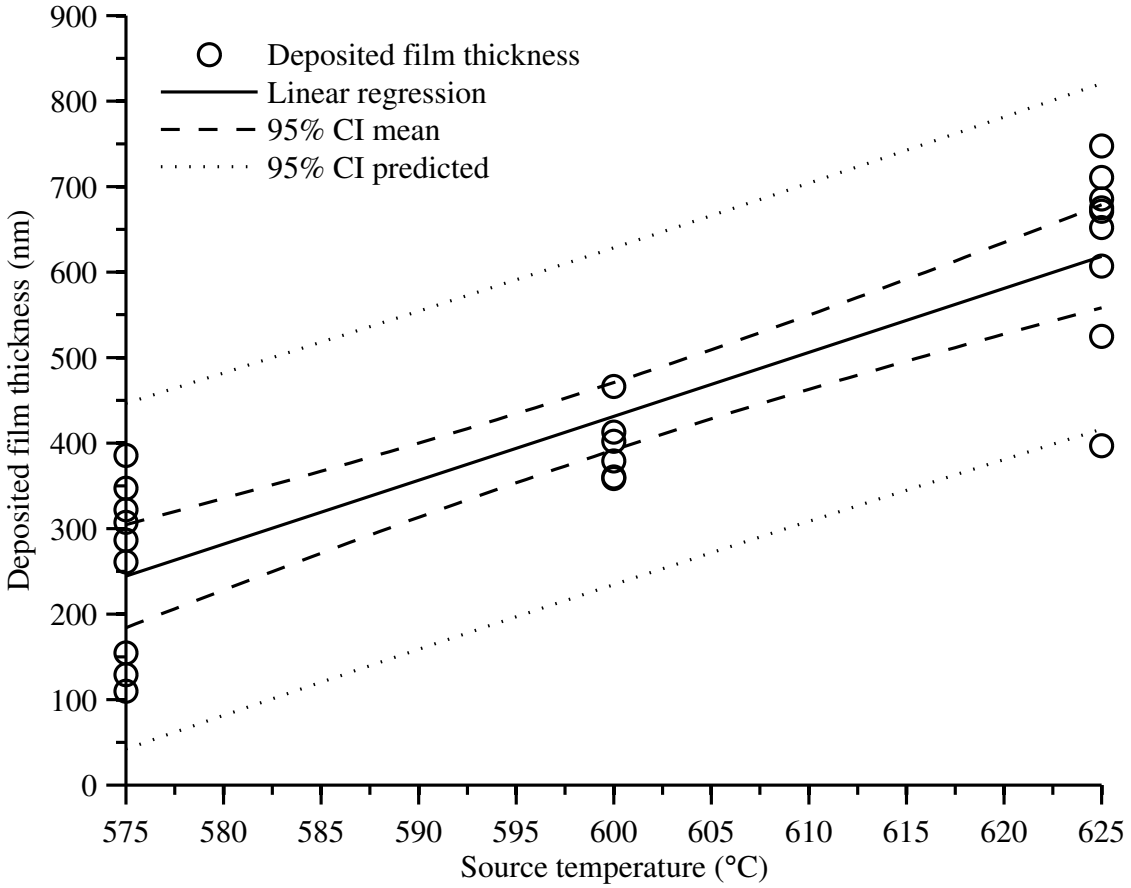


Figure 7–7: Linear regression of the measured nanoparticle film thicknesses for Trials 2–9 as a function of the evaporation source temperature. Confidence intervals on the mean response of the model and on the prediction of a future measurement are given at 95%.

Examining the regression of Figure 7–8 requires a slightly different analysis, as both the measured evaporation rate at the source and the deposited film thickness are random variables. The correlation coefficient between the evaporation rate and film thickness was 0.728 thus, unsurprisingly, the two variables are positively correlated. The regression equation was determined to be:

$$\text{Deposited Film Thickness} = 9830(\text{Evaporation Rate at Source}) + 180 \qquad (7.2)$$

where the Evaporation Rate at Source is measured in g/min. For this regression, $R^2 = 0.529$ and the 95% confidence interval on the slope is [5730..13900]. Assuming $n = 24$ is a sufficiently large number of samples to infer the distribution of the correlation coefficient from the experimental data, a 95% confidence interval for the correlation coefficient can be estimated as [0.459..0.874] [165]. From this it can be inferred that although approximately 53% of the variation in the film thickness can be attributed to the evaporation rate at the source, the strength of the positive linear relationship between the evaporation rate and the deposited film thickness (i.e. the 95% confidence interval on the correlation coefficient) is wide, and other process variables are most likely contributing to the variability in the deposited film thickness.

Similar to the analysis of Figure 7–7, a 95% confidence interval on the predicted value of a future response was constructed by treating the measured evaporation rate as an independent variable, and this is shown in Figure 7–8. The resultant margin of error is approximately $\pm 550$ nm which, when considered with the margin of error from Figure 7–7, provides an important piece of evidence regarding the variability observed during the course of this project in the coating thicknesses of the synthesized Zn/ZnO-CNT nanocomposites and in the variability of the measured sustaining voltages when these nanocomposites were used as DC glow discharge cathodes. It is extremely likely that the difficulties in obtaining reproducible data in this project, as described in Chapters 5 and 6, can be attributed to the inability of the constructed system to deposit nanoparticle coatings with a precision less than

the calculated margins of error of approximately ±225 nm and ±550 nm when the source temperature or the evaporation rate at the source are known, respectively. As a result, further development of the AFC reactor design is needed to obtain better control of the nanoparticle deposition rates before this technique can be applied to reliably produce CNT nanocomposite materials with reproducible nanoparticle coating thicknesses.

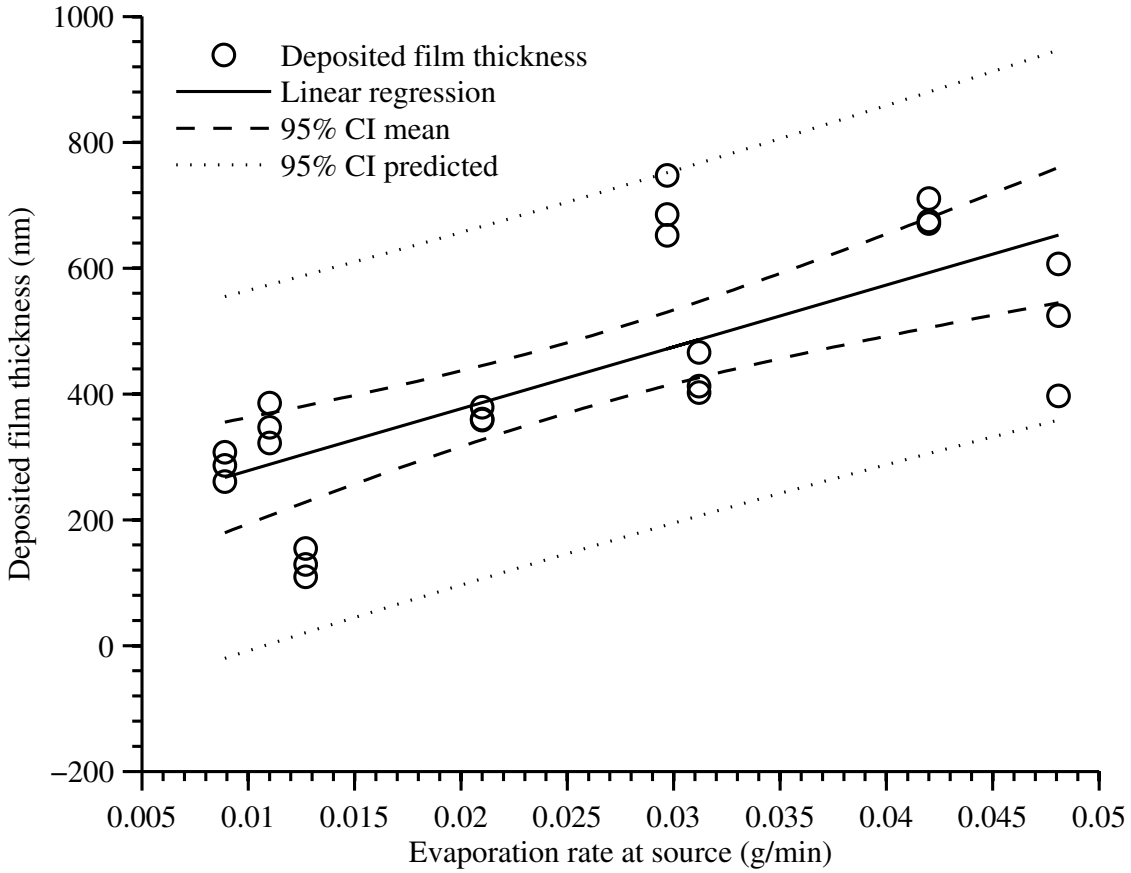


Figure 7–8: Linear regression of the deposited film thickness for Trials 2 to 9 as a function of the zinc evaporation rate measured at the high-temperature source. Confidence intervals on the mean response of the model and on the prediction of a future measurement are given at 95%.

## 7.3 XPS analysis of deposited Zn/ZnO nanoparticle layers

Given the morphological differences of the deposited nanoparticles on CNTs, as described in Chapter 5, the generation of nanoparticles versus microparticles in the presence/absence of the RF glow discharge in the deposition apparatus, and the mixed Zn and ZnO signals from the electron diffraction patterns of Chapter 5, an investigation of the surface and bulk compositions of the synthesized materials was undertaken. Films of Zn/ZnO nanoparticles were deposited on Si wafers using experimental conditions similar to those for nanocomposite synthesis. This was done in order to obtain samples that were analogous to the synthesized nanocomposites, but were comparatively "flat," so that they could be analyzed via X-ray photoelectron spectroscopy (XPS) and X-ray diffraction (XRD).

### 7.3.1 Experimental procedures

#### 7.3.1.1 XPS

XPS was performed using a Thermo Scientific K-Alpha spectrometer which utilized a monochromated aluminum X-ray source (Al K$\alpha$ at 1486.6 eV). All spectra were collected at an analysis chamber pressure of less than $10^{-8}$ Torr. For peak identification, all spectra were normalized to the C1s peak at 285.0 eV. Atomic composition depth profiles were generated by argon ion sputtering at an accelerating voltage of 3000 eV and 10 nA, where the sputtering time for each sample was determined by a series of rapid trial-and-error survey scans prior to the collection of high resolution scans for Zn, O, C, and Si.

#### 7.3.1.2 XRD

XRD data was collected using a Bruker D8 Discover equipped with a general area detector diffraction system (GADDS). Low incident X-ray angles (1°–3°) were used as a result of the flat samples, thus $2\theta$ scans were limited to between approximately 10°–105°.

#### 7.3.1.3 Nanoparticle layer synthesis

The analysis of the following samples is described below. All samples shared the following synthesis conditions. Argon was used as the nozzle and sheath gas, and was supplied at flow rates of $Q_N = 0.84$ SLPM and $Q_S = 0.90$ SLPM. The reactor pressure was maintained at $P_R = 2.0$ Torr and the total gas flow rate through the system was $Q_T = 2.06$ SLPM.

1. Sample 1 was generated without the RF glow discharge in order to deposit microparticles on the Si wafer. Argon was supplied at a flow rate of $Q_{PP} = 0.324$ SLPM in order to maintain the system pressure and total flow rate, as above. The deposition time for the synthesis of the microparticle layer was $t_d = 5$ min.
2. Sample 2 was generated in the presence of an Ar RF glow discharge at 20 W in order to deposit nanoparticles on the Si wafer. Argon was supplied at a flow rate of $Q_{PP} = 0.324$ SLPM in order to maintain the system pressure and total flow rate, as above. The deposition time for the synthesis of the nanoparticle layer was $t_d = 1.5$ min.
3. Sample 3 was generated in the presence of an Ar RF glow discharge at 20 W containing 16%vol. $O_2$. This corresponded to an $O_2$ flow rate of $Q_{PP} = 0.324$ SLPM. The deposition time for the synthesis of the nanoparticle layer was

$t_d$ = 1.5 min. In order to evaluate the effectiveness of the oxygen plasma in generating ZnO nanoparticles, a plasma polymer layer was deposited on the Si wafer following the nanoparticle deposition to inhibit the diffusion of oxygen to the as-synthesized nanoparticles once the sample was removed from vacuum [167]. All gas flow rates were shut off, and 10 sccm of ethane was introduced to the reactor. A RF glow discharge at 20 W was ignited and the sample was re-introduced to the process stream using the linear motion for 2.5 min to deposit the plasma polymer. During this time, the reactor pressure was $P_R$ = 2.0 Torr.

### 7.3.2 Results and discussion: XPS of nanoparticle layers on Si wafers

Similar to the results of Chapter 5, the absence of a RF glow discharge to prevent nanoparticle agglomeration similarly resulted in the formation of microparticle films on the silicon wafer substrates, as shown in Figure 7–9. The deposited film appeared to have a structure characteristic of dendritic growth.

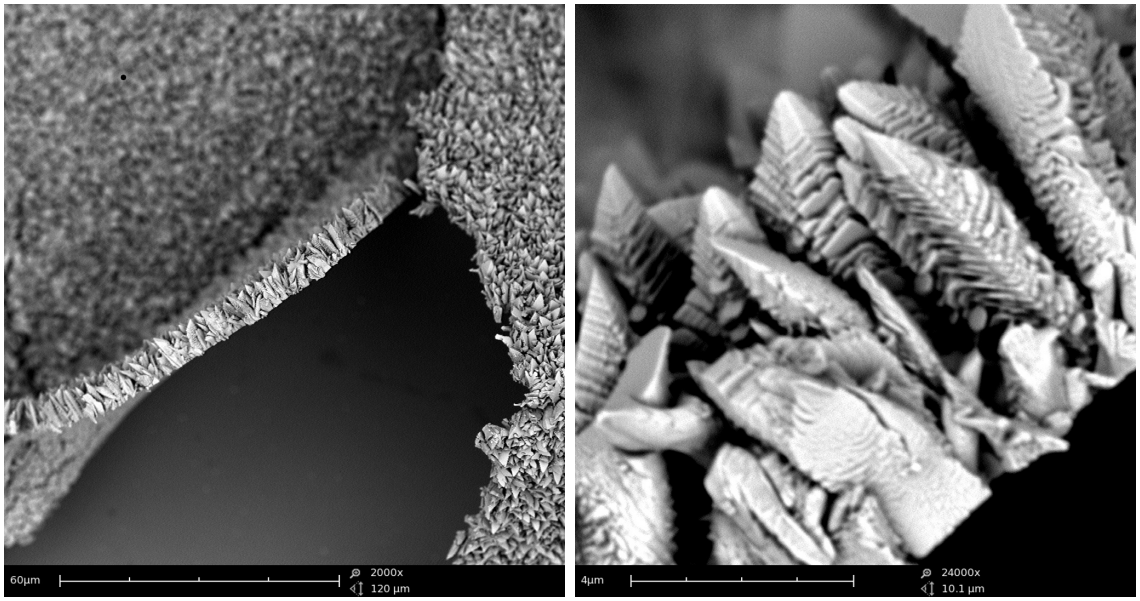


Figure 7–9: SEM images of the microparticle layers deposited on the Si wafer substrates when no RF glow discharge was present in the nanoparticle deposition system.

Figure 7–10 shows the atomic composition of the microparticle film as a function of the $Ar^+$ sputtering time (i.e. the depth profile). The decrease in the C1s signal from over 70%at. to approximately 40%at. in the first 10 s of sputtering is difficult to explain. Such a high carbon content normally indicates a carbon contamination of the surface beyond that of adventitious carbon, which is plausible since the carbon content remained above 20%at. until 100 s of sputtering, at which point the C1s signal reached zero. Normally, adventitious carbon should be removed within the first 10 to 20 s of sputtering for the accelerating voltage and beam current used. If this is the case, then the source of the contamination is unknown.

Meanwhile, the 1:1 ratio of the O1s signal to the Zn2p3 signal, indicated that $Ar^+$ was unable to remove the surface oxidation of the zinc microparticles. However, examination of Sample 1 before and after XPS analysis showed attrition of the microparticle surface (Figure 7–11), thus the incident $Ar^+$ ion energy was likely sufficient to generate depth profiles, and that further sputtering would likely remove the surface oxidation.

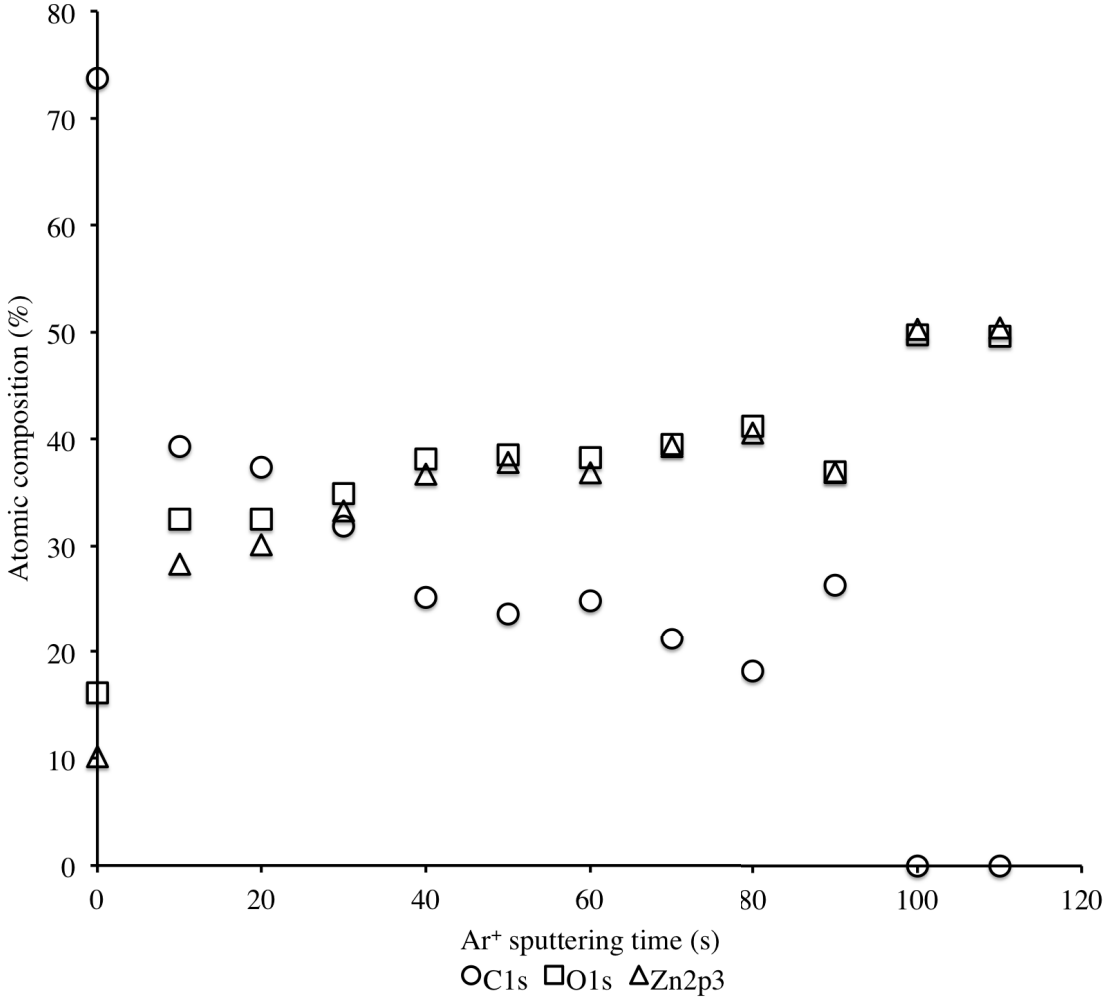


Figure 7–10: Atomic composition depth profile of Zn microparticles deposited on a Si wafer (Sample 1).

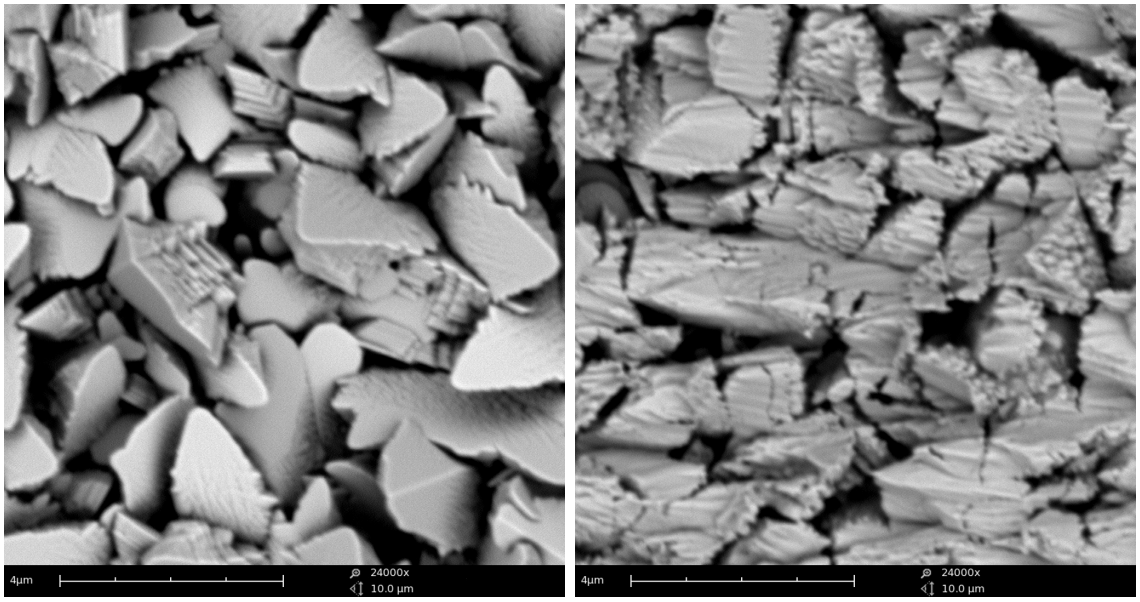


(a) Before $Ar^+$ sputtering. (b) After $Ar^+$ sputtering.

Figure 7–11: SEM images of Sample 1 before and after the generation of the XPS depth profile in Figure 7–10.

However, XPS depth profile studies of the deposited nanoparticle layers were complicated by the apparent porosity of the nanoparticle films. It appeared that the films were sufficiently porous that the unknown carbon contamination discussed above was capable of permeating the film. The XPS depth profile of Sample 2 is shown in Figure 7–12. After approximately 250 s, all carbon was removed from the sample, however this also corresponded to a removal of the nanoparticle layer. This removal of the nanoparticle layer was visually observed during data acquisition as a change in the diffraction pattern on the Si wafer, and this was confirmed by observation of the sputtered area using SEM. Consequently, no conclusions could be drawn as to the extent of Zn nanoparticle oxidation caused by ambient oxygen.

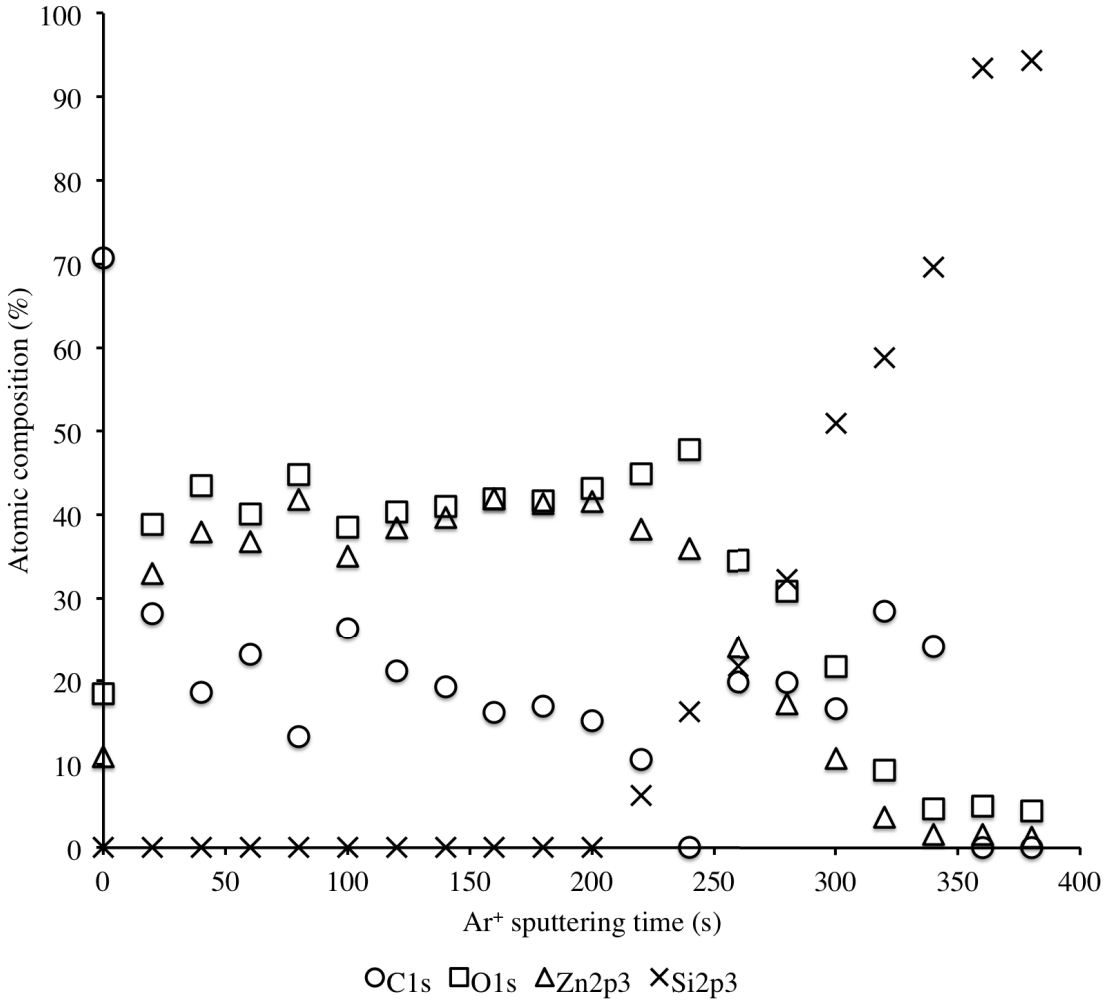


Figure 7–12: Atomic composition depth profile of Zn/ZnO nanoparticles deposited on a Si wafer (Sample 2).

The XPS depth profile of Sample 3, shown in Figure 7–13, indicated that the plasma polymer layer was rapidly removed by $Ar^+$ sputtering. After approximately 100 s, sufficient plasma polymer was removed to allow for detection of the underlying Zn/ZnO nanoparticle layer. Similar to the results of Sample 2, $Ar^+$ sputtering also

removed the nanoparticle layer from the Si wafer, again preventing any inferences as to the extent of Zn nanoparticle oxidation from process and ambient conditions.

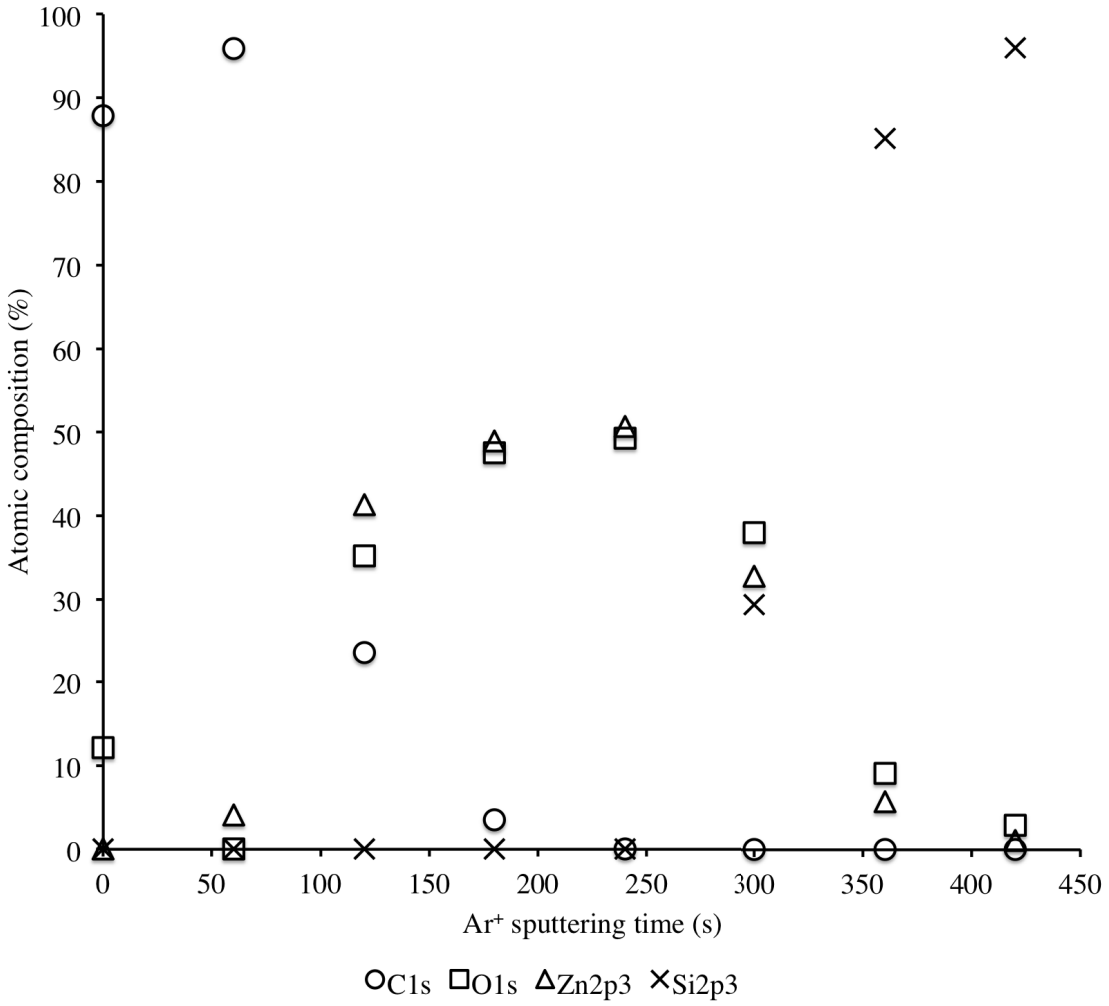


Figure 7–13: Atomic composition depth profile of Zn/ZnO nanoparticles deposited on a Si wafer and sealed with a plasma polymer layer to prevent nanoparticle oxidation by ambient oxygen (Sample 3).

### 7.3.3 Results and discussion: XRD of nanoparticle layers on Si wafers

Samples 2 and 3 were replicated and analyzed using XRD, shown in Figures 7–14 and 7–15, respectively. In both figures, the background signals were subtracted via Bezier curve. The reference patterns for Zn and ZnO are also included in Figures 7–14 and 7–15. In each Figure, the reference patterns were scaled by relative height to the peak in the scan closest to their 100% intensity lines. For Zn, this occurs at $2\theta = 43.26^\circ$ and for ZnO at $2\theta = 36.29^\circ$ [168].

In Figure 7–14, it appears the sample is predominantly composed of Zn, since the most intense peaks for Zn (i.e. at $2\theta = 39.03^\circ$, $43.26^\circ$, $54.37^\circ$, $70.15^\circ$ and $70.70^\circ$ [168]) all appear at appropriate relative intensities, as indicated by the Zn reference pattern. Conversely, the relative height of 21.94% used for the reference pattern of ZnO, combined with the fact that none of the other peaks in the scan corresponding to ZnO appear at intensities greater than those of the scaled ZnO reference pattern, provides evidence that very little ZnO was present in this sample. In Figure 7–14, the 100% intensity line for ZnO is being obscured by the XRD peak for Zn at 36.32 [168] and it is likely that any ZnO present in Sample 2 was the result of atmospheric oxidation of Zn nanoparticles synthesized in the AFC-RF process.

It appears that in Figure 7–15, both Zn and ZnO were present in the sample, and both in sufficient quantities such that their corresponding diffraction peaks appear at similar intensities. While a quantitative analysis of the amounts of Zn and ZnO present cannot be deduced from the data obtained, this result does indicate that the 16%vol. $O_2$ glow discharge had a significant effect in oxidizing the synthesized Zn nanoparticles. More oxygen is present in the sample exposed to the oxygen plasma

(Sample 3) than in Sample 2, where oxidation of the nanoparticles could only occur from exposure to ambient oxygen.

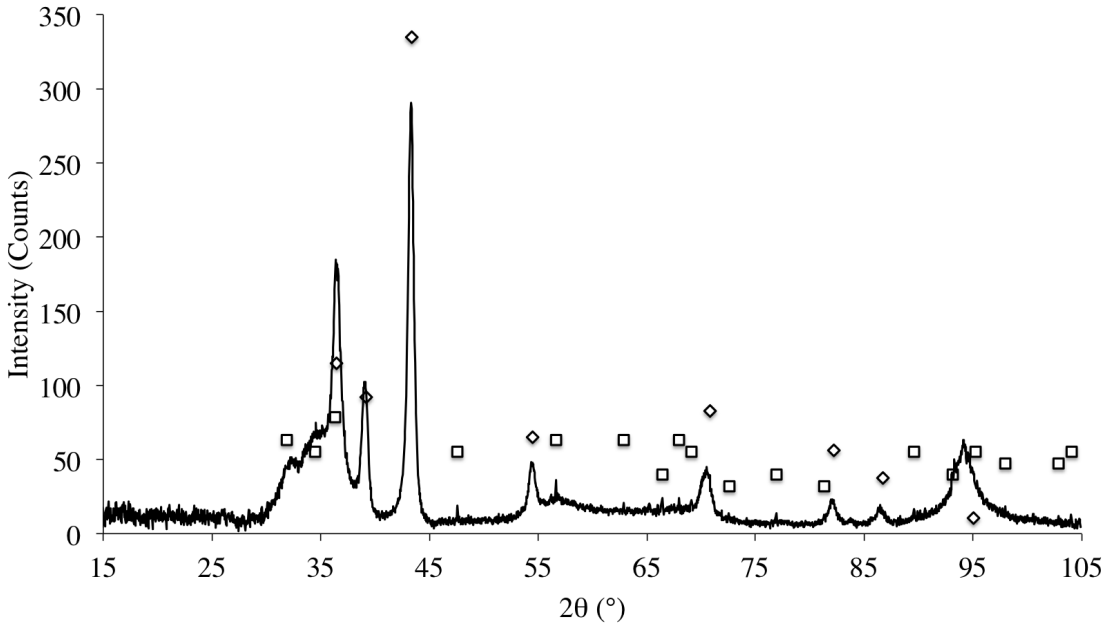


Figure 7–14: XRD spectrum of Sample 2, where no $O_2$ was present in the RF glow discharge. The reference patterns of Zn (◇) and ZnO (□) are indicated, with each scaled by relative height. For Zn, the relative height shown is 129.50% and for ZnO, the relative height shown is 21.94%.

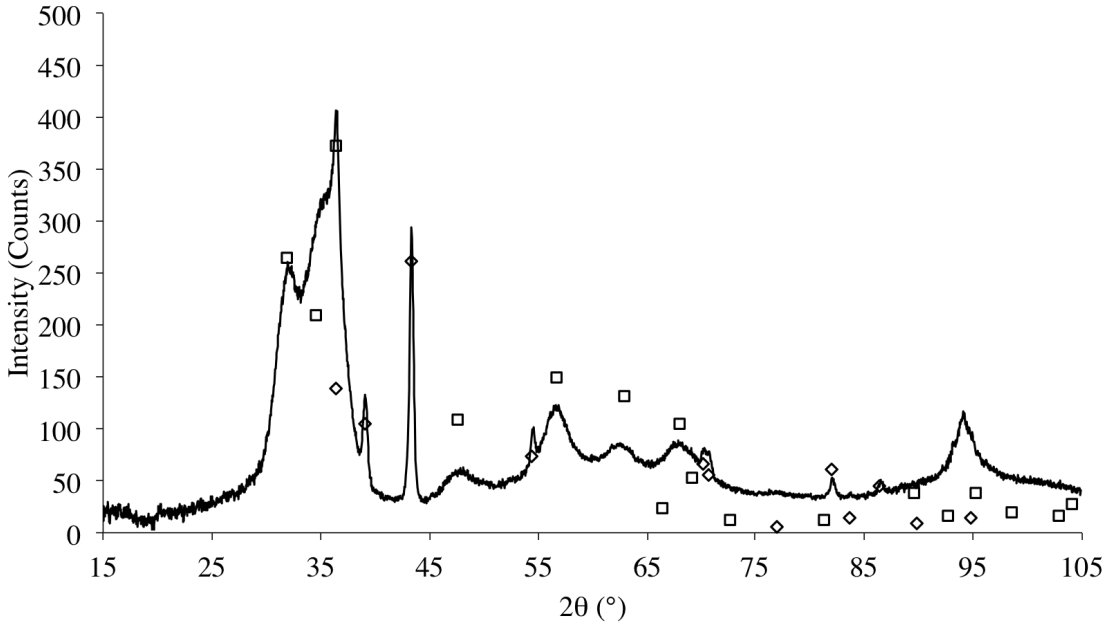


Figure 7–15: XRD spectrum of Sample 3, where 16%vol. $O_2$ was present in the RF glow discharge. The reference patterns of Zn (◇) and ZnO (□) are indicated, with each scaled by relative height. For Zn, the relative height shown is 88.93% and for ZnO, the relative height shown is 91.73%.

# CHAPTER 8
# Conclusions

The primary contribution of this PhD project is the development of a novel process which combines aerosol flow condensation for the generation of nanoparticles with a radio-frequency glow discharge plasma to facilitate their deposition by preventing their agglomeration into larger micro-particles while in-flight with the objective of synthesizing nanocomposites of nanoparticles and carbon nanotubes. Specifically, this process was used to synthesize nanocomposites of nanoparticles containing Zn and ZnO on carbon nanotubes. Neither atmospheric oxidation of the nanoparticle films, nor the presence of a 16%vol. $O_2$ RF plasma at 13.56 MHz and 20 W in the deposition apparatus were able to generate pure ZnO nanoparticles.

With regards to the synthesized nanocomposites, it initially appeared that maximum gas flow rates through the system of around 8 SLPM tended to deposit nanoparticles with a lognormal size distribution and median size of approximately 4 nm. There was some evidence that decreasing the gas flow rate through the system to around 2 SLPM tended to produce bimodally-distributed nanoparticles, with both modes having lognormal distributions and median sizes of approximately 4 to 5 nm and approximately 67 nm. Changing the composition of the RF glow discharge to include 0.5%vol. $C_2H_6$ appeared to have no effect on the size distribution, but this did seem to favour the deposition of the larger nanoparticles in clusters over the surface of the CNT.

During the course of experimentation leading to this thesis, it became apparent that the developed process exhibited large variation in the rate of nanoparticle deposition. The variation in the deposition rate of nanoparticles was quantified by measuring the thicknesses of nanoparticle layers deposited on silicon wafers by AFM. A maximum rate of deposition of the nanoparticle layer of approximately 500 nm/min was observed, however linear regressions of the measured layer thicknesses as functions of the evaporative source temperature and measured average evaporation rate resulted in 95% confidence intervals on the prediction of future layer thicknesses of approximately $\pm 225$ nm and $\pm 550$ nm, respectively, for the evaporative source temperature range of 575 to 625 °C and measured average evaporation rate range of 0.009 to 0.048 g/min. Thus, although the developed process was able to rapidly deposit nanoparticles on the substrate, the variability of the deposition rate made it effectively impossible to produce reproducible nanocomposite samples for testing as DC glow discharge cathodes.

The evaluation of the synthesized Zn/ZnO-CNT nanocomposites as cathode materials revealed no significant reduction in the sustaining voltages required to maintain a DC glow discharge in nitrogen, as compared to control samples of nanostructured CNT surfaces and untreated stainless steel. This result can be attributed to the measured variability in the designed Zn/ZnO-CNT nanocomposite synthesis process. However, this result can also be attributed to the experimental conditions under which the nanocomposites were tested. Compared to the literature values, the applied electric fields to which the nanocomposites were exposed was one to two

orders of magnitude lower than those required for field electron emission. Moreover, the previously-documented interfacial resistances between the CNTs and their SS substrates were likely responsible for the destruction of CNTs by Joule heating during DC glow discharge testing.

## 8.1 Recommendations for future work

In consideration of the conclusions of this study, particularly those resulting from the measured variability in the evaporation rate of zinc and in the deposition rate of nanoparticles, further development of the process conceived in this work is imperative if it is to be used reliably as a process for nanocomposite synthesis. Consequently, the following recommendations for future work are strongly made:

- The variability in both the average evaporation rate of zinc and the deposition rate of nanoparticles in the process must be addressed with the objective of reducing this variability such that nanocomposites with similar characteristics (e.g. nanoparticle coating thicknesses, nanoparticle size distributions, and performances as cathode materials) can be created. Toward this objective, the following suggestions are made:
  - In consideration of the likely heat transfer limitation between the filament of the evaporation source, its crucible, and the thermocouple used to regulate the setpoint temperature, this component should be replaced with a heating element whose mode of heat transfer is conductive, rather than a combination of convective and radiative heat transfer, as is the case in the current apparatus. This would result in better regulation of the evaporation source temperature, as the system pressure, gas flow rates,

and surface properties of the crucible and filament could no longer affect the heat transfer from the heating element to the evaporant. Moreover, in such a configuration, the thermocouple used to regulate the temperature of the evaporant should be in direct contact with a surface located close to the evaporant in order to obtain more precise temperature regulation. A promising candidate for a replacement heat source which meets these criteria would be a graphite heating element, since these can be manufactured in a wide range of sizes and configurations that could allow for a design which heats the crucible and thermocouple by conduction. It is further recommended that such a heating element be coated with a ceramic resistant to oxidation, such as silicon carbide. Although graphite heating elements can provide temperatures in excess of 2000 °C, they are readily oxidized at these temperatures and this results in reduced lifetimes in oxidative atmospheres.

– Since the saturation ratio is a strong function of temperature, the temperature gradient above the evaporative source should be better controlled. To this end, the use of a Knudsen cell is recommended, rather than an open crucible design. This would provide better regulation of temperature of the evaporant and its vapours. Additionally, the presence of an orifice with a surface area smaller than the available surface area of the evaporant should allow for better regulation of the rate at which vapours of the evaporant leave the evaporation source.

  - The introduction of a constrained gas flow above the orifice a Knudsen cell may be of use in providing a more uniform flow of gas, and thus help better control the condensation of nanoparticles. Such a design may be difficult to implement, as the orifice of the Knudsen cell would have to be connected to a channel perpendicular to the gas flow, and with a minimum distance between the orifice of the Knudsen cell and the gas flow in order to minimize recirculation caused by tee junctions.
  - Computational fluid dynamic simulations are recommended prior to the construction of any similar processes in order to ensure any recirculation or turbulent flows are avoided in the process. Additionally, such simulations could be used to model the nanoparticle condensation process with appropriate, additional software. Although this represents a significant amount of work, such information would be useful not only in designing effective modifications to the developed process, but would provide valuable information regarding the factors affecting nanoparticle production upon comparison with experimental data.

- The problem of CNT destruction by Joule heating in samples that have been synthesized by the CVD method used in the current work has been previously studied. Moreover, this CVD method can produce CNTs of variable quality and quantity. It would be of interest to make use of other CNT synthesis techniques which produce CNTs with fewer defects and, more importantly, less contact resistance with the substrate. The development of a project to measure and quantify the contact resistance of CNT nanostructures for electrical discharge

applications would be of long-term value, as it could form the basis for further study in modifying and evaluating the effect of plasma processing on CNT-based nano structures.

- The effectiveness of the RF glow discharge in preventing agglomeration of the produced nanoparticles remains unaddressed. A study of the nanoparticle size distributions as a function of the distance downstream of the evaporative source and comparing the effect of the presence and parameters of the RF glow discharge is recommended. However, a significant challenge to this proposed study would be the effective application of a measurement technique which could manage the sizes of the produced nanoparticles, their surface charges resulting from the RF glow discharges, and the sampling of particles under vacuum.
- Given that the RF glow discharge and plasma composition used in this project have previously been used to synthesize coated or other surface-functionalized nanoparticles, a detailed study of the RF glow discharge used in the developed process is recommended. Specifically, the ability of the discharge to functionalize the synthesized nanoparticles is of interest. However, if XPS is to be used as the primary method of investigation, an evaporant material other than zinc should be used since the binding energy shifts occurring between zinc, oxygen and carbon are relatively small and particularly difficult to de-convolute for XPS analysis. Consequently, the use of alternative evaporant materials or RF glow discharges with different atomic species for functionalization is recommended.

- Similarly, once better control of the nanoparticle synthesis and deposition is established, a review of the effects of the RF glow discharge on the morphology of the nanoparticles in the nanocomposite should be confirmed in a future work.

## REFERENCES


[1] R. Hippler, *Low Temperature Plasmas: Fundamentals, Technologies and Techniques*. Weinheim; Chichester: Wiley, 2008.

[2] A. A. Fridman and L. A. Kennedy, *Plasma Physics and Engineering*. New York: Taylor & Francis, 2004.

[3] Q. Liu, G. Ding, Z. Yang, B. Zhu, and Y. Wang, "Development of an AC plasma display panel with a low discharge voltage utilizing an electrophoretic carbon nanotube as a field emission layer," *Journal of Micromechanics and Microengineering*, vol. 22, no. 7, p. 075014, 2012.

[4] L. Qifa, W. Yan, Y. Zhuoqing, D. Haiquan, L. Chang, and D. Guifu, "Electrophoretic deposition of carbon nanotubes auxiliary layer for power saving in AC plasma display panels," *IEEE Transactions on Plasma Science*, vol. 40, no. 4, pp. 1110–1116, 2012.

[5] S.-G. Ahn, S.-H. Yoon, and Y.-S. Kim, "Secondary electron emission characteristics of MgO-ZnO alloy thin film layer for AC PDP," *Thin Solid Films*, vol. 517, no. 14, pp. 4027–4030, 2009.

[6] J. Huang, J. Wang, C. Gu, K. Yu, F. Meng, and J. Liu, "A novel highly sensitive gas ionization sensor for ammonia detection," *Sensors and Actuators A*, vol. 150, no. 2, pp. 218–223, 2009.

[7] R. B. Sadeghian and M. Kahrizi, "A novel miniature gas ionization sensor based on freestanding gold nanowires," *Sensors and Actuators A*, vol. 137, no. 2, pp. 248–255, 2007.

[8] E. Moreau, "Airflow control by non-thermal plasma actuators," *Journal of Physics D: Applied Physics*, vol. 40, no. 3, pp. 605–636, 2007.

[9] K. H. Becker, K. H. Schoenbach, and J. G. Eden, "Microplasmas and applications," *Journal of Physics D: Applied Physics*, vol. 39, no. 3, pp. R55–R70, 2006.

[10] U. N. Maiti, S. Maiti, T. P. Majumder, and K. K. Chattopadhyay, "Ultra-thin graphene edges at the nanowire tips: a cascade cold cathode with two-stage field amplification," *Nanotechnology*, vol. 22, no. 50, p. 505703, 2011.

[11] S.-H. Yoon, H. Yang, and Y.-S. Kim, "Ordered growth of ZnO nanorods for fabrication of a hybrid plasma display panel," *Nanotechnology*, vol. 18, no. 20, p. 205608, 2007.

[12] J. M. Green, L. Dong, T. Gutu, J. Jiao, J. F. Conley, and Y. Ono, "ZnO-nanoparticle-coated carbon nanotubes demonstrating enhanced electron field-emission properties," *Journal of Applied Physics*, vol. 99, no. 9, p. 094308, 2006.

[13] M. Dionne, *Optimized Carbon Nanotube Array Cathodes for Thermo-Field Emission in Plasmas: A Theoretical Model and an Experimental Verification*. PhD thesis, McGill University, 2010.

[14] M. Dionne, S. Coulombe, and J.-L. Meunier, "Low-pressure gas discharge UV source using a thermo-field emission carbon nanotube array cathode," in *Proceedings of the 12th International Symposium on the Science and Technology of Light Sources an the 3rd International Conference on White LEDs and Solid State Lighting (LS12-WLED3)*, (Eindhoven, Netherlands), July 11-16 2010.

[15] Z. Ren, Y. Lan, and Y. Wang, *Aligned Carbon Nanotubes*, ch. Properties and Applications of Aligned Carbon Nanotube Arrays, pp. 183–253. Berlin: Springer, 2013.

[16] R. Zou, J. Hu, Y. Song, N. Wang, H. Chen, H. Chen, J. Wu, Y. Sun, and Z. Chen, "Carbon nanotubes as field emitter," *Journal of Nanoscience and Nanotechnology*, vol. 10, no. 12, pp. 7876–7896, 2010.

[17] S. Zuo, X. Li, W. Liu, Y. He, Z. Xiao, and C. Zhu, "Field emission properties of the dendritic carbon nanotubes film embedded with zno quantum dots," *Journal of Nanomaterials*, vol. 2011, pp. 1–5, 2011.

[18] K. Yu, Y. S. Zhang, F. Xu, Q. Li, Z. Q. Zhu, and Q. Wan, "Significant improvement of field emission by depositing zinc oxide nanostructures on screen-printed carbon nanotube films," *Applied Physics Letters*, vol. 88, no. 15, p. 153123, 2006.

[19] C. B. Singh, S. Sarkar, V. Singh, S. K. Ram, and S. Kumar, "Ion-induced secondary electrons emission measurement from MgO films deposited on multiwalled carbon nanotubes," *Materials Letters*, vol. 76, pp. 131–134, 2012.

[20] W. Yi, S. Yu, W. Lee, I. T. Han, T. Jeong, Y. Woo, J. Lee, S. Jin, W. Choi, J. Heo, D. Jeon, and J. M. Kim, "Secondary electron emission yields from mgo

deposited on carbon nanotubes," *Journal of Applied Physics*, vol. 89, no. 7, p. 4091, 2001.

[21] G. G. Wildgoose, C. E. Banks, and R. G. Compton, "Metal nanoparticles and related materials supported on carbon nanotubes: methods and applications," *Small*, vol. 2, no. 2, pp. 182–93, 2006.

[22] Y. Liang, Y. Li, H. Wang, and H. Dai, "Strongly coupled inorganic/nanocarbon hybrid materials for advanced electrocatalysis," *J Am Chem Soc*, vol. 135, no. 6, pp. 2013–36, 2013.

[23] H. Park, J.-S. Kim, B. G. Choi, S. M. Jo, D. Y. Kim, W. H. Hong, and S.-Y. Jang, "Sonochemical hybridization of carbon nanotubes with gold nanoparticles for the production of flexible transparent conducing films," *Carbon*, vol. 48, no. 5, pp. 1325–1330, 2010.

[24] W.-C. Chang, Y.-Y. Cheng, W.-C. Yu, Y.-C. Yao, C.-H. Lee, and H.-H. Ko, "Enhancing performance of ZnO dye-sensitized solar cells by incorporation of multiwalled carbon nanotubes," *Nanoscale Research Letters*, vol. 7, no. 1, pp. 1–7, 2012.

[25] T. Y. Lee, P. S. Alegaonkar, and J.-B. Yoo, "Fabrication of dye sensitized solar cell using tio2 coated carbon nanotubes," *Thin Solid Films*, vol. 515, no. 12, pp. 5131–5135, 2007.

[26] A. Star, V. Joshi, S. Skarupo, D. Thomas, and J.-C. P. Gabriel, "Gas sensor array based on metal-decorated carbon nanotubes," *The Journal of Physical Chemistry B*, vol. 110, no. 42, pp. 21014–21020, 2006.

[27] E. J. Swanson, J. Tavares, and S. Coulombe, "Improved dual-plasma process for the synthesis of coated or functionalized metal nanoparticles," *IEEE Transactions on Plasma Science*, vol. 36, no. 4, pp. 886–887, 2008.

[28] C. Qin and S. Coulombe, "Organic layer-coated metal nanoparticles prepared by a combined arc evaporation/condensation and plasma polymerization process," *Plasma Sources Science and Technology*, vol. 16, no. 2, pp. 240–249, 2007.

[29] J. Tavares, S. Coulombe, and J. L. Meunier, "Synthesis of cubic-structured monocrystalline titanium nitride nanoparticles by means of a dual plasma process," *Journal of Physics D: Applied Physics*, vol. 42, no. 10, p. 102001, 2009.

[30] D. Nawn, D. Banerjee, and K. K. Chattopadhyay, "Zinc oxide nanostructure decorated amorphous carbon nanotubes: an improved field emitter," *Diamond and Related Materials*, vol. 34, pp. 50–59, 2013.

[31] Y.-S. Min, E. J. Bae, J. B. Park, U. J. Kim, W. Park, J. Song, C. S. Hwang, and N. Park, "ZnO nanoparticle growth on single-walled carbon nanotubes by atomic layer deposition and a consequent lifetime elongation of nanotube field emission," *Applied Physics Letters*, vol. 90, no. 26, p. 263104, 2007.

[32] L. Huang, S. P. Lau, H. Y. Yang, and S. F. Yu, "Local measurement of secondary electron emission from ZnO-coated carbon nanotubes," *Nanotechnology*, vol. 17, no. 6, pp. 1564–1567, 2006.

[33] K. Woo Hyun, K. H. Cho, C. Kyung Cheol, K. Do Youb, and O. O. Park, "Influence of gold nanoparticles on the characteristics of plasma display panels," *Electron Devices, IEEE Transactions on*, vol. 57, no. 10, pp. 2644–2650, 2010.

[34] J. G. Ok, S. H. Tawfick, K. A. Juggernauth, K. Sun, Y. Zhang, and A. J. Hart, "Electrically addressable hybrid architectures of zinc oxide nanowires grown on aligned carbon nanotubes," *Advanced Functional Materials*, vol. 20, no. 15, pp. 2470–2480, 2010.

[35] X. L. Li, C. Li, Y. Zhang, D. P. Chu, W. I. Milne, and H. J. Fan, "Atomic layer deposition of ZnO on multi-walled carbon nanotubes and its use for synthesis of CNT-ZnO heterostructures," *Nanoscale Research Letters*, vol. 5, no. 11, pp. 1836–1840, 2010.

[36] B. Aïssa, C. Fauteux, M. A. El Khakani, and D. Therriault, "Structural and photoluminescence properties of laser processed ZnO/carbon nanotube nanohybrids," *Journal of Materials Research*, vol. 24, no. 11, pp. 3313–3320, 2009.

[37] P. M. Parker, "World outlook report 2006-2011: compact fluorescent light bulbs," 2005.

[38] M. Born and T. Markus, *Research on Modern Gas Discharge Light Sources*, ch. 15, pp. 399–423. Berlin: Springer-Verlag, 2005.

[39] S. Coulombe and J.-L. Meunier, "Thermo-field emission: a comparative study," *Journal of Physics D: Applied Physics*, vol. 30, no. 5, p. 776, 1997.

[40] L. Rao, R. J. Munz, and J.-L. Meunier, "Vacuum arc velocity and erosion rate measurements on nanostructured plasma and HVOF spray coatings," *Journal of Physics D: Applied Physics*, vol. 40, no. 14, pp. 4192–4201, 2007.

[41] G. Herrmann and P. S. Wagener, *The Oxide-Coated Cathode*, vol. 1. London: Chapman & Hall, 1951.

[42] T. Okada and T. Yoshioka, "Application of carbon nanotubes as a source of priming electrons in AC plasma display panels," *Applied Physics Letters*, vol. 93, no. 17, p. 171501, 2008.

[43] G. S. Bocharov and A. V. Eletskii, "Degradation of a carbon nanotube-based field-emission cathode during ion sputtering," *Technical Physics*, vol. 57, no. 7, pp. 1008–1012, 2012.

[44] L. Vandsburger, S. Coulombe, and J. L. Meunier, "Degradation of carbon nanotubes in oxygen glow discharges," *Carbon*, vol. 57, pp. 248–258, 2013.

[45] S. Berhanu, O. Grning, Z. Chen, J. Merikhi, M. Kaiser, N. L. Rupesinghe, and P. K. Bachmann, "Microscopic analysis of performance variations in carbon nanotube field emission cathodes: implications for device optimization," *Physica Status Solidi A*, vol. 209, no. 11, pp. 2114–2125, 2012.

[46] W. T. Lee, S. J. Im, J. Geon Han, S. Yu, H. Y. Kim, I. T. Han, J. B. Yoo, K. Y. Kim, J. W. Lee, J. M. Kim, and E. H. Choi, "MgO/carbon nanotubes protective layer in AC-plasma display panels," *Japanese Journal of Applied Physics*, vol. 41, no. 11A, Part 1, pp. 6550–6552, 2002.

[47] P. Rumbach and D. B. Go, "Fundamental properties of field emission-driven direct current microdischarges," *Journal of Applied Physics*, vol. 112, no. 10, p. 103302, 2012.

[48] A. Von Engel, *Ionized gases*. Oxford: Clarendon Press, 1965.

[49] S. Iijima, "Helical microtubules of graphitic carbon," *Nature*, vol. 354, no. 6348, pp. 56–58, 1991.

[50] W. I. Milne, K. B. K. Teo, G. A. J. Amaratunga, P. Legagneux, L. Gangloff, J. P. Schnell, V. Semet, V. Thien Binh, and O. Groening, "Carbon nanotubes as field emission sources," *Journal of Materials Chemistry*, vol. 14, no. 6, pp. 933–943, 2004.

[51] J.-M. Bonard, H. Kind, T. Stckli, and L.-O. Nilsson, "Field emission from carbon nanotubes: the first five years," *Solid-State Electronics*, vol. 45, no. 6, pp. 893–914, 2001.

[52] D. N. Futaba, H. Kimura, B. Zhao, T. Yamada, H. Kurachi, S. Uemura, and K. Hata, "Carbon nanotube loop arrays for low-operational power, high uniformity field emission with long-term stability," *Carbon*, vol. 50, no. 8, pp. 2796–2803, 2012.

[53] S. Neupane, M. Lastres, M. Chiarella, W. Li, Q. Su, and G. Du, "Synthesis and field emission properties of vertically aligned carbon nanotube arrays on copper," *Carbon*, vol. 50, no. 7, pp. 2641–2650, 2012.

[54] B.-R. Huang, T.-C. Lin, J. P. Chu, and Y.-C. Chen, "Long-term stability of a horizontally-aligned carbon nanotube field emission cathode coated with a metallic glass thin film," *Carbon*, vol. 50, no. 4, pp. 1619–1624, 2012.

[55] J. W. Jeong, J. W. Kim, J. T. Kang, S. Choi, S. Ahn, and Y. H. Song, "A vacuum-sealed compact X-ray tube based on focused carbon nanotube field-emission electrons," *Nanotechnology*, vol. 24, no. 8, p. 085201, 2013.

[56] G. Z. Yue, Q. Qiu, B. Gao, Y. Cheng, J. Zhang, H. Shimoda, S. Chang, J. P. Lu, and O. Zhou, "Generation of continuous and pulsed diagnostic imaging X-ray radiation using a carbon-nanotube-based field-emission cathode," *Applied*

*Physics Letters*, vol. 81, no. 2, pp. 355–357, 2002.

[57] S. Agarwal, B. Yamini Sarada, and K. K. Kar, "The fabrication of carbon-nanotube-coated electrodes and a field-emission-based luminescent device," *Nanotechnology*, vol. 21, no. 6, p. 065601, 2010.

[58] Y. Zhang, S. Z. Deng, N. S. Xu, and J. Chen, "Fully sealed carbon nanotube flat-panel light source and its application as thin film transistor-liquid-crystal display backlight," *Journal of Vacuum Science & Technology B: Microelectronics and Nanometer Structures*, vol. 26, no. 3, p. 1033, 2008.

[59] Y. Wei, L. Xiao, F. Zhu, L. Liu, J. Tang, P. Liu, and S. Fan, "Cold linear cathodes with carbon nanotube emitters and their application in luminescent tubes," *Nanotechnology*, vol. 18, no. 32, p. 325702, 2007.

[60] A. A. Kuznetzov, S. B. Lee, M. Zhang, R. H. Baughman, and A. A. Zakhidov, "Electron field emission from transparent multiwalled carbon nanotube sheets for inverted field emission displays," *Carbon*, vol. 48, no. 1, pp. 41–46, 2010.

[61] W. B. Choi, D. S. Chung, J. H. Kang, H. Y. Kim, Y. W. Jin, I. T. Han, Y. H. Lee, J. E. Jung, N. S. Lee, G. S. Park, and J. M. Kim, "Fully sealed, high-brightness carbon-nanotube field-emission display," *Applied Physics Letters*, vol. 75, no. 20, pp. 3129–3131, 1999.

[62] J. G. Eden, S. J. Park, N. P. Ostrom, and K. F. Chen, "Recent advances in microcavity plasma devices and arrays: a versatile photonic platform," *Journal of Physics D: Applied Physics*, vol. 38, no. 11, pp. 1644–1648, 2005.

[63] Q. Zou, Y. G. Li, M. Z. Wang, Y. C. Zhao, and L. H. Zou, "Generation of microplasma using multiwall carbon nanotubes cathode," *Plasma Devices and*

*Operations*, vol. 17, no. 3, pp. 181–190, 2009.

[64] S. J. Park, J. G. Eden, and K. H. Park, "Carbon nanotube-enhanced performance of microplasma devices," *Applied Physics Letters*, vol. 84, no. 22, pp. 4481–4483, 2004.

[65] Y. K. Yap, J. Menda, L. K. Vanga, V. Kayastha, J. Wang, L. B. King, S. Dimovski, and Y. Gogotsi, "Testing multiwall carbon nanotubes on ion erosion for advanced space propulsion," *MRS Proceedings*, vol. 821, p. 3.7, 2004.

[66] R. Rosen, W. Simendinger, C. Debbault, H. Shimoda, L. Fleming, B. Stoner, and O. Zhou, "Application of carbon nanotubes as electrodes in gas discharge tubes," *Applied Physics Letters*, vol. 76, no. 13, pp. 1668–1670, 2000.

[67] B.-J. Lee, E.-C. Shin, and G.-H. Jeong, "Structure modifications of vertically grown carbon nanotubes by plasma ion bombardment," *Vacuum*, vol. 84, no. 12, pp. 1398–1401, 2010.

[68] S. Lee and J.-W. Peng, "Effect of plasma treatment on electrical conductivity and raman spectra of carbon nanotubes," *Journal of Physics and Chemistry of Solids*, vol. 72, no. 9, pp. 1101–1103, 2011.

[69] J. B. Liu, J. Chen, N. S. Xu, S. Z. Deng, and J. C. She, "Achieving uniform field emission from carbon nanotube composite cold cathode with different carbon nanotube contents: effects of conductance and plasma treatment," *Ultramicroscopy*, vol. 109, no. 5, pp. 390–394, 2009.

[70] G. Chen, S. Neupane, W. Li, L. Chen, and J. Zhang, "An increase in the field emission from vertically aligned multiwalled carbon nanotubes caused by $NH_3$ plasma treatment," *Carbon*, vol. 52, pp. 468–475, 2013.

[71] Z. Hou, B. Cai, H. Liu, and D. Xu, "Ar, $O_2$, $CHF_3$, and $SF_6$ plasma treatments of screen-printed carbon nanotube films for electrode applications," *Carbon*, vol. 46, no. 3, pp. 405–413, 2008.

[72] K. S. Hazra, N. A. Koratkar, and D. S. Misra, "Improved field emission from multiwall carbon nanotubes with nano-size defects produced by ultra-low energy ion bombardment," *Carbon*, vol. 49, no. 14, pp. 4760–4766, 2011.

[73] S. Lee, Y.-C. Liu, and C.-H. Chen, "Raman study of the temperature-dependence of plasma-induced defect formation rates in carbon nanotubes," *Carbon*, vol. 50, no. 14, pp. 5210–5216, 2012.

[74] D. Eder, "Carbon nanotube?inorganic hybrids," *Chemical Reviews*, vol. 110, no. 3, pp. 1348–1385, 2010.

[75] S. Zuo, X. Li, W. Liu, Y. He, Z. Xiao, and C. Zhu, "Field emission properties of the dendritic carbon nanotubes film embedded with ZnO quantum dots," *Journal of Nanomaterials*, vol. 2011, pp. 1–5, 2011.

[76] C.-S. Huang, C.-Y. Yeh, Y.-H. Chang, Y.-M. Hsieh, C.-Y. Ku, and Q.-T. Lai, "Field emission properties of CNT-ZnO composite materials," *Diamond and Related Materials*, vol. 18, no. 2-3, pp. 452–456, 2009.

[77] A. Wisitsoraat, A. Tuantranont, V. Patthanasettakul, and S. Mongpraneet, "Electron field emission from $ZnO_x$ nanoparticles decorated on vertically aligned carbon nanotubes prepared by vapor-phase transport," *Journal of Vacuum Science & Technology B: Microelectronics and Nanometer Structures*, vol. 26, no. 5, pp. 1757–1760, 2008.

[78] D. Hasselkamp, *Particle Induced Electron Emission II.* Berlin; New York: Springer-Verlag, 1992.

[79] J. Z. Sun, A. Qin, and B. Z. Tang, "Functional polyacetylenes: hybrids with carbon nanotubes," *Polymer Chemistry*, vol. 4, no. 2, pp. 211–223, 2013.

[80] C. S. Chen, X. H. Chen, B. Yi, T. G. Liu, W. H. Li, L. S. Xu, Z. Yang, H. Zhang, and Y. G. Wang, "Zinc oxide nanoparticle decorated multi-walled carbon nanotubes and their optical properties," *Acta Materialia*, vol. 54, no. 20, pp. 5401–5407, 2006.

[81] F. Vietmeyer, B. Seger, and P. V. Kamat, "Anchoring ZnO particles on functionalized single wall carbon nanotubes: excited state interactions and charge collection," *Advanced Materials*, vol. 19, no. 19, pp. 2935–2940, 2007.

[82] Y. Wang, J. Wu, and F. Wei, "A treatment method to give separated multi-walled carbon nanotubes with high purity, high crystallization and a large aspect ratio," *Carbon*, vol. 41, no. 15, pp. 2939–2948, 2003.

[83] W. S. Kim, H. Oki, A. Kinoshita, K. Murakami, S. Abo, F. Wakaya, and M. Takai, "Relationship between field-emission characteristics and defects measured by raman scattering in carbon-nanotube cathodes treated by plasma and laser," *Journal of Vacuum Science & Technology B: Microelectronics and Nanometer Structures*, vol. 26, no. 2, pp. 760–763, 2008.

[84] N. Kondo, T. Yamamoto, and K. Watanabe, "Molecular dynamics simulations of thermal transport in carbon nanotubes with structural defects," *e-Journal of Surface Science and Nanotechnology*, vol. 4, pp. 239–243, 2006.

[85] A. Stetter, J. Vancea, and C. H. Back, "Conductivity of multiwall carbon nanotubes: role of multiple shells and defects," *Physical Review B*, vol. 82, no. 11, p. 115451, 2010.

[86] H. Chu, L. Wei, R. Cui, J. Wang, and Y. Li, "Carbon nanotubes combined with inorganic nanomaterials: preparations and applications," *Coordination Chemistry Reviews*, vol. 254, no. 9-10, pp. 1117–1134, 2010.

[87] J. H. Seinfeld and S. N. Pandis, *Atmospheric Chemistry and Physics: From Air Pollution to Climate Change*. New York: Wiley, 1998.

[88] S. K. Friedlander, "The behavior of constant rate aerosol reactors," *Aerosol Science and Technology*, vol. 1, no. 1, pp. 3–13, 1981.

[89] D. M. Mattox, *Handbook of Physical Vapor Deposition (PVD) Processing*. Amsterdam: William Andrew Publishing, 2nd ed., 2010.

[90] V. K. Badam, V. Kumar, F. Durst, and K. Danov, "Experimental and theoretical investigations on interfacial temperature jumps during evaporation," *Experimental Thermal and Fluid Science*, vol. 32, no. 1, pp. 276–292, 2007.

[91] T. F. Kuech and K. F. Jensen, *Thin Film Processes II*, ch. OMPVE of Compound Semiconductors, pp. 370–398. Elsevier, 1991.

[92] S. E. Pratsinis, T. T. Kodas, M. P. Dudukovic, and S. K. Friedlander, "Aerosol reactor design: effect of reactor geometry on powder production and vapor deposition," *Powder Technology*, vol. 47, no. 1, pp. 17–23, 1986.

[93] S. E. Pratsinis, "Simultaneous nucleation, condensation, and coagulation in aerosol reactors," *Journal of Colloid and Interface Science*, vol. 124, no. 2, pp. 416–427, 1988.

[94] I. Agranovski, *Aerosols: Science and Technology*. Wiley, 2010.

[95] S. K. Friedlander, *Smoke, Dust, and Haze: Fundamentals of Aerosol Dynamics*. New York: Oxford University Press, 2000.

[96] J. H. Seinfeld, *Atmospheric Chemistry and Physics of Air Pollution*. New York: Wiley, 1986.

[97] C. G. Granqvist and R. A. Buhrman, "Ultrafine metal particles," *Journal of Applied Physics*, vol. 47, no. 5, pp. 2200–2219, 1976.

[98] R. Birringer, H. Gleiter, H. P. Klein, and P. Marquardt, "Nanocrystalline materials: an approach to a novel solid structure with gas-like disorder?," *Physics Letters A*, vol. 102, no. 8, pp. 365–369, 1984.

[99] L. Pasquini, E. Callini, M. Brighi, F. Boscherini, A. Montone, T. R. Jensen, C. Maurizio, M. Vittori Antisari, and E. Bonetti, "Magnesium nanoparticles with transition metal decoration for hydrogen storage," *Journal of Nanoparticle Research*, vol. 13, no. 11, pp. 5727–5737, 2011.

[100] R. W. Siegel, "Cluster-assembled nanophase materials," *Annual Review of Materials Science*, vol. 21, no. 1, pp. 559–578, 1991.

[101] R. S. Averback, "Sintering and deformation of nano-grained materials," *Zeitschrift für Physik D: Atoms, Molecules and Clusters*, vol. 26, no. 1, pp. 84–88, 1993.

[102] A. Ceylan, K. Jastrzembski, and S. I. Shah, "Enhanced solubility Ag-Cu nanoparticles and their thermal transport properties," *Metallurgical and Materials Transactions A: Physical Metallurgy and Materials Science*, vol. 37, no. 7, pp. 2033–2038, 2006.

[103] M. Raffi, A. K. Rumaiz, M. M. Hasan, and S. I. Shah, "Studies of the growth parameters for silver nanoparticle synthesis by inert gas condensation," *Journal of Materials Research*, vol. 22, no. 12, pp. 3378–3384, 2011.

[104] C. Suryanarayana and B. Prabhu, *Nanostructured Materials: Processing, Properties, and Applications*, ch. Synthesis of Nanostructured Materials by Inert-Gas Condensation Methods, pp. 47–90. New York: Noyes Publications, 2nd ed., 2007.

[105] C. Suryanarayana and C. C. Koch, "Nanocrystalline materials–current research and future directions," *Hyperfine Interactions*, vol. 130, no. 1-4, pp. 5–44, 2000.

[106] A. H. Pfund, "The optical properties of metallic and crystalline powders," *Journal of the Optical Society of America*, vol. 23, no. 10, pp. 375–377, 1933.

[107] L. Harris, R. T. McGinnies, and B. M. Siegel, "The preparation and optical properties of gold blacks," *Journal of the Optical Society of America*, vol. 38, no. 7, pp. 582–588, 1948.

[108] L. Harris, D. Jeffries, and B. M. Siegel, "An electron microscope study of gold smoke deposits," *Journal of Applied Physics*, vol. 19, no. 8, pp. 791–794, 1948.

[109] M. Scarselli, L. Camilli, P. Castrucci, F. Nanni, S. Del Gobbo, E. Gautron, S. Lefrant, and M. De Crescenzi, "In situ formation of noble metal nanoparticles on multiwalled carbon nanotubes and its implication in metalnanotube interactions," *Carbon*, vol. 50, no. 3, pp. 875–884, 2012.

[110] C. Bittencourt, A. Felten, B. Douhard, J. F. Colomer, G. Van Tendeloo, W. Drube, J. Ghijsen, and J. J. Pireaux, "Metallic nanoparticles on plasma treated carbon nanotubes: Nano$^2$hybrids," *Surface Science*, vol. 601, no. 13,

pp. 2800–2804, 2007.

[111] S. E. Pratsinis, "Aerosol-based technologies in nanoscale manufacturing: from functional materials to devices through core chemical engineering," *AIChE Journal*, vol. 56, no. 12, pp. 3028–3035, 2010.

[112] K. Wegner, B. Walker, S. Tsantilis, and S. E. Pratsinis, "Design of metal nanoparticle synthesis by vapor flow condensation," *Chemical Engineering Science*, vol. 57, no. 10, pp. 1753–1762, 2002.

[113] V. Haas, R. Birringer, H. Gleiter, and S. E. Pratsinis, "Synthesis of nanostructured powders in an aerosol flow condenser," *Journal of Aerosol Science*, vol. 28, no. 8, pp. 1443–1453, 1997.

[114] Y. M. Ho, G. M. Yang, W. T. Zheng, X. Wang, H. W. Tian, Q. Xu, H. B. Li, J. W. Liu, J. L. Qi, and Q. Jiang, "Synthesis and field electron emission properties of hybrid carbon nanotubes and nanoparticles," *Nanotechnology*, vol. 19, no. 6, p. 065710, 2008.

[115] I. S. Hwang, J. C. Kim, S. D. Seo, S. Lee, J. H. Lee, and D. W. Kim, "A binder-free Ge-nanoparticle anode assembled on multiwalled carbon nanotube networks for Li-ion batteries," *Chemical Communications*, vol. 48, no. 56, pp. 7061–7063, 2012.

[116] Y. Zhang, Q. Zhang, Y. Li, N. Wang, and J. Zhu, "Coating of carbon nanotubes with tungsten by physical vapor deposition," *Solid State Communications*, vol. 115, no. 1, pp. 51–55, 2000.

[117] M. T. Swihart, "Vapor-phase synthesis of nanoparticles," *Current Opinion in Colloid & Interface Science*, vol. 8, no. 1, pp. 127–133, 2003.

[118] W. Chang, G. Skandan, H. Hahn, S. C. Danforth, and B. H. Kear, "Chemical vapor condensation of nanostructured ceramic powders," *Nanostructured Materials*, vol. 4, no. 3, pp. 345–351, 1994.

[119] E. S. Vasilyeva, O. V. Tolochko, B. K. Kim, D. W. Lee, and D. S. Kim, "Synthesis of tungsten disulphide nanoparticles by the chemical vapor condensation method," *Microelectronics Journal*, vol. 40, no. 4-5, pp. 687–691, 2009.

[120] G. Kim, J. Bang, Y. Kim, S. Rout, and S. Woo, "Structural, electrical and optical properties of boron doped ZnO thin films using lsmcd method at room temperature," *Applied Physics A: Materials Science & Processing*, vol. 97, no. 4, pp. 821–828, 2009.

[121] M. Ehbrecht, H. Ferkel, V. V. Smirnov, O. M. Stelmakh, W. Zhang, and F. Huisken, "Laser-driven flow reactor as a cluster beam source," *Review of Scientific Instruments*, vol. 66, no. 7, pp. 3833–3837, 1995.

[122] E. Borsella, S. Botti, M. C. Cesile, S. Martelli, A. Nesterenko, and P. G. Zappelli, "$MoS_2$ nanoparticles produced by laser induced synthesis from gaseous precursors," *Journal of Materials Science Letters*, vol. 20, no. 2, pp. 187–191, 2001.

[123] M. Ali, N. Friedenberger, M. Spasova, and M. Winterer, "A novel approach for chemical vapor synthesis of ZnO nanocrystals: optimization of yield, crystallinity," *Chemical Vapor Deposition*, vol. 15, no. 7-9, pp. 192–198, 2009.

[124] J. Suffner, P. Ágoston, J. Kling, and H. Hahn, "Chemical vapor synthesis of fluorine-doped $SnO_2$ (FTO) nanoparticles," *Journal of Nanoparticle Research*, vol. 12, no. 7, pp. 2579–2588, 2009.

[125] J. C. Kim and B. K. Kim, "Synthesis of nanosized tungsten carbide powder by the chemical vapor condensation process," *Scripta Materialia*, vol. 50, no. 7, pp. 969–972, 2004.

[126] D. Li, C. J. Choi, B. K. Kim, and Z. D. Zhang, "Characterization of FeN nanoparticles synthesized by the chemical vapor condensation process," *Journal of Magnetism and Magnetic Materials*, vol. 277, no. 1-2, pp. 64–70, 2004.

[127] C. J. Choi, X. L. Dong, and B. K. Kim, "Characterization of Fe and Co nanoparticles synthesized by chemical vapor condensation," *Scripta Materialia*, vol. 44, no. 8-9, pp. 2225–2229, 2001.

[128] R. Dharmadasa, A. A. Tahir, and K. G. U. Wijayantha, "Single step growth and characterization of zinc oxide, tin oxide, and composite ($Zn_xSn_{1-x}O_y$) nanoplate and nanocolumn electrodes," *Journal of the American Ceramic Society*, vol. 94, no. 10, pp. 3540–3546, 2011.

[129] L. Sun, H. He, C. Liu, Y. Lu, and Z. Ye, "Controllable growth and optical properties of ZnO nanostructures on Si nanowire arrays," *CrystEngComm*, vol. 13, no. 7, pp. 2439–2444, 2011.

[130] O. Yilmazoglu, R. Joshi, A. Popp, D. Pavlidis, and J. J. Schneider, "Pronounced field emission from vertically aligned carbon nanotube blocks and bundles," *Journal of Vacuum Science & Technology B: Microelectronics and Nanometer Structures*, vol. 29, no. 2, pp. 02B106–1–02B106–5, 2011.

[131] N. G. Semaltianos, "Nanoparticles by laser ablation," *Critical Reviews in Solid State and Materials Sciences*, vol. 35, no. 2, pp. 105–124, 2010.

[132] E. Fazio, S. Patan, S. Scibilia, A. M. Mezzasalma, G. Mondio, F. Neri, and S. Trusso, "Structural and optical properties of pulsed laser deposited ZnO thin films," *Current Applied Physics*, vol. 13, no. 4, pp. 710–716, 2013.

[133] A. Koshio, M. Shiraishi, Y. Kobayashi, M. Ishihara, Y. Koga, S. Bandow, S. Iijima, and F. Kokai, "Modification of carbon nanotubes by laser ablation of copper," *Chemical Physics Letters*, vol. 396, no. 4-6, pp. 410–414, 2004.

[134] A. Anders, "Approaches to rid cathodic arc plasmas of macro- and nanoparticles: a review," *Surface and Coatings Technology*, vol. 120-121, pp. 319–330, 1999.

[135] D. M. Sanders, R. L. Boxman, and P. J. Martin, *Handbook of Vacuum Arc Science and Technology: Fundamentals and Applications*. New Jersey: Noyes Publications, 1995.

[136] L. Rao, N. K. Reddy, S. Coulombe, J.-L. Meunier, and R. J. Munz, "Carbon nanotubes as nanoparticles collector," *Journal of Nanoparticle Research*, vol. 9, no. 4, pp. 689–695, 2006.

[137] W. Han, P. Redlich, F. Ernst, and M. Rühle, "Synthesis of GaN-carbon composite nanotubes and GaN nanorods by arc discharge in nitrogen atmosphere," *Applied Physics Letters*, vol. 76, no. 5, p. 652, 2000.

[138] K. Suenaga, C. Colliex, N. Demoncy, A. Loiseau, H. Pascard, and F. Willaime, "Synthesis of nanoparticles and nanotubes with well-separated layers of boron nitride and carbon," *Science*, vol. 278, no. 5338, pp. 653–655, 1997.

[139] T. Charinpanitkul, A. Soottitantawat, N. Tonanon, and W. Tanthapanichakoon, "Single-step synthesis of nanocomposite of copper and carbon

nanoparticles using arc discharge in liquid nitrogen," *Materials Chemistry and Physics*, vol. 116, no. 1, pp. 125–128, 2009.

[140] D. Bera, S. C. Kuiry, M. McCutchen, S. Seal, H. Heinrich, and G. C. Slane, "In situ synthesis of carbon nanotubes decorated with palladium nanoparticles using arc-discharge in solution method," *Journal of Applied Physics*, vol. 96, no. 9, pp. 5152–5157, 2004.

[141] C. E. Baddour, *Direct Growth of Carbon Nanotubes on Metal Surfaces Without an External Catalyst and Nanocomposite Production*. PhD thesis, McGill University, 2010.

[142] C. E. Baddour, F. Fadlallah, D. Nasuhoglu, R. Mitra, L. Vandsburger, and J.-L. Meunier, "A simple thermal CVD method for carbon nanotube synthesis on stainless steel 304 without the addition of an external catalyst," *Carbon*, vol. 47, no. 1, pp. 313–318, 2008.

[143] L. Vandsburger, "Synthesis and covalent surface modification of carbon nanotubes for preparation of stabilized nanofluid suspensions," Master's thesis, McGill University, 2009.

[144] N. Hordy, "Direct growth of carbon nanotubes from stainless steel grids and plasma functionalization for poly(vinyl alcohol) composite production," Master's thesis, McGill University, 2011.

[145] K. T. A. L. Burm, "Calculation of the townsend discharge coefficients and the paschen curve coefficients," *Contributions to Plasma Physics*, vol. 47, no. 3, pp. 177–182, 2007.

[146] S. C. Brown, *Basic Data of Plasma Physics*. Cambridge: Technology Press of the Massachusetts Institute of Technology, 1959.

[147] K. Kubo, T. Hirakawa, H. Uchiike, and S. Goto, "Ion-induced secondary electron emission characteristics of new protecting materials for AC PDPs," in *SID Conference Record of the International Display Research Conference*, pp. 957–960, 2001.

[148] M. K. Sharma, B. K. Saikia, A. Phukan, and B. Ganguli, "Plasma nitriding of austenitic stainless steel in $N_2$ and $N_2 - H_2$ DC pulsed discharge," *Surface and Coatings Technology*, vol. 201, no. 6, pp. 2407–2413, 2006.

[149] J. J. Camacho, L. Daz, M. Santos, D. Reyman, and J. M. L. Poyato, "Optical emission spectroscopic study of plasma plumes generated by IR $CO_2$ pulsed laser on carbon targets," *Journal of Physics D: Applied Physics*, vol. 41, no. 10, p. 105201, 2008.

[150] S. Sato and K. Koyama, "Relationship between electrode surface roughness and impulse breakdown voltage in vacuum gap of Cu and Cu-Cr electrodes," *Dielectrics and Electrical Insulation, IEEE Transactions on*, vol. 10, no. 4, pp. 576–582, 2003.

[151] J. Tavares, E. J. Swanson, and S. Coulombe, "Plasma synthesis of coated metal nanoparticles with surface properties tailored for dispersion," *Plasma Processes and Polymers*, vol. 5, no. 8, pp. 759–769, 2008.

[152] J. Tavares and S. Coulombe, "Dual plasma synthesis and characterization of a stable copper-ethylene glycol nanofluid," *Powder Technology*, vol. 210, no. 2, pp. 132–142, 2011.

[153] J. Tavares, *Dual plasma synthesis of functionalized metal nanoparticles: from enhanced surface properties to stable nanofluids*. PhD thesis, McGill University, 2010.

[154] C. Perkins, P. Lichty, and A. W. Weimer, "Determination of aerosol kinetics of thermal ZnO dissociation by thermogravimetry," *Chemical Engineering Science*, vol. 62, no. 21, pp. 5952–5962, 2007.

[155] A. Weidenkaff, A. Steinfeld, A. Wokaun, P. O. Auer, B. Eichler, and A. Reller, "Direct solar thermal dissociation of zinc oxide: condensation and crystallisation of zinc in the presence of oxygen," *Solar Energy*, vol. 65, no. 1, pp. 59–69, 1999.

[156] H. Sun and X. Pan, "Microstructure of ZnO shell on Zn nanoparticles," *Journal of Materials Research*, vol. 19, no. 10, pp. 3062–3067, 2011.

[157] Y. M. Ho, J. W. Liu, J. L. Qi, and W. T. Zheng, "Spectroscopic investigation on carbon nanotubes coated with ZnO nanoparticles," *Journal of Physics D: Applied Physics*, vol. 41, no. 6, p. 065308, 2008.

[158] O. J. Yoon, S. M. Kang, S. M. Moon, J. K. Jung, I. S. Choi, and K. R. Yoon, "Deposition of iron nanoparticles onto multiwalled carbon nanotubes by helicon plasma-enhanced, chemical vapor deposition," *Journal of Non-Crystalline Solids*, vol. 353, no. 11-12, pp. 1208–1211, 2007.

[159] M. Abramoff, P. Magalhaes, and S. J. Ram, "Image processing with ImageJ," *Biophotonics International*, vol. 11, no. 7, pp. 36–42, 2004.

[160] M. Shiratani, H. Kawasaki, T. Fukuzawa, T. Yoshioka, Y. Ueda, S. Singh, and Y. Watanabe, "Simultaneous in situ measurements of properties of particulates in RF silane plasmas using a polarization-sensitive laser-light-scattering method," *Journal of Applied Physics*, vol. 79, no. 1, pp. 104–109, 1996.

[161] Y. Watanabe, M. Shiratani, H. Kawasaki, S. Singh, T. Fukuzawa, Y. Ueda, and H. Ohkura, "Growth processes of particles in high frequency silane plasmas," *Journal of Vacuum Science and Technology A*, vol. 14, no. 2, pp. 540–545, 1996.

[162] L. Ravi and S. Girshick, "Coagulation of nanoparticles in a plasma," *Physical Review E*, vol. 79, no. 2, p. 026408, 2009.

[163] J. B. Baxter and C. A. Schmuttenmaer, "Conductivity of ZnO nanowires, nanoparticles, and thin films using time-resolved terahertz spectroscopy," *The Journal of Physical Chemistry B*, vol. 110, no. 50, pp. 25229–25239, 2006.

[164] A. J. Morfa, G. Beane, B. Mashford, B. Singh, E. D. Gaspera, A. Martucci, and P. Mulvaney, "Fabrication of ZnO thin films from nanocrystal inks," *The Journal of Physical Chemistry C*, vol. 114, no. 46, pp. 19815–19821, 2010.

[165] D. C. Montgomery and G. C. Runger, *Applied Statistics and Probability for Engineers*. New York: Wiley, 2nd ed., 2003.

[166] E. Lassner and W.-D. Schubert, *Tungsten: Properties, Chemistry, Technology of the Elements, Alloys, and Chemical Compounds*. New York: Plenum Press, 1999.

[167] H. Yasuda, *Plasma polymerization*. Orlando: Academic Press, 1985.

[168] R. T. Downs and M. Hall-Wallace, "The american mineralogist crystal structure database," *American Mineralogist*, vol. 88, pp. 247–250, 2003.